Neuron

Article

# EndophilinA-dependent coupling between activity-induced calcium influx and synaptic autophagy is disrupted by a Parkinson-risk mutation

## Highlights

- Pre-synaptic $Ca^{2+}$ influx induces autophagy at *Drosophila* synapses
- $Ca^{2+}$ influx drives changes in EndoA rigidity, localization, and synaptic autophagy
- Starvation and $Ca^{2+}$ influx independently trigger autophagosome formation
- A Parkinson disease-linked mutation in EndoA1 blocks synaptic autophagy


## Authors

Adekunle T. Bademosi, Marianna Decet, Sabine Kuenen, ..., Joost Schymkowitz, Sandra-F. Soukup, Patrik Verstreken

## Correspondence

soukuplab@gmail.com (S.-F.S.), patrik.verstreken@kuleuven.be (P.V.)



## In brief

Bademosi, Decet, and Kuenen et al. show that synaptic autophagy is triggered by calcium influx during neuronal activity. This is mediated by rigidity changes in EndoA structure driving protein mobility and protein re-localization. A Parkinson disease-linked variant in EndoA1 impinges on this process and blocks autophagy in flies and human neurons.


Bademosi et al., 2023, Neuron *111*, 1–21
May 3, 2023 © 2023 The Authors. Published by Elsevier Inc.
https://doi.org/10.1016/j.neuron.2023.02.001

CellPress

Please cite this article in press as: Bademosi et al., EndophilinA-dependent coupling between activity-induced calcium influx and synaptic autophagy is disrupted by a Parkinson-risk mutation, Neuron (2023), https://doi.org/10.1016/j.neuron.2023.02.001

Neuron

CellPress
OPEN ACCESS

Article

# EndophilinA-dependent coupling between activity-induced calcium influx and synaptic autophagy is disrupted by a Parkinson-risk mutation

Adekunle T. Bademosi,[1,2,3,12] Marianna Decet,[1,2,12] Sabine Kuenen,[1,2,12] Carles Calatayud,[1,2] Jef Swerts,[1,2] Sandra F. Gallego,[1,2] Nils Schoovaerts,[1,2] Spyridoula Karamanou,[7] Nikolaos Louros,[1,4] Ella Martin,[5,6] Jean-Baptiste Sibarita,[8] Katlijn Vints,[1,2,9] Natalia V. Gounko,[1,2,9] Frédéric A. Meunier,[3,10] Anastassios Economou,[7] Wim Versées,[5,6] Frederic Rousseau,[1,4] Joost Schymkowitz,[1,4] Sandra-F. Soukup,[11,*] and Patrik Verstreken[1,2,13,*]

[1]VIB-KU Leuven Center for Brain & Disease Research, Leuven 3000, Belgium
[2]KU Leuven, Department of Neurosciences, Leuven Brain Institute, Mission Lucidity, Leuven 3000, Belgium
[3]Clem Jones Centre for Ageing Dementia Research, Queensland Brain Institute, The University of Queensland, St Lucia Campus, Brisbane, QLD 4072, Australia
[4]Switch Laboratory, Department of Cellular and Molecular Medicine, KU Leuven, Leuven 3000, Belgium
[5]VIB-VUB Center for Structural Biology, Brussels 1050, Belgium
[6]Department of Structural Biology Brussels, Vrije Universiteit Brussel, Brussels 1050, Belgium
[7]KU Leuven, Department of Microbiology and Immunology, Rega Institute for Medical Research, Leuven 3000, Belgium
[8]Interdisciplinary Institute for Neuroscience, University of Bordeaux, F-33000 Bordeaux, France
[9]VIB Bio Core, KU Leuven, Leuven 3000, Belgium
[10]School of Biomedical Sciences, The University of Queensland, St Lucia Campus, Brisbane, QLD 4072, Australia
[11]Univ. Bordeaux, CNRS UMR 5293, F-33000 Bordeaux, France
[12]These authors contributed equally
[13]Lead contact
*Correspondence: soukuplab@gmail.com (S.-F.S.), patrik.verstreken@kuleuven.be (P.V.)
https://doi.org/10.1016/j.neuron.2023.02.001

## SUMMARY

Neuronal activity causes use-dependent decline in protein function. However, it is unclear how this is coupled to local quality control mechanisms. We show in *Drosophila* that the endocytic protein Endophilin-A (EndoA) connects activity-induced calcium influx to synaptic autophagy and neuronal survival in a Parkinson disease-relevant fashion. Mutations in the disordered loop, including a Parkinson disease-risk mutation, render EndoA insensitive to neuronal stimulation and affect protein dynamics: when EndoA is more flexible, its mobility in membrane nanodomains increases, making it available for autophagosome formation. Conversely, when EndoA is more rigid, its mobility reduces, blocking stimulation-induced autophagy. Balanced stimulation-induced autophagy is required for dopagminergic neuron survival, and a variant in the human ENDOA1 disordered loop conferring risk to Parkinson disease also blocks nanodomain protein mobility and autophagy both *in vivo* and in human-induced dopaminergic neurons. Thus, we reveal a mechanism that neurons use to connect neuronal activity to local autophagy and that is critical for neuronal survival.

## INTRODUCTION

Pre-synaptic terminals are complex machines that drive a multitude of functions such as memory acquisition, complex coordinated movements, and thought.[1] Synapses are densely packed with proteins and lipids[2] that power essential processes such as neurotransmitter release, changes in plasticity, endocytosis, and signaling.[3–5] Yet, synapses are often located far from neuronal cell bodies, and thus, nerve terminals need to, at least in part, locally cope with turnover of bio-molecules.[6–10]

There are several cellular "homeostasis mechanisms" that are involved in quality control and protein turnover at the synapses, including macroautophagy, where double membrane structures engulf parts of the cytoplasm destined for degradation and recycling. However, synapses are fragile, and it is likely they avoid "blunt" and "massive" turnover by gorging sizable parts of their cytoplasm. For example, based on electron microscopy studies, autophagosomes can measure up to hundreds of nanometers in diameter, and thus, a single autophagosome could engulf up to > 10%–20% of the synaptic cytoplasm at once.[11–15] Hence, it is conceivable that autophagy at synapses is a well-regulated process.

There are several synapse-specific proteins that are implicated in the creation of autophagosomes at nerve terminals, and these same proteins are not involved in autophagy elsewhere in the cell.[9,10,14–16] This includes the active zone protein


This is an open access article under the CC BY-NC-ND license (http://creativecommons.org/licenses/by-nc-nd/4.0/).

Please cite this article in press as: Bademosi et al., EndophilinA-dependent coupling between activity-induced calcium influx and synaptic autophagy is disrupted by a Parkinson-risk mutation, Neuron (2023), https://doi.org/10.1016/j.neuron.2023.02.001



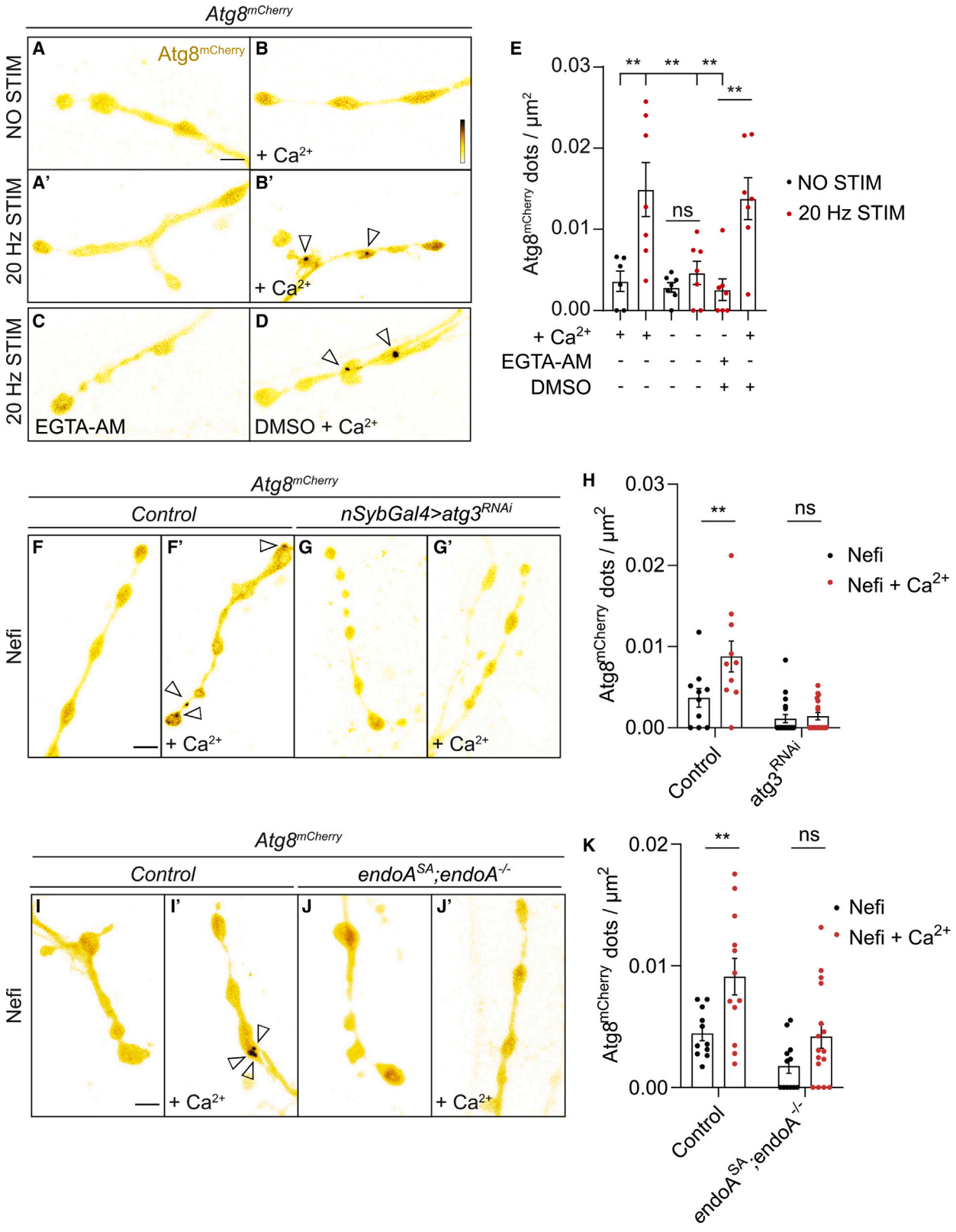


(legend on next page)

Please cite this article in press as: Bademosi et al., EndophilinA-dependent coupling between activity-induced calcium influx and synaptic autophagy is disrupted by a Parkinson-risk mutation, Neuron (2023), https://doi.org/10.1016/j.neuron.2023.02.001



CellPress
OPEN ACCESS

bassoon that binds to and sequesters Atg5, thus limiting the ability to create new autophagosomes at synapses.[17] We and others have also implicated synaptojanin-1 that dephosphorylates phosphoinositides at the autophagosomal membrane to facilitate Atg18 cycling.[8,14,18] Similarly, we found a role for endophilinA1 (EndoA1), a small BAR and SH3 domain-containing protein that, when phosphorylated by LRRK2, creates membrane docking sites for autophagic proteins such as Atg3 or Atg1.[8,15,19,20] While the important question of how key molecular pathways trigger autophagy at synapses is not answered, these discoveries are starting to reveal exciting connections to neurodegenerative disease that we do not yet fully understand. Indeed, the genes encoding synaptojanin-1 and LRRK2 have been found mutated in Parkinson disease (PD). There is also a GWAS signal close to the *LRRK2* locus and two independent GWAS signals in the vicinity of the *SH3GL2* gene that encodes human ENDOA1.[21–23] Interestingly, there is also a mutation in the intrinsically disordered loop region of ENDOA1 between the BAR and SH3 domains that confers increased risk to develop PD.[24] However, the effect of this mutation on EndoA function is unknown.

Synapses require intense metabolic activity to power the vesicle cycle and other membrane-bound processes. This also causes protein stress and damage. An interesting idea is that this stress and damage are coupled to protein and organelle turnover including that, across species, neuronal activity induces the formation of autophagosomes at synapses.[10,15,18,25–31] However, how elements of neuronal activity such as calcium influx, neurotransmitter release, or endocytosis drive the formation of autophagosomes at synaptic terminals has not been investigated.

Here, we show that neuronal stimulation-induced calcium influx is necessary and sufficient to drive the formation of autophagosomes at pre-synaptic terminals, and this is required for neuronal survival. This process is mediated by ENDOA1 and blocked by the PD risk variant, G276V, in the disordered loop region of the human protein. This region controls EndoA nanoscale organization at *Drosophila* synapses in a calcium-dependent manner, such that at rest, the protein is in the periphery, where it can promote synaptic vesicle endocytosis, while during stimulation and $Ca^{2+}$ influx, it relocalizes to the synapse lumen to facilitate autophagosome formation. We show that these changes in mobility correlate with the intrinsic dynamics of the EndoA protein: a mutation that increases flexibility, increases mobility, and drives autophagy, or a mutation that decreases flexibility, decreases mobility, and blocks synaptic autophagy. Similarly, the PD-associated mutation in the disordered loop also decreases mobility and synaptic autophagy. Using genetic interaction studies and imaging, we show there are independent routes to activate EndoA-dependent synaptic autophagy, and all are affected by proteins mutated in PD: LRRK2-dependent EndoA phosphorylation[15,32] and stimulation-induced dynamic flexibility changes in EndoA.

## RESULTS

### EndoA is required for $Ca^{2+}$-induced pre-synaptic autophagy

It is not known how neuronal activity induces autophagy at synapses.[10,15,28,29] We therefore tested if $Ca^{2+}$ influx induced by stimulation can trigger the process. We performed live confocal imaging of *Drosophila* third instar larval neuromuscular junction (NMJ) boutons expressing Atg8 fused to mCherry ($Atg8^{mCherry}$) under endogenous *atg8*-promotor control. Motor neurons were electrically stimulated within the range of their normal physiological firing ability (20 Hz).[33,34] Stimulation of 30 min induces the formation of Atg8-positive puncta (Figures 1B′ and 1E). These puncta do not form when neurons are not stimulated nor in the absence of extracellular $Ca^{2+}$ (Figures 1A, 1B, 1A′, and 1E). Likewise, Atg8-labeled structures do not form when neurons are stimulated in the presence of the membrane-permeable $Ca^{2+}$ chelator EGTA-AM (Figures 1C–1E), while they do form in presence of the vehicle (DMSO) and $Ca^{2+}$ (Figures 1D and 1E). We conclude that $Ca^{2+}$ influx upon neuronal stimulation triggers the accumulation of Atg8-labeled autophagosomes at synaptic boutons.

To find independent evidence, we used nefiracetam (Nefi), a compound that opens L/N-type $Ca^{2+}$ channels.[35–37] We confirmed that Nefi causes $Ca^{2+}$ influx at *Drosophila* NMJ boutons using GCaMP6 imaging (Figures S1A and S1B). We then incubated live NMJs with Nefi and observed that this induces autophagy in the presence of extracellular $Ca^{2+}$ but not when $Ca^{2+}$ is omitted (Figures 1F, 1F′, and 1H). To verify that the process induced by Nefi and $Ca^{2+}$ is indeed autophagy, we knocked down the essential autophagy protein Atg3 in neurons (RNAi).[15] Under these conditions, $Atg8^{mCherry}$ remains cytosolic

**Figure 1. $Ca^{2+}$ influx-induced synaptic autophagy is EndoA-dependent**

(A–E) Live imaging of non-stimulated and stimulated (30 min, 20 Hz) *Drosophila* larval NMJ boutons expressing $Atg8^{mCherry}$ at endogenous levels in the absence of $Ca^{2+}$ (A and A′), presence of $Ca^{2+}$ (B and B′), presence of EGTA-AM (no $Ca^{2+}$ in the buffer) (C), and presence of DMSO plus $Ca^{2+}$ (D). Fluorescence intensities shown using scale (0–1292 gray value) indicated in (B). Quantification of the number of $Atg8^{mCherry}$ dots (arrowheads) (E). Error bars: mean ± SEM; scale bar: 5 μm. Statistical significance: one-way ANOVA with Tukey's multiple comparison test: ** $p < 0.01$, ns, not significant, $n \geq 6$ larvae (24 NMJs) per genotype.

(F–H) Live imaging of genomically expressed $Atg8^{mCherry}$ in NMJ boutons of *w* controls (F and F′) and of animals expressing RNAi against *atg3* (under the control of the pan-neuronal driver *nSyb-Gal4*) (G and G′). Non-stimulated animals were incubated for 30 min in HL3 containing nefiracetam (Nefi) (10 μM) and post-synaptic glutamate receptor blocker 1-naphthylacetyl spermine trihydrochloride (NAS) (100 μM) to block muscle contractions (F and G). Stimulated animals were incubated for 30 min in HL3 with Nefi (10 μM), NAS (100 μM), and $CaCl_2$ (1 mM) (F′ and G′). Quantification of the number of $Atg8^{mCherry}$ dots (arrowheads) (H). Error bars: mean ± SEM; scale bar: 5 μm. Statistical significance: two-way ANOVA with Šidàk multiple comparison test: ** $p < 0.01$, ns, not significant, $n \geq 9$ larvae (36 NMJs) per genotype.

(I–K) Live imaging of genomically expressed $Atg8^{mCherry}$ in NMJ boutons of *w* control animals (I and I′) and of $endoA^{-/-}$ null mutant animals expressing phospho-dead $endoA^{S75A}$ (genomic construct) (J and J′). Quantification of the number of $Atg8^{mCherry}$ dots (arrowheads) (K). Error bars: mean ± SEM; scale bar: 5 μm. Statistical significance: two-way ANOVA with Šidàk multiple comparison test: ** $p < 0.01$, ns, not significant, $n \geq 11$ larvae (44 NMJs) per genotype. Full genotypes: see STAR Methods.

Related to Figure S1.

Please cite this article in press as: Bademosi et al., EndophilinA-dependent coupling between activity-induced calcium influx and synaptic autophagy is disrupted by a Parkinson-risk mutation, Neuron (2023), https://doi.org/10.1016/j.neuron.2023.02.001



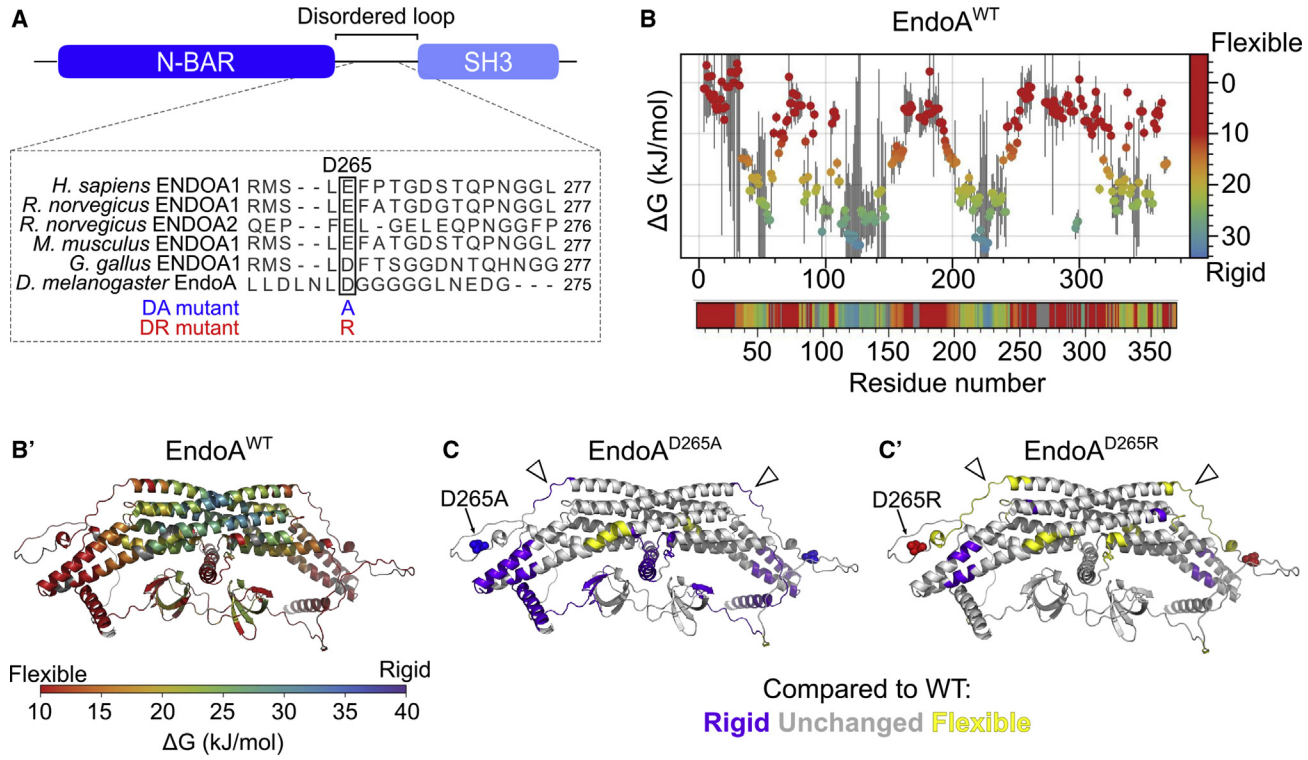


**Figure 2. D265A and D265R mutations regulate EndoA flexibility**

(A) Protein alignment showing conservation of the negatively charged glutamic acid in position 264 of Rat ENDOA2 and the negatively charged aspartic acid in position 265 of *Drosophila* EndoA.

(B and B′) Dynamics of native wild-type EndoA, at 4°C, as determined by HDX-MS experiments. HDX data (n = 2 biological × 3 technical repeats; see Table S2) were analyzed by PyHDX to obtain ΔG/residue values (see Table S3). Output ΔG values colored according to a gradient color map (as indicated) were plotted together with covariances across the linear sequence (B, top panel) or are shown in a linear box (B, bottom panel). ΔG values plotted on the AlphaFold 2.0 predicted 3D structure of dimeric EndoA (B′).

(C and C′) Differences in the dynamics of the mutant proteins relative to the wild type. HDX-MS data (n = 2 biological × 3 technical repeats; Table S2) were analyzed by PyHDX to obtain the relative fractional uptake values (rfus), i.e., all deuterium uptake values were expressed relative to the maximally deuterated sample (FD; taken as 100%) and the undeuterated sample (taken as 0%) (see Table S4). The Δrfus(wt-mutant) for the HDXtime = 10 s were plotted on the 3D structure of dimeric EndoA. The color code used only indicates positive (purple; mutant is more rigid than wild type [WT]), negative (yellow; mutant is more flexible than WT), or no difference to WT (gray). The mutated site is indicated on either protomer with (C) blue (D265A) or (C′) red (D265R) spheres. Arrowheads indicate the portion of the unstructured loop that shows opposite effect between the mutants.

Related to Figure S2 and Tables S2–S4.

(Figures 1G and 1H). Hence, $Ca^{2+}$ influx induced by Nefi induces autophagy at synapses.

EndoA is a synaptic protein involved in synaptic vesicle endocytosis.[38–41] Previous reports have suggested that the protein is responsive to $Ca^{2+}$, but the consequences and functional relevance of this are not known.[42–45] Moreover, we have previously shown that starvation-induced synaptic autophagy is blocked in $EndoA^{S75A}$.[15] Thus, we stimulated $EndoA^{S75A}$ with Nefi and $Ca^{2+}$ and found that EndoA is also required for stimulation-induced synaptic autophagy (Figures 1I–1K).

## Mutations in the intrinsically disordered loop region of EndoA control protein flexibility

Past work suggests that a negatively charged residue, E264 (in rat ENDOA2), in the disordered loop region between the BAR and SH3 domains of EndoA mediates its sensitivity to $Ca^{2+}$.[42] This amino acid is evolutionary conserved and corresponds to the negatively charged residue D265 in *Drosophila* EndoA (Figure 2A). We mutated this residue to a neutral alanine to mimic $Ca^{2+}$ unresponsiveness ($EndoA^{D265A}$) and to a positively charged arginine to mimic $Ca^{2+}$ induction ($EndoA^{D265R}$). The E264 in the unstructured loop region of rat ENDOA2 affects the binding efficiency of proteins to the EndoA-SH3 domain. We therefore assessed the ability of *Drosophila* $EndoA^{D265R}$ and $EndoA^{D265A}$ to bind (endogenous) dynamin, a well-known EndoA-interaction partner.[39] $EndoA^{D265R}$ binds significantly less dynamin than $EndoA^{WT}$, and $EndoA^{D265A}$ binds more dynamin than $EndoA^{D265R}$ (Figures S2A and S2A′). This indicates the that *Drosophila* D265 and rat E264 in endophilin-A are functional homologous residues.

We then expressed these mutant *Drosophila* proteins and wild-type EndoA in *E. coli*, purified them to homogeneity (Figure S2D), and verified the integrity of our proteins by SEC-MALS (Figure S2E). To assess if the D265 mutations cause conformational changes,[42,43] we carried out a battery of biophysical analyses, including Fourier transform infrared (FTIR)

Please cite this article in press as: Bademosi et al., EndophilinA-dependent coupling between activity-induced calcium influx and synaptic autophagy is disrupted by a Parkinson-risk mutation, Neuron (2023), https://doi.org/10.1016/j.neuron.2023.02.001



CellPress
OPEN ACCESS

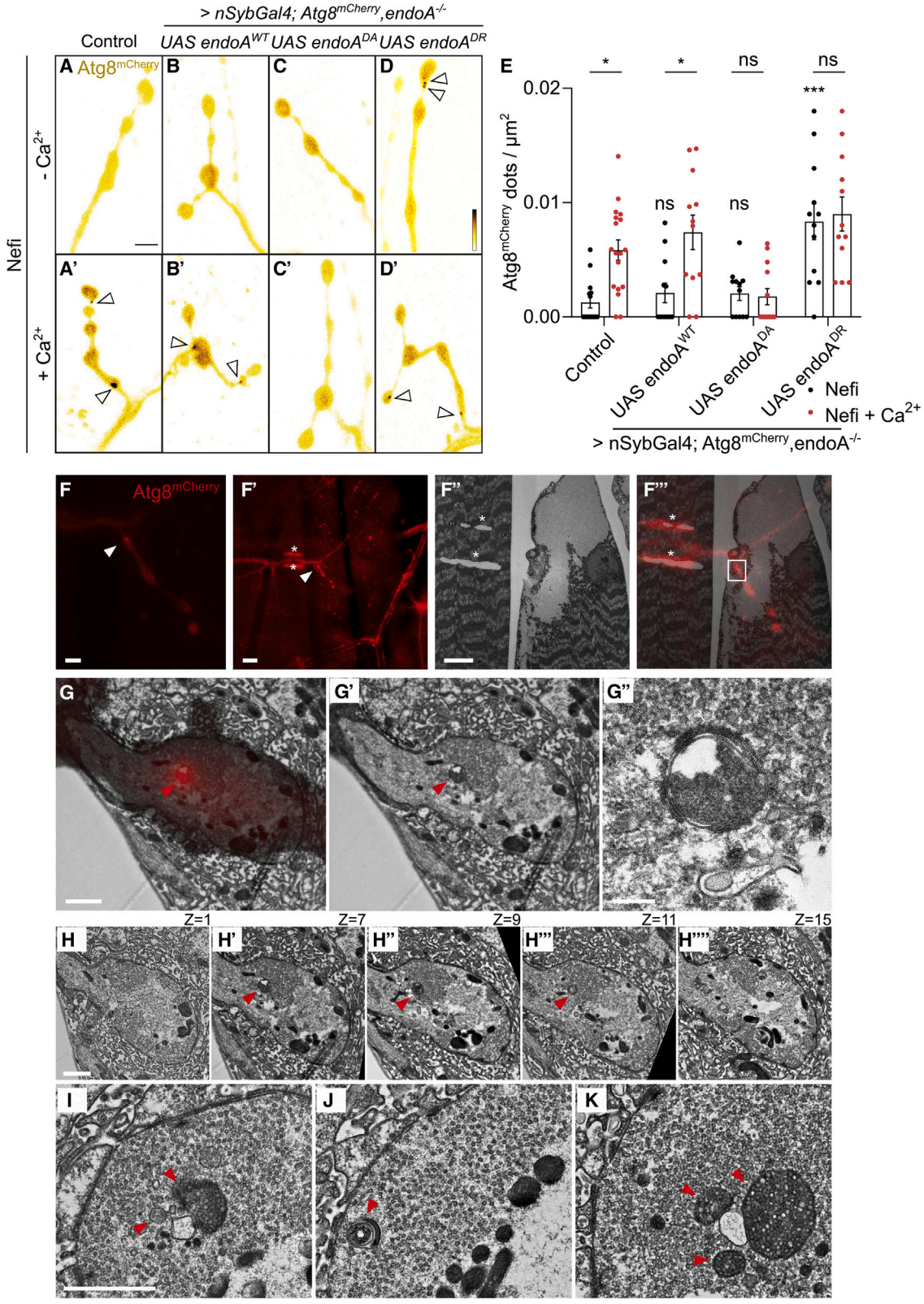


*(legend on next page)*

Please cite this article in press as: Bademosi et al., EndophilinA-dependent coupling between activity-induced calcium influx and synaptic autophagy is disrupted by a Parkinson-risk mutation, Neuron (2023), https://doi.org/10.1016/j.neuron.2023.02.001



spectroscopy, dynamic light scattering (DLS), small-angle X-ray scattering (SAXS), and assessed thermal stability (Figures S2F–S2K). However, this did not reveal significant structural differences from wild-type proteins, indicating that the mutant proteins dimerize, do not majorly affect secondary structure composition, and have similar hydrodynamic radii.

We next evaluated the intrinsic structural dynamics across the entire protein, using hydrogen deuterium exchange mass spectrometry (HDX-MS).[46,47] HDX-MS provides information, at single residue level, on protein conformational dynamics based on the exchange rate between amide hydrogens and deuterium present in the surrounding solvent (see STAR Methods). Our analyses show that wild-type EndoA is a dynamic protein with few rigid elements (Figures 2B and 2B′). By plotting the Gibbs free energy (ΔG) of each residue on the predicted AlphaFold structure of dimeric EndoA,[48] we find few rigid elements that mostly map to the dimerization interface between the two protomers (Figure 2B′). These rigid components likely stabilize the dimer, while the high degree of flexibility in the rest of the protein could mediate protein-protein (e.g., dynamin) and protein-membrane interactions critical for EndoA function. We compared the ΔG of the mutant proteins to that of wild-type EndoA and find that the EndoA$^{D265A}$ mutation, mimicking $Ca^{2+}$ unresponsiveness, increases EndoA rigidity, including in the amphipathic helices that interact with membranes and in a portion of the unstructured loop region. Conversely, the EndoA$^{D265R}$ mutation, mimicking $Ca^{2+}$ induction, increases the overall flexibility of EndoA (Figures 2C and 2C′). Hence, our data indicate that the D265R and D265A mutations cause largely opposite effects on the overall flexibility of EndoA.

## D265 in EndoA mediates $Ca^{2+}$-induced synaptic autophagy

To test if D265 mediates the $Ca^{2+}$ responsiveness of EndoA in autophagy, we generated transgenic flies and expressed EndoA$^{D265A}$, EndoA$^{D265R}$, or wild-type EndoA$^{WT}$ using a pan-neuronal driver (*nSyb-Gal4*) in *endoA*$^{-/-}$ null mutants. We show that all these conditions result in very similar expression levels compared with endogenous EndoA in control animals (Figures S3A and S3A′) and that the proteins localize to pre-synaptic terminals (below). Next, we assessed if these mutant EndoA proteins can recapitulate *in vivo* functions of the wild-type protein. Unlike *endoA*$^{-/-}$ mutants that die as larvae, neuronal expression of EndoA$^{D265A}$ or EndoA$^{D265R}$ rescues lethality and adult flies emerge (Figure S3B). However, most fail to expand their wings, suggesting the animals are weak (Figures S3C and S3C′). Additionally, *endoA*$^{-/-}$ animals that express EndoA$^{D265A}$ or EndoA$^{D265R}$ are extremely uncoordinated, and the animals die earlier than *endoA*$^{-/-}$ mutants that express EndoA$^{WT}$ (Figure S3D). Hence, these data suggest that mutations in the EndoA unstructured loop region fundamentally affect EndoA function.

*EndoA*$^{-/-}$ null mutants show a severe defect in synaptic vesicle endocytosis,[38,49,50] and we tested this in our mutants using FM 1-43 dye uptake assays. Larval fillets were incubated in FM 1-43, which is internalized into newly formed synaptic vesicles upon nerve stimulation.[51] *EndoA*$^{-/-}$ animals expressing EndoA$^{D265A}$ or EndoA$^{D265R}$ show efficient FM 1-43 dye uptake at NMJs, similar to controls (*endoA*$^{---}$ expressing EndoA$^{WT}$ or wild type; Figures S3E and S3E′). Endocytic defects in *endoA*$^{-/-}$ mutants also cause a decline in neurotransmitter release during prolonged 10 Hz stimulation.[38,52] However, excitatory junctional potential (EJP) amplitudes during low frequency stimulation (0.2 Hz–1 Hz) and during high frequency stimulation (10 Hz, 400 s) were similar across our conditions (Figures S3F and S3G). Moreover, defects in endocytosis in *endoA*$^{-/-}$ mutants severely affect vesicle replenishment at synaptic terminals,[38,49,52] but transmission electron microscopy (TEM) analyses of NMJ boutons did not reveal differences in synaptic vesicle number per area (Figures S3H and S3H′). We conclude that the D265 EndoA mutants do not affect synaptic vesicle endocytosis in a significant manner at (robust) NMJ synapses, but they cause adult flies to be uncoordinated resulting in early death. This suggests that important EndoA functions (other than endocytosis) are affected by D265.

Considering these results, we asked if $Ca^{2+}$-influx-induced synaptic autophagy might be affected and determined the distribution of Atg8$^{mCherry}$ in response to $Ca^{2+}$ influx. In non-induced conditions (absence of extracellular $Ca^{2+}$), Atg8$^{mCherry}$ remains cytosolic and does not accumulate in puncta in *endoA*$^{-/-}$ mutants that express EndoA$^{WT}$ or EndoA$^{D265A}$ (Figures 3A–3C and

**Figure 3. EndoA mutants alter $Ca^{2+}$ influx-mediated synaptic autophagy induction**

(A–E) Live imaging of genomically expressed Atg8$^{mCherry}$ at NMJ boutons of control (*nSyb-Gal4*/+) animals (A and A′) and of *endoA*$^{-/-}$ animals expressing *endoA*$^{WT}$ (B and B′), *endoA*$^{D265A}$ (C and C′), and *endoA*$^{D265R}$ (D and D′) (under the control of *nSyb-Gal4*). Non-stimulated animals were incubated for 30 min in HL3, Nefi (10 μM), and NAS (100 μM) (A–D). Stimulated animals were incubated for 30 min in HL3 containing Nefi (10 μM), NAS (100 μM), and $CaCl_2$ (1 mM) (A′–D′). Fluorescence intensities shown using scale (0–23645 gray value) indicated in (D). Arrowheads indicate Atg8$^{mCherry}$ accumulations. Scale bar: 5 μm. Quantification of the number of Atg8$^{mCherry}$ dots (arrowheads) per NMJ area (E). Error bars: mean ± SEM. Statistical significance: two-way ANOVA with Tukey's multiple comparison test: *$p < 0.05$, ***$p < 0.001$, ns, not significant, $n \geq 12$ larvae (48 NMJs) per genotype. Significance levels displayed above "Nefi" columns refer to comparison with "Nefi" treatment (unstimulated) on control animals.

(F–H) CLEM of boutons of *endoA*$^{-/-}$ animals expressing *endoA*$^{D265R}$ with *nSyb-Gal4*, as well as Atg8$^{mCherry}$ expressed at endogenous levels. (F) Single confocal slice of an example NMJ displaying an Atg8$^{mCherry}$ structure (arrowhead). Scale bar: 5 μm. (F′) Zoom out of the same NMJ shown in (F). Asterisks indicate branding marks, and arrowhead indicates Atg8$^{mCherry}$ structure. Scale bar: 20 μm. (F″) Electron micrograph of the same region as in (F′). Asterisks indicate branding marks, and arrowhead indicates Atg8$^{mCherry}$ structure. Scale bar: 10μm. (F‴) Overlay of confocal image in (F′) with electron micrograph in (F″). Asterisks indicate branding marks, and arrowhead indicates Atg8$^{mCherry}$ structure. Scale bar: 10 μm. (G and G′) Zoomed representation of the bouton containing the Atg8$^{mCherry}$ structure shown as overlay (G) and electron micrograph only (G′). Red arrowhead indicates the structure correlating with the mCherry signal. Scale bar: 1 μm. (G″) magnification. Scale bar: 200 nm. (H–H‴) Single TEM slices showing the putative autophagosomal structure visible in multiple consecutive slices (red arrowhead). Z = 1: 0, Z = 7: 42 nm, Z = 9: 560 nm, Z = 11: 700 nm, Z = 15: 980 nm. Scale bar: 1 μm.

(I–K) Examples of additional Atg8-overlapping autophagosomal structures (red arrowheads) from *endoA*$^{D265R}$ expressing animals. Scale bar: 1 μm.

Related to Figures S3 and S4.

Please cite this article in press as: Bademosi et al., EndophilinA-dependent coupling between activity-induced calcium influx and synaptic autophagy is disrupted by a Parkinson-risk mutation, Neuron (2023), https://doi.org/10.1016/j.neuron.2023.02.001



CellPress
OPEN ACCESS

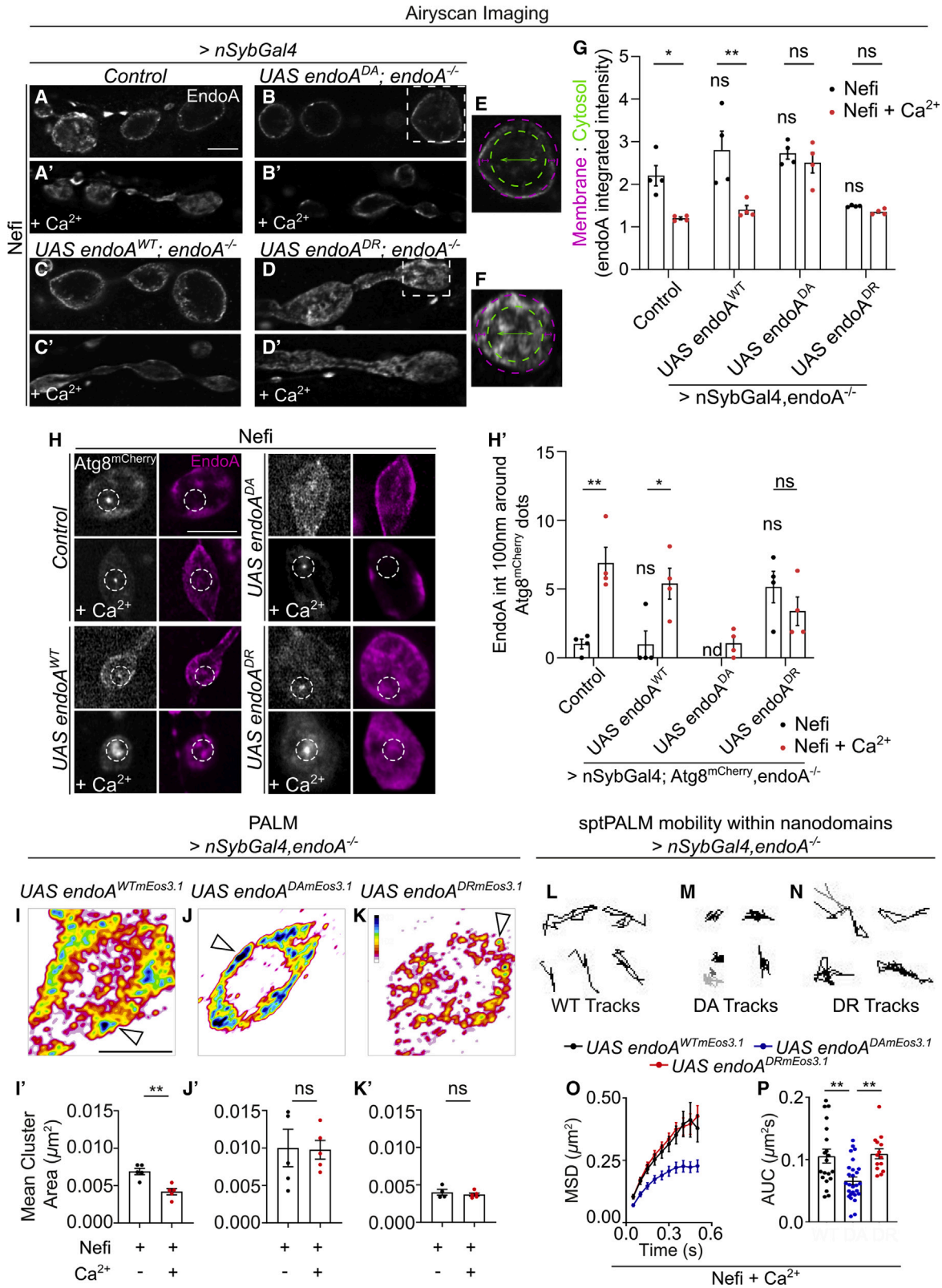


*(legend on next page)*

Please cite this article in press as: Bademosi et al., EndophilinA-dependent coupling between activity-induced calcium influx and synaptic autophagy is disrupted by a Parkinson-risk mutation, Neuron (2023), https://doi.org/10.1016/j.neuron.2023.02.001



3E). Atg8$^{mCherry}$ puncta also fail to form at Nefi and $Ca^{2+}$-induced NMJs of *endoA*$^{-/-}$ that express EndoA$^{D265A}$, indicating that, in this mutant, autophagy is blocked also during stimulation (Figures 3A′–3C′ and 3E). In contrast, Atg8$^{mCherry}$-labeled puncta do form already at uninduced NMJs of *endoA*$^{-/-}$ that express EndoA$^{D265R}$ (Figures 3D and 3E). The autophagy levels in uninduced EndoA$^{D265R}$ mutants are similar to those observed in induced controls, indicating that autophagy is constitutively activated by EndoA$^{D265R}$ (Figures 3D′ and 3E). We show this effect is dominant, as expression of EndoA$^{D265R}$ in wild-type flies upregulates synaptic autophagy (Figures S4A–S4C). Finally, we provide evidence that increased autophagosomes in EndoA$^{D265R}$ are the result of increased biogenesis: we fed animals chloroquine that blocks autophagy flux by interfering with autophagosome to lysosome fusion. Chloroquine-fed EndoA$^{D265R}$ mutants consistently show an accumulation of Atg8-labeled autophagosomes, consistent with an increase in autophagosome biogenesis, rather than a block in flux (Figure S4D).

To reveal the ultrastructure of the Atg8$^{mCherry}$-labeled structures in EndoA$^{D265R}$ mutants, we resorted to correlative light and electron microscopy (CLEM). First, we imaged Atg8$^{mCherry}$ puncta by confocal microscopy and used a two-photon laser to create branding marks around the region of interest. We used these to identify relevant boutons in block-face scanning EM and processed the samples for imaging by TEM. We then manually overlaid confocal light microscopy sections with the TEM images.[15] We found that the Atg8$^{mCherry}$ puncta overlap with structures reminiscent of degradative organelles including lysosomes and autophagosomes (Figures 3F–3K). This confirms the autophagosome/degradative nature of the Atg8$^{mCherry}$-labeled organelles that form in EndoA$^{D265R}$ animals. Taken together, these results indicate that EndoA D265 mutants are unresponsive to $Ca^{2+}$ influx and that EndoA$^{D265R}$ constitutively induces autophagy at synapses, while EndoA$^{D265A}$ is inert and fails to induce the process even upon $Ca^{2+}$ influx.

## D265 uncouples starvation and $Ca^{2+}$-induced synaptic autophagy

EndoA is required for both starvation-induced synaptic autophagy[15] and $Ca^{2+}$-induced synaptic autophagy, and this requires D265 (this work). We thus tested if D265 also mediates starvation-induced synaptic autophagy and assessed Atg8$^{mCherry}$ puncta. We starved for 4 h *endoA*$^{-/-}$ animals that express EndoA$^{D265A}$, EndoA$^{D265R}$, or Endo$^{WT}$ and compared autophagy levels with those of fed animals (Figure S4E). In contrast to the block in $Ca^{2+}$-induced autophagy in EndoA$^{D265A}$ mutants (Figures 3C, 3C′, and 3E), starvation-induced autophagy reaches a level similar to that in controls (Figure S4E). In addition, starvation induces an additive further two-fold increase in the synaptic autophagy levels in EndoA$^{D265R}$ mutants (Figures 3D, 3D′, 3E, and S4E). These data indicate that starvation and neuronal stimulation independently induce synaptic autophagy and that the D265 mutations uncouple these processes.

## $Ca^{2+}$ influx affects the nanoscale organization of EndoA at synapses

To understand how the D265 EndoA mutants affect autophagy at synapses, we determined the localization of wild-type and mutant EndoA proteins at live synapses. We took advantage of the nanoscale resolution provided by the Airy scan detector in confocal laser scanning microscopy.[53] $Ca^{2+}$ influx causes a redistribution of endogenous EndoA or EndoA$^{WT}$ neuronally expressed in *endoA*$^{-/-}$ mutants (single confocal slices in Figures 4A–4F). Wild-type EndoA moves from its preferential

**Figure 4. Synaptic nanoscale organization of EndoA is $Ca^{2+}$-influx-dependent**

(A–G) Representative images of Airyscan confocal sections of synaptic boutons of paraformaldehyde-fixed control (*nSyb-Gal4*/+) (A and A′) and *endoA*$^{-/-}$ larvae expressing *endoA*$^{D265A}$ (B and B′), *endoA*$^{WT}$ (C and C′), and *endoA*$^{D265R}$ (D and D′) (under the control of the pan-neuronal driver *nSyb-Gal4*) labeled with anti-EndoA antibody. Scale bar: 5 μm. Non-stimulated animals were incubated for 30 min in HL3, Nefi (10 μM), and NAS (100 μM) (A–D). Stimulated animals were incubated for 30 min in HL3 containing Nefi (10 μM), NAS (100 μM), and $CaCl_2$ (1 mM) (A′–D′). Zoomed in synaptic boutons (from B and D, respectively) showing quantification of EndoA intensity around the synaptic plasma membrane (magenta) and within the synaptic lumen (green) (E and F). Quantification of the EndoA-integrated intensity across genotypes indicated in (A–D) showing ratio of EndoA intensity at the membrane to that in the lumen (G). Error bars represent mean ± SEM; statistical significance: two-way ANOVA with Tukey's multiple comparison test: * $p < 0.05$, ** $p < 0.01$, ns, not significant, $n \geq 4$ larvae (16 NMJs) per genotype. Significance levels displayed above "Nefi" columns refer to comparison with "Nefi" treatment (unstimulated) with control animals.

(H and H′) Representative images of Airyscan confocal sections of individual synaptic boutons of paraformaldehyde-fixed control (*nSyb-Gal4*/+) in stimulated and non-stimulated conditions, labeled with anti-EndoA antibody and expressing Atg8$^{mCherry}$ at endogenous levels. Scale bar: 5 μm. Only synaptic boutons with Atg8$^{mCherry}$ puncta (dotted circles) indicative of autophagosomes were selected, and EndoA-integrated density in a radius of 100 nm from the Atg8$^{mCherry}$ puncta was measured. (H′) Quantification of the normalized integrated EndoA intensity across genotypes indicated in (A–D) showing EndoA intensity 100 nm around Atg8$^{mCherry}$ puncta. Data from all genotypes were normalized to control (*nSyb-Gal4*/+) unstimulated data. Error bars represent mean ± SEM; statistical significance: two-way ANOVA with Tukey's multiple comparison test: * $p < 0.05$, ** $p < 0.01$, ns, not significant, nd, no data, $n \geq 4$ larvae (16 NMJs) per genotype.

(I–K) Transgenic *endoA*$^{-/-}$ larvae expressing *endoA*$^{WT}$::mEos3.1, *endoA*$^{D265A}$::mEos3.1, or *endoA*$^{D265R}$::mEos3.1 (*nSyb-Gal4*) were imaged using single molecule localization photoactivated localization microscopy (PALM) at 20 Hz. Representative images show cluster map color coded for cluster size and density distribution of *endoA*$^{::mEos3.1}$ generated by density-based spatial clustering of applications with noise (DBSCAN) analysis. Arrowheads indicate EndoA nanodomains. Fluorescence intensity shown using indicated scale (2–203). Scale bar: 2 μm. (I′–K′) Quantification of the mean cluster area of *endoA*$^{WT}$::mEos3.1, *endoA*$^{D265A}$::mEos3.1, and *endoA*$^{D265R}$::mEos3.1 in non-stimulated and stimulated conditions. Error bars: mean ± SEM; statistical significance: Student's t test two-tailed unpaired distribution: ** $p < 0.01$, ns, not significant, $n \geq 5$ larvae (20 NMJs) per genotype.

(L–N) Transgenic *endoA*$^{-/-}$ larvae expressing *endoA*$^{WT}$::mEos3.1, *endoA*$^{D265A}$::mEos3.1, or *endoA*$^{D265R}$::mEos3.1 (*nSyb-Gal4*) were imaged using single-particle tracking photoactivated localization microscopy (sptPALM) at 20 Hz. Representative trajectories located within EndoA nanodomains in NMJ boutons of *endoA*$^{-/-}$ larvae expressing *endoA*$^{WT}$::mEos3.1 (L), *endoA*$^{D265A}$::mEos3.1 (M), and *endoA*$^{D265R}$::mEos3.1 (N).

(O) This is quantified for each genotype as mean square displacement (MSD) as a function of time.

(P) Quantification of the area under the MSD curve ($\mu m^2 s$). Error bars: mean ± SEM; statistical significance: one-way ANOVA with Tukey's multiple comparison test: ** $p < 0.01$, $n \geq 4$ larvae ($n \geq 14$ nanodomains) per genotype.

Related to Figures S5 and S6 and Video S1.

Please cite this article in press as: Bademosi et al., EndophilinA-dependent coupling between activity-induced calcium influx and synaptic autophagy is disrupted by a Parkinson-risk mutation, Neuron (2023), https://doi.org/10.1016/j.neuron.2023.02.001



CellPress
OPEN ACCESS

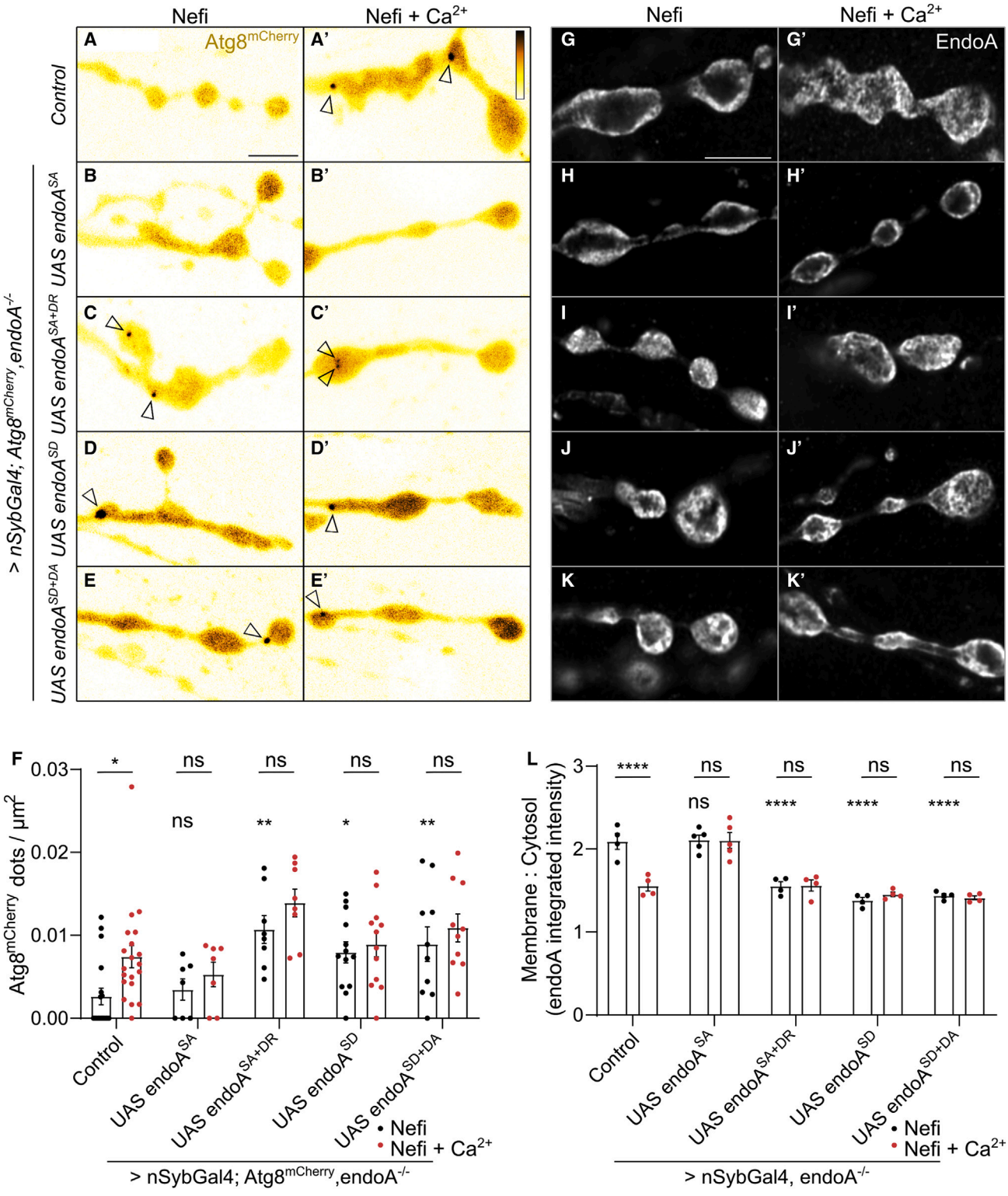


**Figure 5. $Ca^{2+}$ and EndoA phosphorylation independently induce autophagy**

(A–F) Live imaging of genomically expressed $Atg8^{mCherry}$ in NMJ boutons of control (*nSyb-Gal4*/+) animals (A and A′) and of $endoA^{-/-}$ animals expressing $endoA^{S75A}$ (B and B′), $endoA^{S75A+D265R}$ (C and C′), $endoA^{S75D}$ (D and D′), and $endoA^{S75D+D265A}$ (E and E′) (*nSyb-Gal4*). Non-stimulated animals were incubated for 30 min in HL3, Nefi (10 µM), and NAS (100 µM) (A–E). Stimulated animals were incubated for 30 min in HL3 containing Nefi (10 µM), NAS (100 µM), and $CaCl_2$ (1 mM) (A′–E′). Fluorescence intensities shown using scale (300–2441 gray value) indicated in (A′). Arrowheads indicate $Atg8^{mCherry}$ puncta. Scale bar: 5 µm. (F)

*(legend continued on next page)*

Please cite this article in press as: Bademosi et al., EndophilinA-dependent coupling between activity-induced calcium influx and synaptic autophagy is disrupted by a Parkinson-risk mutation, Neuron (2023), https://doi.org/10.1016/j.neuron.2023.02.001



peripheral localization toward the synaptic bouton lumen (Figures 4A, 4A′, 4C, 4C′, and 4G). Interestingly, EndoA$^{D265A}$ remains mostly at the bouton periphery even upon $Ca^{2+}$ influx (Figures 4B, 4B′, 4E, and 4G). Conversely, EndoA$^{D265R}$ is distributed across the bouton already at rest (Figures 4D–4G). In contrast to wild-type EndoA, the distribution of EndoA$^{D265A}$ or EndoA$^{D265R}$ does not change upon $Ca^{2+}$ influx, confirming these mutants are $Ca^{2+}$ insensitive. We next asked whether the redistribution of EndoA would cause increased localization of the protein close to Atg8$^{mCherry}$-labeled autophagosomes. We therefore expressed Atg8$^{mCherry}$ and quantified the amount of EndoA in the 100 nm zone around specified Atg8$^{mCherry}$ puncta. As predicted, EndoA localizes more in the proximity of Atg8$^{mCherry}$-labeled structures in response to $Ca^{2+}$ influx and when harboring the D265R mutation. Conversely, significantly less EndoA localizes around (rare) Atg8$^{mCherry}$-labeled structures in unstimulated boutons or in EndoA$^{D265A}$ mutants (Figures 4H and 4H′). These data suggest that increased $Ca^{2+}$ influx enables EndoA redistribution, including to the vicinity of synaptic autophagosomes.

To further understand the movements of EndoA at the bouton periphery, we resorted to photoactivated localization microscopy (PALM) under oblique illumination that was developed by us for *Drosophila* NMJs.[14,54,55] This technology allows the tracking of proteins tagged with photoconvertible fluorescent probes at < 50-nm resolution and within 200–400 nm proximity to the synaptic plasma membrane.[56] We tagged wild-type, EndoA$^{D265A}$, and EndoA$^{D265R}$ mutants with mEOS3.1 and expressed the proteins in *endoA*$^{-/-}$ mutants. mEOS is a photoconvertible fluorescent protein whose stochastic change in emission spectrum from green to red allows for single molecule localization.[57,58] Animals were or were not stimulated with Nefi and $Ca^{2+}$ and fixed and analyzed by PALM (Figures S5A and S5A‴). Interestingly, wild-type EndoA$^{WT::mEos3.1}$ organizes in "hotspots" or "nanometer-sized clusters of proteins—nanodomains" at the bouton periphery (Figure S5A‴). These EndoA$^{WT::mEos3.1}$ nanodomains are significantly smaller when NMJs are stimulated or when imaging EndoA$^{D265R::mEos3.1}$ as compared with unstimulated samples or when imaging EndoA$^{D265A::mEos3.1}$ (Figures 4I′–4K′ and S5B–S5D′). Our data are consistent with the idea that the more rigid EndoA$^{D265A}$ has opportunity to interact with the membrane and other proteins in the periphery, including dynamin (Figures S2A and S2A′), and is thus more confined within larger nanodomains located (juxta)membrane (Figures 4B, 4B′, and 4G). Conversely, the more flexible EndoA$^{D265R}$ is increasingly localized to the synaptic lumen and thus away from the nanodomains (Figures 4D, 4D′, and 4G).

To find further evidence for this model, we characterized the re-arrangements of EndoA in nanodomains upon $Ca^{2+}$ influx using live single-particle tracking PALM (sptPALM) (Figures S6A–S6B′).[58] We incubated NMJs with Nefi and $Ca^{2+}$ and tracked individual EndoA$^{WT::mEos3.1}$, EndoA$^{D265A::mEos3.1}$, or EndoA$^{D265R::mEos3.1}$ molecules (neuronally expressed in *endoA*$^{-/-}$) and plotted their trajectory maps (Figures 4L–4N; Video S1). We first confirmed the existence of EndoA nanodomains at the bouton periphery using the high-resolved intensity maps that are generated during the sptPALM processing (Figures S6C and S6C′). Then, we assessed the mobility behavior of EndoA in these nanodomains by analyzing the mean square displacement (MSD) of the single proteins within the nanodomains. This parameter reveals the level of confinement of motion. Upon $Ca^{2+}$ influx, EndoA$^{D265A::mEos3.1}$ is significantly more confined within these nanodomains than EndoA$^{WT::mEos3.1}$ or EndoA$^{D265R::mEos3.1}$ (Figures 4O and 4P). We reach a similar conclusion when analyzing the instantaneous diffusion coefficients of EndoA across entire NMJs, revealing increased mobility of EndoA$^{WT::mEos3.1}$ in response to $Ca^{2+}$ influx, while EndoA$^{D265R::mEos3.1}$ and EndoA$^{D265A::mEos3.1}$ are insensitive (Figures S6D–S6F‴). Mechanistically, these results indicate that the D265A mutation confines the more rigid EndoA in nanodomains at the bouton periphery and that $Ca^{2+}$ influx alters the diffusion of EndoA such that it localizes to the bouton lumen.

## EndoA D265R induces synaptic autophagy independent of S75 phosphorylation

We previously showed that LRRK2-dependent S75 phosphorylation of EndoA drives synaptic autophagy,[8,15] and we wondered if this intersects with EndoA-dependent stimulation-induced autophagy. We therefore combined phospho-mimetic S75D that constitutively drives synaptic autophagy, with D265A that blocks synaptic autophagy (EndoA$^{S75D,\ D265A}$). We also combined the phospho-dead S75A mutation that inhibits synaptic autophagy with D265R that constitutively induces autophagy (EndoA$^{S75A,\ D265R}$) and expressed these EndoA double mutants in neurons (*nSyb-Gal4*) of *endoA*$^{-/-}$ null flies (Figures 5A–5E′). In contrast to EndoA$^{S75A}$ single mutants (Figures 5B, 5B′, and 5F), autophagy is constitutively induced in EndoA$^{S75A,\ D265R}$ double mutants (Figures 5C, 5C′, and 5F), suggesting D265R is epistatic to S75A (Figure 5F). In addition, while synaptic autophagy is blocked in EndoA$^{D265A}$, autophagy is constitutively induced in EndoA$^{S75D,\ D265A}$ double mutants (Figures 5D–5F), indicating S75D is epistatic to D265A.

We next assessed the distribution of the EndoA single and double mutants within synaptic boutons (Figures 5G–5L). While

Quantification of the number of Atg8$^{mCherry}$ puncta (arrowheads) per NMJ area. Error bars: mean ± SEM. Statistical significance: two-way ANOVA with Tukey's multiple comparison test: * $p < 0.05$, ** $p < 0.01$, ns, not significant, $n \geq 8$ larvae (32 NMJs) per genotype. Significance levels displayed above "Nefi" columns refer to comparison with "Nefi" treatment (unstimulated) with control animals.

(G–L) Representative images of Airyscan confocal sections of synaptic boutons of paraformaldehyde-fixed control (*nSyb-Gal4*/+) (G and G′) and *endoA*$^{-/-}$ larvae expressing *endoA*$^{S75A}$ (H and H′), *endoA*$^{S75A+D265R}$ (I and I′), *endoA*$^{S75D}$ (J and J′), and *endoA*$^{S75D+D265A}$ (K and K′) (*nSyb-Gal4*) labeled with anti-EndoA antibody. Scale bar: 5μm. Non-stimulated animals were incubated for 30 min in HL3, Nefi (10 μM), and NAS (100 μM) (G–K). Stimulated animals were incubated for 30 min in HL3 containing Nefi (10 μM), NAS (100 μM), and $CaCl_2$ (1 mM) (G′–K′). Quantification of the EndoA-integrated intensity across genotypes (G–K) showing ratio of EndoA intensity at the membrane to that in the lumen (L). Error bars: mean ± SEM; statistical significance: two-way ANOVA with Tukey's multiple comparison test: ****$p < 0.0001$, ns, not significant, $n \geq 4$ larvae (16 NMJs) per genotype. Significance levels displayed above "Nefi" columns refer to comparison with "Nefi" treatment (unstimulated) with control animals.

Please cite this article in press as: Bademosi et al., EndophilinA-dependent coupling between activity-induced calcium influx and synaptic autophagy is disrupted by a Parkinson-risk mutation, Neuron (2023), https://doi.org/10.1016/j.neuron.2023.02.001



CellPress
OPEN ACCESS

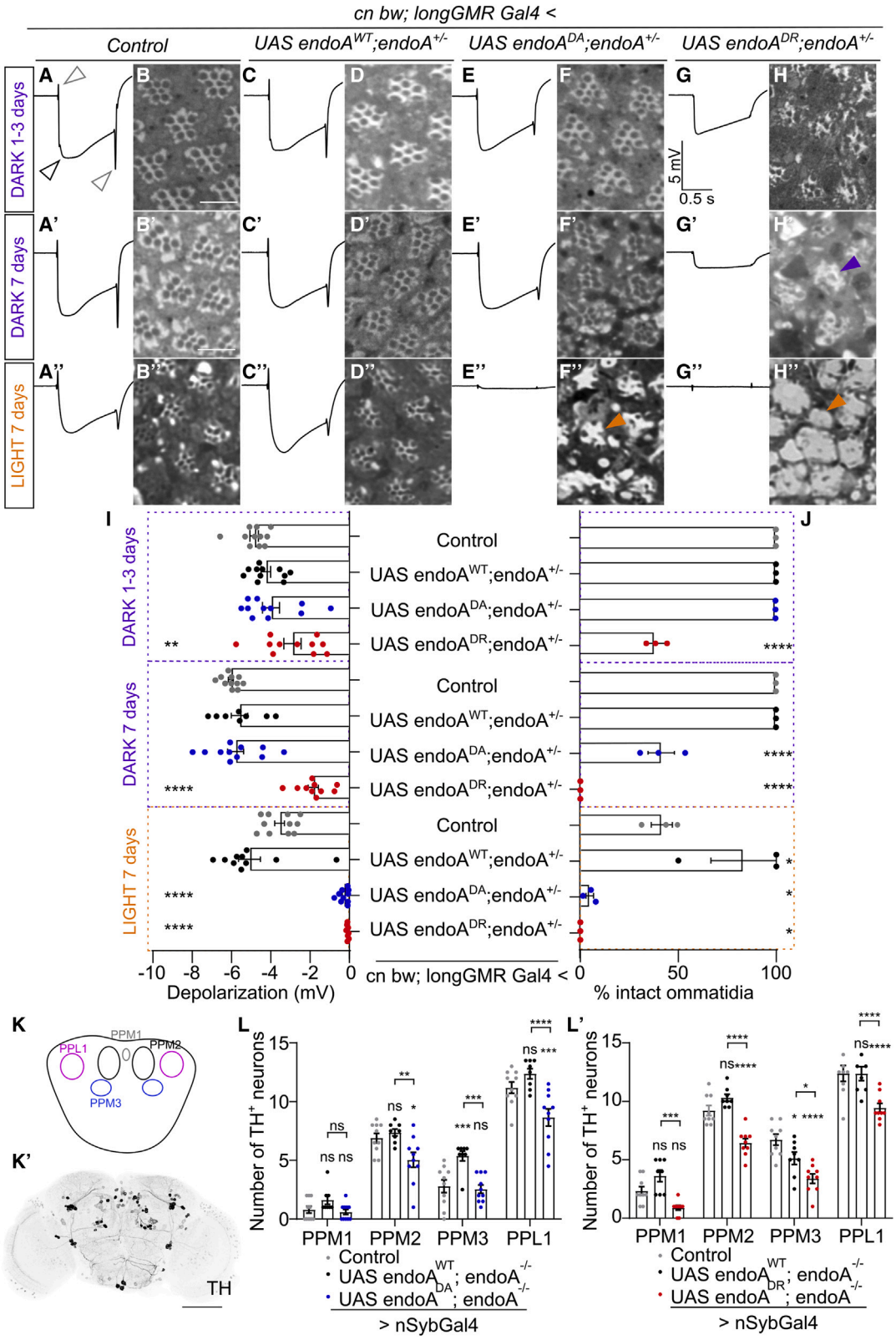


*(legend on next page)*

Please cite this article in press as: Bademosi et al., EndophilinA-dependent coupling between activity-induced calcium influx and synaptic autophagy is disrupted by a Parkinson-risk mutation, Neuron (2023), https://doi.org/10.1016/j.neuron.2023.02.001



$Ca^{2+}$ influx causes endogenous EndoA to redistribute toward the synaptic lumen (Figures 5G, 5G′, and 5L), phospho-dead $EndoA^{S75A}$ remains predominantly localized in the juxta-membrane (Figures 5H, 5H′, and 5L), similar to $EndoA^{D264A}$. Conversely, phospho-mimetic $EndoA^{S75D}$ already distributes across the bouton even without stimulation (Figures 5J, 5J′, and 5L), similar to $EndoA^{D264R}$. Interestingly, both the double mutants, $EndoA^{S75A,\ D265R}$ and $EndoA^{S75D,\ D265A}$, which both constitutively induce synaptic autophagy are constitutively distributed to the synapse lumen (Figures 5I, 5I′, 5K, 5K′, and 5L). Thus, both the genetic interactions and localization data are supporting the idea that induction of synaptic autophagy by phosphorylation or $Ca^{2+}$ influx are independent, parallel events that can override each other.

## EndoA D265 mutations cause neurodegeneration

Having characterized the involvement of EndoA in synaptic autophagy, we turned to examine its potential implication in neurodegeneration as defects in autophagy are frequently connected to these disorders.[59,60] We specifically tested if defects in stimulation-induced synaptic autophagy led to neuronal demise by assessing neuronal integrity in *endoA*$^{+/-}$ mutants expressing $EndoA^{D265R}$, $EndoA^{D265A}$, or $EndoA^{WT}$ in photoreceptors (*longGMR-Gal4*). We started by placing animals for 3 or 7 days in constant dark to avoid retinal stimulation and then recorded electroretinograms (ERGs). ERGs measure the depolarization of photoreceptors in response to a brief (1 s) light pulse. Smaller amplitudes of the ''on'' and ''off'' transients at the onset and conclusion of the light pulse are a measure of defective neurotransmitter release in the eye, while a reduced amplitude of the overall depolarization is a measure of neurodegeneration.[15,61,62] The amplitude of depolarization in 3-day-old and 7-day-old control and $EndoA^{D265A}$ flies is similar, but $EndoA^{D265R}$ flies already show a clear age-dependent reduction in ERG amplitude when kept in dark conditions (Figures 6A, 6A′, 6C, 6C′, 6E, 6E′, 6G, 6G′, and 6I). We also placed the flies in constant light to cause light-induced stress and repeated this experiment. While control and *endoA*$^{+/-}$ flies expressing $EndoA^{WT}$ are fine, now both $EndoA^{D265A}$ and $EndoA^{D265R}$ flies show strongly reduced ERG depolarization amplitudes (Figures 6A′, 6C″, 6E″, 6G″, and 6I), a hallmark of neurodegeneration. Furthermore, we find reduced amplitudes of the ''on'' and ''off'' transients in both $EndoA^{D265A}$ and $EndoA^{D265R}$ compared with $EndoA^{WT}$ (Figures S3I and S3J). This indicates additional defects in neurotransmission, but we cannot rule out that this is caused because of ensuing neurodegeneration.

To further corroborate our findings, we also evaluated neuronal morphology in toluidine blue-stained retinal sections. Quantification of the number of intact ommatidia with seven visible photoreceptors also shows age-dependent degeneration in 7-day-old dark-reared $EndoA^{D265R}$-expressing flies and in $EndoA^{D265R}$- and $EndoA^{D265A}$-expressing flies kept for 7 days in constant light, supporting our ERG recordings (Figures 6B–6H′ and 6J). These data further indicate that expression of $EndoA^{D265R}$ is a more severe condition than $EndoA^{D265A}$ but that both $EndoA^{D265R}$ and $EndoA^{D265A}$ cause neurodegeneration. They also provide evidence that EndoA is required for neuronal survival.

Given the connections between EndoA and PD,[24] we assessed if $EndoA^{D265A}$ or $EndoA^{D265R}$ affect the integrity of dopaminergic neurons in the fly brain (Figures 6K–6L′). Quantification of the number of anti-TH-positive neuronal cell bodies in different dopaminergic neuron clusters (including PPM2, PPM3, and PPL1) shows a significant reduction in both D265 mutants compared with age-matched controls (see STAR Methods; Figures 6L and 6L′). Hence, EndoA D265 is also critical for dopaminergic neuron survival.

## A Parkinson disease-risk variant in *SH3GL2* impairs $Ca^{2+}$-induced synaptic autophagy

In addition to GWAS signals in the vicinity of the *SH3GL2* gene,[24,63–65] there is also a risk-conferring missense mutation in the *SH3GL2* gene of patients with PD that encodes a glycine to valine transition at position 276.[24] This is very proximal to the autophagy controlling D265 position (E264 in ENDOA1) (Figure 7A). We thus speculated that the EndoA1 risk mutation also affects $Ca^{2+}$ influx-induced synaptic autophagy.

**Figure 6. EndoA D265 mutants induce neurodegeneration**

(A–G″) Representative electroretinogram (ERG) traces recorded from control (*cn bw; longGMR Gal4*/+) and *endoA*$^{+/-}$ mutants expressing $endoA^{WT}$, $endoA^{D265A}$, or $endoA^{D265R}$ (*longGMR-Gal4*). *Cn bw* mutations remove the protective eye pigmentation. Prior to ERG recordings, animals were exposed to 1–3 (A, C, E, and G) or 7 days of constant dark (A′, C′, E′, and G′) or 7 days of constant light (A″, C″, E″, and G″). Average traces are depicted in black. Gray arrowhead: on and off transients and black arrowhead: depolarization.

(B–H″) Histological sections of retinas of flies exposed for 1–3 (B, D, F, and H) or 7 days to constant dark (B′, D′, F′, and H′) or constant light (B″, D″, F″, and H″) stained with toluidine blue. Arrowheads indicate morphologically abnormal ommatidia. Scale bar: 10 μm.

(I) Quantification of ERG depolarization amplitude recorded upon a 1 s light pulse in flies exposed to dark or light. Bars show mean ± SEM. Statistical significance: one-way ANOVA with Tukey's multiple comparison test: *p < 0.05, **p < 0.01, ****p < 0.0001. Significance level refers to the difference to the control (*cn bw; longGMR Gal4*/+) of the indicated condition (light or dark). Recorded flies per condition ≥ 8.

(J) Quantification of the number of intact ommatidia (expressed in percenatge of the total) where all 7 rhabdomeres are visible. Bars show mean ± SEM. Statistical significance: one-way ANOVA with Tukey's multiple comparison test: *p < 0.05, **p < 0.01, ****p < 0.0001. Significance level refers to the difference to the control (*cn bw; longGMR Gal4*/+) of the indicated condition (light or dark). Single data points represent the average percentage of intact ommatidia of three histological sections of three animals per condition.

(K) Schematic of dopaminergic neuron organization in clusters in the fly brain (posterior view).

(K′) Representative maximum projection confocal image of a control brain stained with anti-TH antibody revealing dopaminergic neurons. Scale bar: 100 μm.

(L and L′) Quantification of the number of $TH^+$ neurons in the indicated clusters in aged brains. Experimental time points were defined based on the survival of the mutant animals: $endoA^{D265A}$ expressing flies and respective controls were tested at 23–25 days old; $endoA^{D265R}$ expressing flies and respective controls were tested at 1–2 days old. Bars show mean ± SEM. Statistical significance indicated above each column refers to the comparison to the control (*nSybGal4*/+) of each cluster and calculated with a two-way ANOVA: *p < 0.05, **p < 0.01, ***p < 0.001, ****p < 0.0001, ns not significant.

Please cite this article in press as: Bademosi et al., EndophilinA-dependent coupling between activity-induced calcium influx and synaptic autophagy is disrupted by a Parkinson-risk mutation, Neuron (2023), https://doi.org/10.1016/j.neuron.2023.02.001



CellPress
OPEN ACCESS

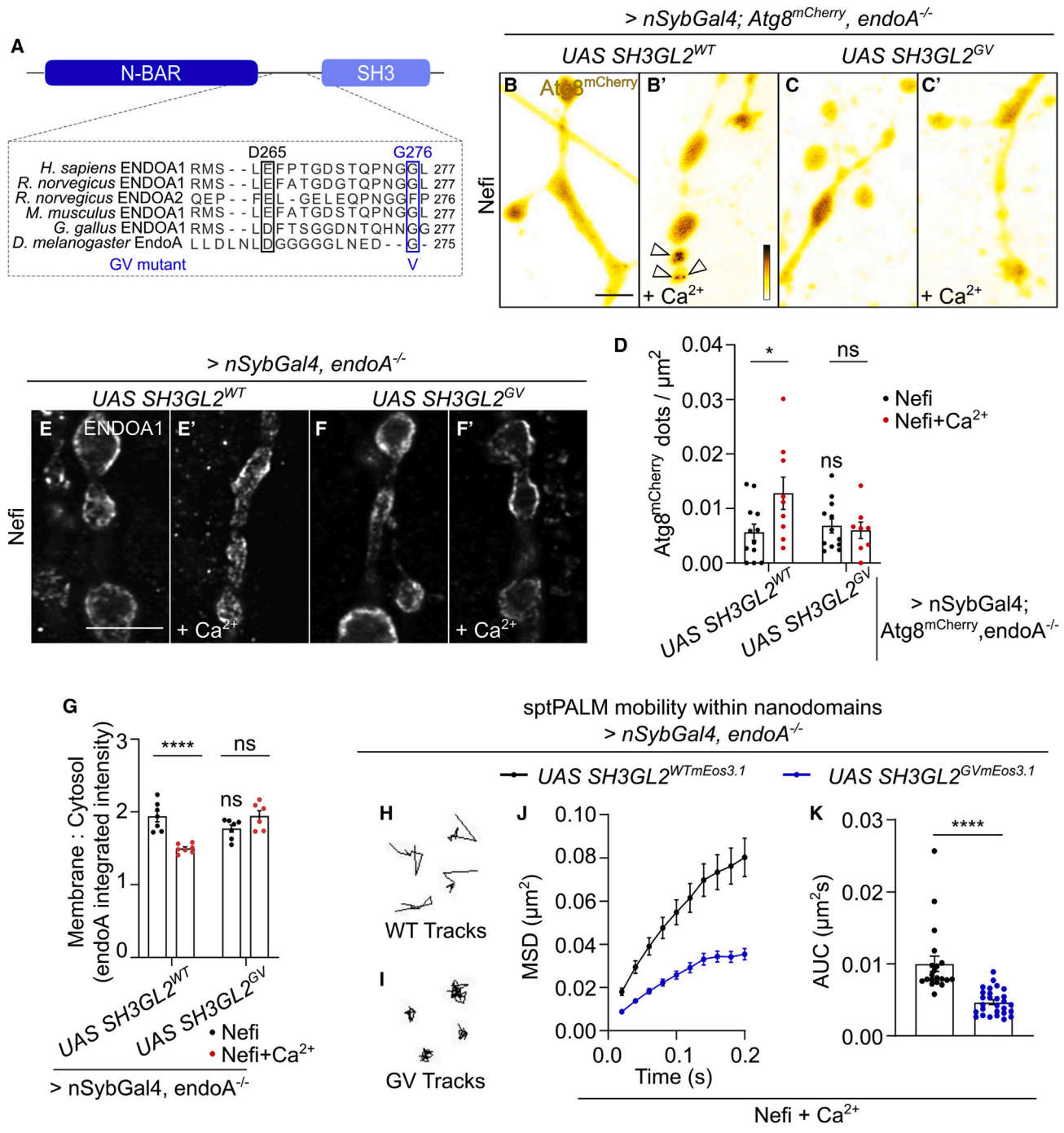


**Figure 7. *SH3GL2* Parkinson disease coding variant impairs $Ca^{2+}$-induced synaptic autophagy**

(A) Protein alignment showing evolutionary conservation of glycine 276 in the unstructured loop region of *Human* ENDOA1 and the proximity to the aspartic acid at position 265 (corresponding to glutamic acid 264 in *Human* ENDOA1).

(B–C′) Representative live confocal images of NMJ boutons of *endoA*$^{-/-}$ animals expressing Atg8$^{mCherry}$ at endogenous levels and *SH3GL2*$^{WT}$ or *SH3GL2*$^{G276V}$ (*nSyb-Gal4*). Non-stimulated animals were incubated for 30 min in HL3, Nefi (10 µM), and NAS (100 µM) (B and C). Stimulated animals were incubated for 30 min in HL3 containing Nefi (10 µM), NAS (100 µM), and $CaCl_2$ (1 mM) (B′ and C′). Fluorescence intensities shown using scale (0–65535 gray value) indicated in (B′). Arrowheads indicate Atg8$^{mCherry}$ positive autophagosomes. Scale bar: 5 µm.

(D) Quantification of the number of Atg8$^{mCherry}$ puncta per NMJ area. Error bars: mean ± SEM. Statistical significance: two-way ANOVA with Tukey's multiple comparison test: * $p < 0.05$, ns, not significant, $n \geq 8$ larvae (32 NMJs) per genotype. Significance level displayed above "Nefi" column refers to comparison with "Nefi" treatment (unstimulated) on control animals.

*(legend continued on next page)*

Please cite this article in press as: Bademosi et al., EndophilinA-dependent coupling between activity-induced calcium influx and synaptic autophagy is disrupted by a Parkinson-risk mutation, Neuron (2023), https://doi.org/10.1016/j.neuron.2023.02.001



We first verified the stability of recombinant ENDOA1$^{G276V}$ and ENDOA1$^{WT}$ by SAXS and find no large conformational differences (Figure S7A) or folding problems (Figure S7B). Furthermore, and similar to *Drosophila* EndoA$^{D265A}$, we find slightly more binding of ENDOA1$^{G276V}$ to *Drosophila* or human dynamin/dynamin1, but the difference is not significant (Figures S2B–S2C′). We then generated *endoA*$^{-/-}$ flies neuronally expressing human ENDOA1$^{WT}$ and ENDOA1$^{G276V}$ and show the constructs are expressed to a similar level based on quantitative real-time PCR and western blotting (Figures S7C–S7D′). We also show that the human proteins localize to fly synapses (see below) and, based on FM 1-43 dye uptake assays, find no significant differences in endocytosis of synaptic vesicles in animals expressing ENDOA1$^{G276V}$ compared with ENDOA1$^{WT}$ or wild-type controls (Figures S7E and S7E′). Together, these results indicate that the G276V mutation does not destabilize ENDOA1, that human ENDOA1 can functionally replace *Drosophila* EndoA when expressed in flies, and that the G276V mutation does not strongly affect synaptic vesicle endocytosis under the tested conditions.

To then assess if stimulation-induced synaptic autophagy is affected by the G276V pathogenic mutation, we quantified the number of Atg8$^{mCherry}$ puncta upon induction by $Ca^{2+}$ influx. While *endoA*$^{-/-}$ mutants expressing ENDOA1$^{WT}$ show robust Atg8$^{mCherry}$-labeled puncta (Figures 7B, 7B′, and 7D), ENDOA1$^{G276V}$-expressing animals fail to upregulate autophagy, also when stimulated (Figures 7C and 7D). These data indicate that the G276V mutation in ENDOA1 impairs $Ca^{2+}$ influx-induced synaptic autophagy.

We then determined the sub-synaptic localization of the human protein at *Drosophila* synapses using Airy scan confocal imaging. While $Ca^{2+}$ influx causes ENDOA1$^{WT}$ to redistribute from the periphery to a more luminal localization (Figures 7E, 7E′, and 7G), ENDOA1$^{G276V}$ remains confined to the periphery (Figures 7F and 7G). To further characterize these observations, we also assessed ENDOA1 nanoscale localization using sptPALM. We generated *endoA*$^{-/-}$ animals expressing ENDOA1$^{WT::mEos3.1}$ or ENDOA1$^{G276V::mEos3.1}$. Like *Drosophila* EndoA$^{WT::mEos3.1}$, human ENDOA1$^{WT::mEos3.1}$ localizes in synaptic nanodomains (Figures S7F–S7F‴). While the MSD of ENDOA1$^{WT::mEos3.1}$ within these nanodomains increases significantly upon $Ca^{2+}$ influx, ENDOA1$^{G276V::mEos3.1}$ remains more confined (Figures 7H–7K). Analyzing the instantaneous diffusion coefficients across the entire NMJs shows increased mobility of ENDOA1$^{WT::mEos3.1}$ upon $Ca^{2+}$ influx while ENDOA1$^{G276V::mEos3.1}$ is unresponsive (Figures S7G–S7H‴). Hence, the behavior of pathogenic mutant ENDOA1$^{G276V::mEos3.1}$ at synapses is very similar to that of *Drosophila* EndoA$^{D265A::mEos3.1}$, both of which block stimulation-induced autophagy.

To test the validity of our result in human cells, we investigated the role of the ENDOA1$^{G276V}$ mutation in induced human dopaminergic neurons. Therefore, we generated ENDOA1$^{G276V}$ homozygous knockin mutations by CRISPR-Cas9-facilitated homologous recombination in Ctrl65 "wild-type[66]" induced pluripotent stem cells (iPSCs) (Figures 8A, 8A′, S8A, and S8B). Then, ventral midbrain dopaminergic neurons (vmDAns) were produced using an optimized protocol for midbrain floor plate differentiation (Figure S8C). Terminal differentiation until day 60 ultimately yields ~50% of TH-positive neurons for both unedited and ENDOA1$^{G276V}$ mutant cells (Figures 8B and 8B′). We confirmed by western blot that the level of wild-type and mutant ENDOA1 in differentiated neurons is statistically indistinguishable, indicating that the mutant human protein is stable (Figures 8C and 8C′). Both wild-type and mutant cells are spontaneously active and fire action potentials to a similar extent, as verified by $Ca^{2+}$ imaging (Figures 8D and 8D″). We then assessed autophagy in these endogenously active cells by quantifying the number of lipidated LC3B puncta, based on antibody labeling within TH-positive (vmDAn) neurites.[13,67] This shows significantly less autophagosomes in ENDOA1$^{G276V}$ mutant neurons compared with control neurons (Figures 8E and 8E′). Hence, these results support the conclusion that the PD risk-conferring variant ENDOA1$^{G276V}$ impairs autophagy in neurites of active (induced) vmDAns.

## DISCUSSION

This work reveals that EndoA links neuronal activity-dependent $Ca^{2+}$ influx to synaptic autophagy and that a human mutation in the unstructured loop region of EndoA conferring risk to PD disrupts this process.

Synapses require regulated turnover systems to maintain protein homeostasis, and disrupting this process causes synaptic and—ultimately—neuronal degeneration.[7,14,15] There are several reasons why synapses are vulnerable, including that they need to cope with metabolically demanding processes, such as the synaptic vesicle cycle that is fueled by mitochondrial energy generation, thus causing the production of damaging reactive oxygen species (ROS).[68] Synapses are also often located at relatively long distances from neuronal cell bodies, imposing logistics problems that include the need to transport degradative organelles along long axons.[69] Finally, individual

(E–F′) Representative images of Airyscan confocal single slice sections of synaptic boutons of *endoA*$^{-/-}$ larvae expressing *SH3GL2*$^{WT}$ (E and E′) and *SH3GL2*$^{G276V}$ (F and F′) (*nSyb-Gal4*) labeled with anti-ENDOA1 antibody. Scale bar: 5 μm.

(G) Quantification of the ENDOA1 integrated intensity across genotypes showing ratio of ENDOA1 intensity at the membrane to that within the cytosol. Error bars: mean ± SEM; statistical significance: two-way ANOVA with Tukey's multiple comparison test: ****$p < 0.0001$, ns, not significant, $n \geq 6$ larvae (24 NMJs) per genotype. Significance levels displayed above "Nefi" column refer to comparison with "Nefi" treatment (unstimulated) on control animals.

(H and I) Representative trajectories located within ENDOA1 nanodomains in NMJ boutons of *endoA*$^{-/-}$ larvae expressing *SH3GL2*$^{WT::mEos3.1}$ (H) and *SH3GL2*$^{G276V::mEos3.1}$ (I).

(J) This is quantified for each genotype as mean square displacement (MSD) as a function of time.

(K) Quantification of the area under the MSD curve ($\mu m^2 s$) represented in (J). Error bars mean ± SEM; statistical significance: unpaired t test with Welch's correction: ****$p < 0.0001$, $n \geq 4$ larvae ($n \geq 20$ nanodomains) per genotype.

Related to Figure S7.

Please cite this article in press as: Bademosi et al., EndophilinA-dependent coupling between activity-induced calcium influx and synaptic autophagy is disrupted by a Parkinson-risk mutation, Neuron (2023), https://doi.org/10.1016/j.neuron.2023.02.001



CellPress
OPEN ACCESS

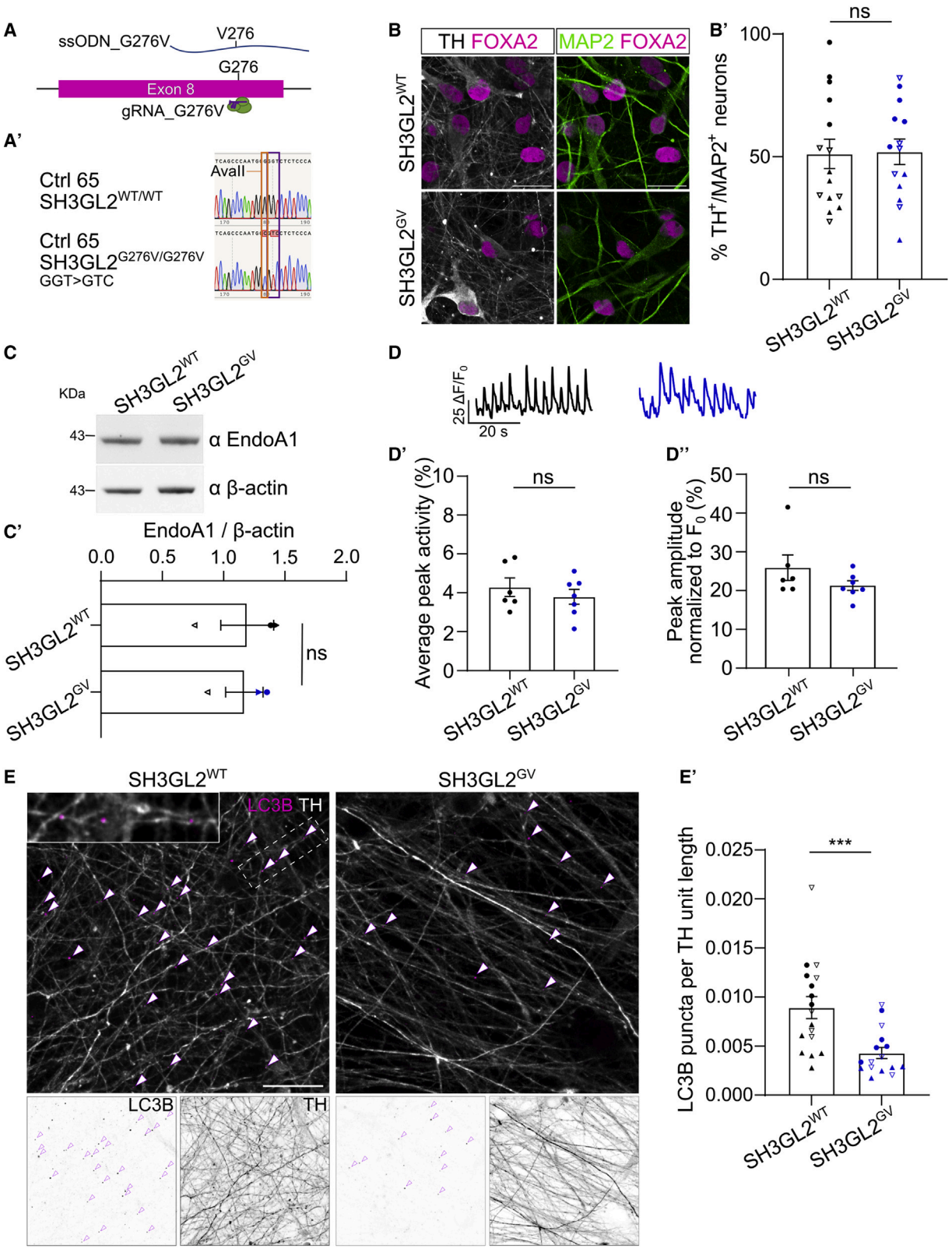


*(legend on next page)*

Please cite this article in press as: Bademosi et al., EndophilinA-dependent coupling between activity-induced calcium influx and synaptic autophagy is disrupted by a Parkinson-risk mutation, Neuron (2023), https://doi.org/10.1016/j.neuron.2023.02.001



synaptic boutons are fragile and uncontrolled autophagy could cause the (unwanted) engulfment of large parts of the cytoplasm, disrupting homeostasis. We propose that by coupling the activation of synaptic autophagy to neuronal activity, protein and organelle turnovers are induced at specific moments to maintain a healthy and functional synapse.

In this paper, we find that $Ca^{2+}$ influx at stimulated synapses induces autophagosome formation. Work in AIY neurons in *C. elegans* also shows a correlation between an increase in autophagosome formation and $Ca^{2+}$ waves,[30] suggesting this is a universal mechanism. The $Ca^{2+}$ that induces synaptic autophagy upon stimulation appears to be largely derived from extracellular sources, as the L/N-type $Ca^{2+}$ channel agonist Nefi and the availability of extracellular $Ca^{2+}$ promote the process.[35–37] However, contributions from intracellular sources, such as ER-$Ca^{2+}$, are not excluded or could further tune the process.[70]

Mechanistically, we provide evidence that EndoA is required to relay this $Ca^{2+}$ signal. We show the critical involvement of a negatively charged residue at position 264 (265 in flies). This residue was shown to regulate the association of EndoA with some of its binding partners in a $Ca^{2+}$-dependent manner (e.g., dynamin),[42–44] and we confirm this with fly and human protein. While we exclude large-scale conformational changes in EndoA that are directly induced by $Ca^{2+}$, we show that E264/D265 in the unstructured loop orchestrates EndoA flexibility and that mutating this residue eliminates the protein's response to $Ca^{2+}$ and its ability to drive synaptic autophagy. EndoA$^{D265A}$ mimics the absence of $Ca^{2+}$ and is more rigid, while EndoA$^{D265R}$ mimics the presence of $Ca^{2+}$ and is more flexible. There are likely other factors involved to relay the $Ca^{2+}$ signal during stimulation to EndoA, as the protein itself does not directly bind $Ca^{2+}$.[45] However, our work is consistent with a model where synaptic EndoA in the presence of $Ca^{2+}$ is more flexible and in the absence of $Ca^{2+}$ is more rigid, particularly in regions of the protein that mediate interactions with proteins and membranes. Flexible EndoA$^{D265R}$ moves away from membrane-bound nanodomains to support synaptic autophagy. Indeed, increases in mobility of proteins are frequently associated with the loss of interactions.[71] Recent work suggests that dynamin1 phase separates into condensates that likely also contain EndoA.[72] These observations could further explain our finding of EndoA stably localizing in nanodomains under resting conditions and the predicted $Ca^{2+}$ influx-induced flexibility changes in EndoA to induce a fraction of the protein to re-localize from these nanodomains to induce synaptic autophagy. In this model, a large enough pool of protein also still remains at the membrane to support basic endocytosis. The liberation of the EndoA pool for autophagy appears to be a neuron- and synapse-specific process because KCl stimulation of chromaffin cells causes an opposite redistribution of EndoA toward the plasma membrane, suggesting a different mechanism is at play in these cells.[73]

The early stages of neurodegeneration are associated with synaptic failure.[8,74–76] In PD, there is strong genetic evidence pointing to synaptic dysfunction, and several proteins mutated in PD are enriched at synapses (e.g., alpha-synuclein) and/or play essential roles in synaptic function (e.g., DNAJC6 and Synj1).[77–83] Similarly, ENDOA1 is emerging as a key protein in PD, and this is supported by human genetics: there are GWAS signals in the vicinity of the *SH3GL2* locus,[65] and there is a mutation associated with increased risk to PD in the open-reading frame that we modeled here.[24,63] We report that this PD-risk mutation in ENDOA1 does not strongly affect synaptic vesicle endocytosis, but it does block synaptic autophagy. However, an outstanding question remains how alterations in (synaptic) autophagy relate to the integrity of the synapse and to neuronal demise. Our work does show a correlation between defective (too much and too little) synaptic autophagy and neurodegeneration, also of dopaminergic neurons, but it did not find overt alterations in synaptic protein abundance in our EndoA mutants, possibly because subtle and local changes are below our detection limit (data not shown). Nonetheless, it remains to be shown what are the factors induced by defective autophagy that drive degeneration.

Excitingly, the role of EndoA in synaptic autophagy may be a central node in PD[8] that includes Synj1 (that binds EndoA), LRRK2 (that phosphorylates EndoA), and possibly Parkin (that

**Figure 8. Expression of SH3GL2$^{G276V}$ in differentiated dopaminergic neurons recapitulates findings from *Drosophila* synapses**

(A) Schematic representation of gene editing strategy to knock in the G276V mutation in *SH3GL2*.

(A′) Sanger sequencing showing successful homozygous editing.

(B) Representative maximum projection confocal images of terminally differentiated (60 days) SH3GL2$^{WT}$ ventral midbrain dopaminergic neurons (vmDAns) stained with the ventral midbrain marker FOXA2, dopaminergic marker TH, and neuronal marker MAP2. Scale bar: 100 μm.

(B′) Quantification of the number of dopaminergic neurons over the total number of neurons in the field of view expressed as percentage of TH$^+$/MAP2$^+$ neurons. Error bars: mean ± SEM. Statistical significance: one-way ANOVA with Tukey's multiple comparison test: ns, not significant. Single data points representing single confocal images. Data from three independent vmDAn differentiations (circles and empty/filled triangles represent independent differentiations).

(C and C′) Western blot with anti-ENDOA1 from induced vmDAn. (C′) Quantification of ENDOA1 intensity relative to β-actin expression. Experiments performed with three biological replicates (neurons from three independent differentiations, displayed as circle and full/empty triangles). Error bars: mean ± SEM. Statistical significance: Student's t test: ns not significant.

(D–D′′) Calcium imaging on induced vmDAns transfected with GCaMP6f. (D) Example traces of single SH3GL2$^{WT}$ (black) and SH3GL2$^{G276V}$ (blue) neurons. (D′) Quantification of the average activity of neurons in one field of view (peak activity) and (D′′) quantification of the average peak amplitude of the calcium responses. Error bars: mean ± SEM. Statistical significance: Student's t test: ns, not significant

(E) Representative maximum projection confocal images of induced vmDAn (60 days) SH3GL2$^{WT}$ vmDAn stained with anti-TH and anti-LC3B antibodies. Arrowheads: LC3B$^+$ autophagosomes within TH$^+$ neurites. Scale bar: 20 μm. Insert: zoom of the region indicated, where multiple LC3B$^+$ puncta are visible.

(E′) Quantification of the number of LC3B$^+$ autophagosomes within TH$^+$ neurites normalized to the total TH$^+$ neurite length in the field of view. Error bars: mean ± SEM. Statistical significance: Student's t test. ***$p < 0.001$. Single data points represent single confocal images. Data from three independent vmDAn differentiations (circles and empty/filled triangles represent independent differentiations).

Related to Figure S8.

Please cite this article in press as: Bademosi et al., EndophilinA-dependent coupling between activity-induced calcium influx and synaptic autophagy is disrupted by a Parkinson-risk mutation, Neuron (2023), https://doi.org/10.1016/j.neuron.2023.02.001



ubiquitinates EndoA).[32,82,84–86] Mutations in each of these proteins cause alterations in autophagic function,[14,15,87–89] and also analyses of post-mortem tissue of patients with PD found autophagy defects.[90–92] The exact function of the interactions between these PD-related proteins in pathology has not been elucidated, and our data start to show interesting interactions. It seems that different PD-relevant pathways can regulate EndoA availability for autophagy. While EndoA is required at the plasma membrane for endocytosis, LRRK2-dependent EndoA phosphorylation causes EndoA to localize to the synapse lumen to drive synaptic autophagy. Independently, we show here that $Ca^{2+}$ influx also regulates EndoA localization, and this process is directly blocked by the PD-risk mutant ENDOA1$^{G276V}$. In addition to these two mechanisms, EndoA also associates with Synj1 and Parkin that are also mutated in PD, but how these interactions (possibly) regulate synaptic autophagy remains to be tested.

## STAR★METHODS

Detailed methods are provided in the online version of this paper and include the following:


- KEY RESOURCES TABLE
- RESOURCE AVAILABILITY
  - Lead Contact
  - Materials Availability
  - Data and Code Availability
- EXPERIMENTAL MODEL AND SUBJECT DETAILS
  - Fly stocks and maintenance
  - iPSC maintenance and differentiation
- METHOD DETAILS
  - Plasmids generation
  - Autophagy induction assays
  - Confocal Live Imaging and quantification
  - Calcium imaging
  - Immunohistochemistry and confocal imaging
  - Zeiss Airyscan Confocal Imaging and quantification
  - Single-particle tracking photoactivated localization microscopy (sptPALM)
  - sptPALM Analysis
  - Single-Molecule Localization Microscopy and Cluster Analysis
  - Transmission Electron Microscopy (TEM)
  - Correlative Light Electron Microscopy (CLEM)
  - FM 1-43
  - Electrophysiology
  - Western blot
  - RNA extraction, retrotranscription and quantitative real time PCR (qRT-PCR)
  - Recombinant protein production and purification
  - Biophysical/structural characterization of recombinant proteins
  - Amide hydrogen/deuterium exchange mass spectrometry (HDX-MS)
  - SH-SY5Y cell maintenance and lysis
  - Co-immunoprecipitation
  - Electroretinograms (ERGs)
  - Light induced neurodegeneration and histology
  - Gene editing of iPSC
  - iPSC differentiation
  - Analysis of LC3B puncta in $TH^+$ neurites
- QUANTIFICATION AND STATISTICAL ANALYSIS


## SUPPLEMENTAL INFORMATION

Supplemental information can be found online at https://doi.org/10.1016/j.neuron.2023.02.001.

## ACKNOWLEDGMENTS

We thank the VIB-KU Leuven Center for Brain and Disease Research light microscopy unit for help. We thank the members of the Verstreken lab for discussions. Dr. Tristan Wallis (University of Queensland, Australia) provided edited DBSCAN codes for single molecule localization cluster analysis. Dr. Sam Duwe (University of Hasselt, Belgium) provided technical expertise. Equipment used in this study was acquired with funding from Hercules AKUL/11/37 and FWO G.0929.15 to Pieter Vanden Berghe (KU Leuven). Research support was provided by ERC, the Chan Zuckerberg Initiative, and a Methusalem grant of the Flemish government (to P.V.); FWO Vlaanderen (to P.V., W.V., F.R., J.S., E.M., C.C., and N.L.); Initiative d'Excellence de l'Université de Bordeaux (IDEX Neurocampus Chair, to S.-F.S.); GPRBRAIN_2030 and the Region Nouvelle-Aquitaine (18001716-18001717 to S.-F.S.); and VIB (to P.V., F.R., and J.S.). This research was also funded in part by Aligning Science Across Parkinson's (ASAP-000430) through the Michael J. Fox Foundation for Parkinson's Research (MJFF) and by an NHMRC Senior Research Fellowship (GNT1155794), Australian Research Council LIEF grant (LE130100078), and discovery project (DP190100674) to F.A.M. A.T.B. is supported by the EMBO long-term postdoctoral fellowship (ALTF-1034-2018) and Race Against Dementia—dementia Australia postdoctoral fellowship. P.V. is an alumnus of the FENS-Kavli Network of Excellence.

## AUTHOR CONTRIBUTIONS

Conceptualization, A.T.B., M.D., S.K., S.-F.S., and P.V.; methodology, A.T.B., M.D., S.K., and P.V.; investigation, A.T.B., M.D., S.K., C.C., J.S., S.F.G., N.S., N.L., E.M., S.K., K.V., and N.G.; formal analysis, A.T.B., M.D., S.K., J.S., J.-B.S., F.A.M., A.E., W.V., F.R., and J.S.; writing, A.T.B., M.D., S.K., and P.V.; funding acquisition, A.T.B., C.C., N.L., E.M., W.V., F.R., J.S., and P.V.; supervision, P.V.; all co-authors read and edited the manuscript. The co- first authors are listed in alphabetical order and they explicitly state the equal nature of their contribution and thus the interchangeability of the order they appear on this paper.

## DECLARATION OF INTERESTS

P.V. is the scientific founder of Jay Therapeutics. All other authors declare no competing interests.

## INCLUSION AND DIVERSITY

We support inclusive, diverse, and equitable conduct of research

Received: April 26, 2022
Revised: November 9, 2022
Accepted: January 31, 2023
Published: February 23, 2023

## REFERENCES

1. Mayford, M., Siegelbaum, S.A., and Kandel, E.R. (2012). Synapses and memory storage. Cold Spring Harb. Perspect. Biol. *4*, 1–18. https://doi.org/10.1101/cshperspect.a005751.
2. Wilhelm, B.G., Mandad, S., Truckenbrodt, S., Kröhnert, K., Schäfer, C., Rammner, B., Koo, S.J., Claßen, G.A., Krauss, M., Haucke, V., et al.

Please cite this article in press as: Bademosi et al., EndophilinA-dependent coupling between activity-induced calcium influx and synaptic autophagy is disrupted by a Parkinson-risk mutation, Neuron (2023), https://doi.org/10.1016/j.neuron.2023.02.001



(2014). Composition of isolated synaptic boutons reveals the amounts of vesicle trafficking proteins. Science *344*, 1023–1028. https://doi.org/10.1126/science.1252884.

3. Sudhof, T.C. (2004). The synaptic vesicle cycle. Annu. Rev. Neurosci. *27*, 509–547. https://doi.org/10.1146/annurev.neuro.26.041002.131412.
4. Südhof, T.C. (2013). Neurotransmitter release: the last millisecond in the life of a synaptic vesicle. Neuron *80*, 675–690. https://doi.org/10.1016/j.neuron.2013.10.022.
5. Südhof, T.C., and Malenka, R.C. (2008). Understanding synapses: past, present, and future. Neuron *60*, 469–476. https://doi.org/10.1016/j.neuron.2008.10.011.
6. Wang, Y.C., Lauwers, E., and Verstreken, P. (2017). Presynaptic protein homeostasis and neuronal function. Curr. Opin. Genet. Dev. *44*, 38–46. https://doi.org/10.1016/j.gde.2017.01.015.
7. Vijayan, V., and Verstreken, P. (2017). Autophagy in the presynaptic compartment in health and disease. J. Cell Biol. *216*, 1895–1906. https://doi.org/10.1083/jcb.201611113.
8. Soukup, S.F., Vanhauwaert, R., and Verstreken, P. (2018). Parkinson's disease: convergence on synaptic homeostasis. EMBO J. *37*. https://doi.org/10.15252/embj.201898960.
9. Azarnia Tehran, D., Kuijpers, M., and Haucke, V. (2018). Presynaptic endocytic factors in autophagy and neurodegeneration. Curr. Opin. Neurobiol. *48*, 153–159. https://doi.org/10.1016/j.conb.2017.12.018.
10. Decet, M., and Verstreken, P. (2021). Presynaptic autophagy and the connection with neurotransmission. Front. Cell Dev. Biol. *9*, 790721. https://doi.org/10.3389/fcell.2021.790721.
11. Baba, M., Osumi, M., Scott, S.V., Klionsky, D.J., and Ohsumi, Y. (1997). Two distinct pathways for targeting proteins from the cytoplasm to the vacuole/lysosome. J. Cell Biol. *139*, 1687–1695. https://doi.org/10.1083/jcb.139.7.1687.
12. Jin, M., and Klionsky, D.J. (2014). Regulation of autophagy: modulation of the size and number of autophagosomes. FEBS Lett. *588*, 2457–2463. https://doi.org/10.1016/j.febslet.2014.06.015.
13. Klionsky, D.J., Abdel-Aziz, A.K., Abdelfatah, S., Abdellatif, M., Abdoli, A., Abel, S., Abeliovich, H., Abildgaard, M.H., Abudu, Y.P., Acevedo-Arozena, A., et al. (2021). Guidelines for the use and interpretation of assays for monitoring autophagy (4th edition)[1]. Autophagy *17*, 1–382. Fourth Edition. https://doi.org/10.1080/15548627.2020.1797280.
14. Vanhauwaert, R., Kuenen, S., Masius, R., Bademosi, A., Manetsberger, J., Schoovaerts, N., Bounti, L., Gontcharenko, S., Swerts, J., Vilain, S., et al. (2017). The SAC 1 domain in synaptojanin is required for autophagosome maturation at presynaptic terminals. EMBO J. *36*, 1392–1411. https://doi.org/10.15252/embj.201695773.
15. Soukup, S.F., Kuenen, S., Vanhauwaert, R., Manetsberger, J., Hernández-Díaz, S., Swerts, J., Schoovaerts, N., Vilain, S., Gounko, N.V., Vints, K., et al. (2016). A LRRK2-dependent EndophilinA phosphoswitch is critical for macroautophagy at presynaptic terminals. Neuron *92*, 829–844. https://doi.org/10.1016/j.neuron.2016.09.037.
16. Montenegro-Venegas, C., Annamneedi, A., Hoffmann-Conaway, S., Gundelfinger, E.D., and Garner, C.C. (2020). BSN (bassoon) and PRKN/parkin in concert control presynaptic vesicle autophagy. Autophagy *16*, 1732–1733. https://doi.org/10.1080/15548627.2020.1801259.
17. Okerlund, N.D., Schneider, K., Leal-Ortiz, S., Montenegro-Venegas, C., Kim, S.A., Garner, L.C., Waites, C.L., Gundelfinger, E.D., Reimer, R.J., and Garner, C.C. (2017). Bassoon controls presynaptic autophagy through Atg5. Neuron *93*, 897–913.e7. https://doi.org/10.1016/j.neuron.2017.01.026.
18. Yang, S., Park, D., Manning, L., Hill, S.E., Cao, M., Xuan, Z., Gonzalez, I., Dong, Y., Clark, B., Shao, L., et al. (2022). Presynaptic autophagy is coupled to the synaptic vesicle cycle via ATG-9. Neuron *110*, 824–840.e10. https://doi.org/10.1016/j.neuron.2021.12.031.
19. Soukup, S.F., and Verstreken, P. (2017). EndoA/Endophilin-A creates docking stations for autophagic proteins at synapses. Autophagy *13*, 971–972. https://doi.org/10.1080/15548627.2017.1286440.
20. Murdoch, J.D., Rostosky, C.M., Gowrisankaran, S., Arora, A.S., Soukup, S.F., Vidal, R., Capece, V., Freytag, S., Fischer, A., Verstreken, P., et al. (2016). Endophilin-A deficiency induces the Foxo3a-Fbxo32 network in the brain and causes dysregulation of autophagy and the ubiquitin-proteasome system. Cell Rep. *17*, 1071–1086. https://doi.org/10.1016/j.celrep.2016.09.058.
21. Satake, W., Nakabayashi, Y., Mizuta, I., Hirota, Y., Ito, C., Kubo, M., Kawaguchi, T., Tsunoda, T., Watanabe, M., Takeda, A., et al. (2009). Genome-wide association study identifies common variants at four loci as genetic risk factors for Parkinson's disease. Nat. Genet. *41*, 1303–1307. https://doi.org/10.1038/ng.485.
22. Simón-Sánchez, J., Schulte, C., Bras, J.M., Sharma, M., Gibbs, J.R., Berg, D., Paisan-Ruiz, C., Lichtner, P., Scholz, S.W., Hernandez, D.G., et al. (2009). Genome-wide association study reveals genetic risk underlying Parkinson's disease. Nat. Genet. *41*, 1308–1312. https://doi.org/10.1038/ng.487.
23. Daida, K., Funayama, M., Li, Y., Yoshino, H., Hayashida, A., Ikeda, A., Ogaki, K., Nishioka, K., and Hattori, N. (2020). Identification of disease-associated variants by targeted gene panel resequencing in Parkinson's disease. Front. Neurol. *11*, 576465. https://doi.org/10.3389/fneur.2020.576465.
24. Germer, E.L., Imhoff, S., Vilariño-Güell, C., Kasten, M., Seibler, P., Brüggemann, N., International Parkinson's Disease Genomics Consortium, Klein, C., and Trinh, J. (2019). The role of rare coding variants in Parkinson's disease GWAS loci. Front. Neurol. *10*, 1284. https://doi.org/10.3389/fneur.2019.01284.
25. Kroemer, G., Mariño, G., and Levine, B. (2010). Autophagy and the integrated stress response. Mol. Cell *40*, 280–293. https://doi.org/10.1016/j.molcel.2010.09.023.
26. Nakatogawa, H. (2020). Mechanisms governing autophagosome biogenesis. Nat. Rev. Mol. Cell Biol. *21*, 439–458. https://doi.org/10.1038/s41580-020-0241-0.
27. Nixon, R.A. (2013). The role of autophagy in neurodegenerative disease. Nat. Med. *19*, 983–997. https://doi.org/10.1038/nm.3232.
28. Shehata, M., Matsumura, H., Okubo-Suzuki, R., Ohkawa, N., and Inokuchi, K. (2012). Neuronal stimulation induces autophagy in hippocampal neurons that is involved in AMPA receptor degradation after chemical long-term depression. J. Neurosci. *32*, 10413–10422. https://doi.org/10.1523/JNEUROSCI.4533-11.2012.
29. Wang, T., Martin, S., Papadopulos, A., Harper, C.B., Mavlyutov, T.A., Niranjan, D., Glass, N.R., Cooper-White, J.J., Sibarita, J.B., Choquet, D., et al. (2015). Control of autophagosome axonal retrograde flux by presynaptic activity unveiled using botulinum neurotoxin type A. J. Neurosci. *35*, 6179–6194. https://doi.org/10.1523/JNEUROSCI.3757-14.2015.
30. Hill, S.E., Kauffman, K.J., Krout, M., Richmond, J.E., Melia, T.J., and Colón-Ramos, D.A. (2019). Maturation and clearance of autophagosomes in neurons depends on a specific cysteine protease isoform, ATG-4.2. Dev. Cell *49*, 251–266.e8. https://doi.org/10.1016/j.devcel.2019.02.013.
31. Kulkarni, V.V., Anand, A., Herr, J.B., Miranda, C., Vogel, M.C., and Maday, S. (2021). Synaptic activity controls autophagic vacuole motility and function in dendrites. J. Cell Biol. *220*. https://doi.org/10.1083/jcb.202002084.
32. Matta, S., Van Kolen, K., da Cunha, R., van den Bogaart, G., Mandemakers, W., Miskiewicz, K., De Bock, P.J., Morais, V.A., Vilain, S., Haddad, D., et al. (2012). LRRK2 controls an EndoA phosphorylation cycle in synaptic endocytosis. Neuron *75*, 1008–1021. https://doi.org/10.1016/j.neuron.2012.08.022.
33. Chouhan, A.K., Zhang, J., Zinsmaier, K.E., and Macleod, G.T. (2010). Presynaptic mitochondria in functionally different motor neurons exhibit similar affinities for $Ca^{2+}$ but exert little influence as $Ca^{2+}$ buffers at nerve

Please cite this article in press as: Bademosi et al., EndophilinA-dependent coupling between activity-induced calcium influx and synaptic autophagy is disrupted by a Parkinson-risk mutation, Neuron (2023), https://doi.org/10.1016/j.neuron.2023.02.001



firing rates in situ. J. Neurosci. *30*, 1869–1881. https://doi.org/10.1523/JNEUROSCI.4701-09.2010.

34. Chouhan, A.K., Ivannikov, M.V., Lu, Z., Sugimori, M., Llinas, R.R., and Macleod, G.T. (2012). Cytosolic calcium coordinates mitochondrial energy metabolism with presynaptic activity. J. Neurosci. *32*, 1233–1243. https://doi.org/10.1523/JNEUROSCI.1301-11.2012.

35. Yoshii, M., Watabe, S., Murashima, Y.L., Nukada, T., and Shiotani, T. (2000). Cellular mechanism of action of cognitive enhancers: effects of nefiracetam on neuronal $Ca^{2+}$ channels. Alzheimer Dis. Assoc. Disord. *14*. S95–102. https://doi.org/10.1097/00002093-200000001-00014.

36. Yoshii, M., and Watabe, S. (1994). Enhancement of neuronal calcium channel currents by the nootropic agent, nefiracetam (DM-9384), in NG108-15 cells. Brain Res. *642*, 123–131. https://doi.org/10.1016/0006-8993(94)90913-X.

37. Nishizaki, T., Matsuoka, T., Nomura, T., Sumikawa, K., Shiotani, T., Watabe, S., and Yoshii, M. (1998). Nefiracetam modulates acetylcholine receptor currents via two different signal transduction pathways. Mol. Pharmacol. *53*, 1–5. https://doi.org/10.1124/mol.53.1.1.

38. Verstreken, P., Kjaerulff, O., Lloyd, T.E., Atkinson, R., Zhou, Y., Meinertzhagen, I.A., and Bellen, H.J. (2002). Endophilin mutations block clathrin-mediated endocytosis but not neurotransmitter release. Cell *109*, 101–112. https://doi.org/10.1016/S0092-8674(02)00688-8.

39. Ringstad, N., Gad, H., Löw, P., Di Paolo, G., Brodin, L., Shupliakov, O., and De Camilli, P. (1999). Endophilin/sh3p4 is required for the transition from early to late stages in clathrin-mediated synaptic vesicle endocytosis. Neuron *24*, 143–154. https://doi.org/10.1016/S0896-6273(00)80828-4.

40. Schuske, K.R., Richmond, J.E., Matthies, D.S., Davis, W.S., Runz, S., Rube, D.A., Van Der Bliek, A.M., and Jorgensen, E.M. (2003). Endophilin is required for synaptic vesicle endocytosis by localizing synaptojanin. Neuron *40*, 749–762. https://doi.org/10.1016/S0896-6273(03)00667-6.

41. Milosevic, I., Giovedi, S., Lou, X., Raimondi, A., Collesi, C., Shen, H., Paradise, S., O'Toole, E., Ferguson, S., Cremona, O., and De Camilli, P. (2011). Recruitment of endophilin to clathrin-coated pit necks is required for efficient vesicle uncoating after fission. Neuron *72*, 587–601. https://doi.org/10.1016/j.neuron.2011.08.029.

42. Zhang, J., Fan, J., Tian, Q., Song, Z., Zhang, J.F., and Chen, Y. (2012). Characterization of two distinct modes of endophilin in clathrin-mediated endocytosis. Cell. Signal. *24*, 2043–2050. https://doi.org/10.1016/j.cellsig.2012.06.006.

43. Chen, Y., Deng, L., Maeno-Hikichi, Y., Lai, M., Chang, S., Chen, G., and Zhang, J.F. (2003). Formation of an endophilin-$Ca^{2+}$ channel complex is critical for clathrin-mediated synaptic vesicle endocytosis. Cell *115*, 37–48. https://doi.org/10.1016/S0092-8674(03)00726-8.

44. Kroll, J., Jaime Tobón, L.M., Vogl, C., Neef, J., Kondratiuk, I., König, M., Strenzke, N., Wichmann, C., Milosevic, I., and Moser, T. (2019). Endophilin-A regulates presynaptic $Ca^{2+}$ influx and synaptic vesicle recycling in auditory hair cells. EMBO J. *38*. https://doi.org/10.15252/embj.2018100116.

45. Yang, Y., Chen, J., Chen, X., Li, D., He, J., Wang, S., Zhao, S., Yang, X., Deng, S., Tong, C., et al. (2021). Endophilin a1 drives acute structural plasticity of dendritic spines in response to $Ca^{2+}$/calmodulin. J. Cell Biol. *220*, e202007172. https://doi.org/10.1083/jcb.202007172.

46. Masson, G.R., Burke, J.E., Ahn, N.G., Anand, G.S., Borchers, C., Brier, S., Bou-Assaf, G.M., Engen, J.R., Englander, S.W., Faber, J., et al. (2019). Recommendations for performing, interpreting and reporting hydrogen deuterium exchange mass spectrometry (HDX-MS) experiments. Nat. Methods *16*, 595–602. https://doi.org/10.1038/s41592-019-0459-y.

47. Smit, J.H., Krishnamurthy, S., Srinivasu, B.Y., Parakra, R., Karamanou, S., and Economou, A. (2021). Probing universal protein dynamics using hydrogen–deuterium exchange mass spectrometry-derived residue-level Gibbs free energy. Anal. Chem. *93*, 12840–12847. https://doi.org/10.1021/acs.analchem.1c02155.

48. Jumper, J., Evans, R., Pritzel, A., Green, T., Figurnov, M., Ronneberger, O., Tunyasuvunakool, K., Bates, R., Žídek, A., Potapenko, A., et al. (2021). Highly accurate protein structure prediction with AlphaFold. Nature *596*, 583–589. https://doi.org/10.1038/s41586-021-03819-2.

49. Guichet, A., Wucherpfennig, T., Dudu, V., Etter, S., Wilsch-Bräuniger, M., Hellwig, A., González-Gaitán, M., Huttner, W.B., and Schmidt, A.A. (2002). Essential role of endophilin A in synaptic vesicle budding at the Drosophila neuromuscular junction. EMBO J. *21*, 1661–1672. https://doi.org/10.1093/emboj/21.7.1661.

50. Dickman, D.K., Horne, J.A., Meinertzhagen, I.A., and Schwarz, T.L. (2005). A slowed classical pathway rather than kiss-and-run mediates endocytosis at synapses lacking synaptojanin and endophilin. Cell *123*, 521–533. https://doi.org/10.1016/j.cell.2005.09.026.

51. Ramaswami, M., Krishnan, K.S., and Kelly, R.B. (1994). Intermediates in synaptic vesicle recycling revealed by optical imaging of Drosophila neuromuscular junctions. Neuron *13*, 363–375. https://doi.org/10.1016/0896-6273(94)90353-0.

52. Verstreken, P., Koh, T.W., Schulze, K.L., Zhai, R.G., Hiesinger, P.R., Zhou, Y., Mehta, S.Q., Cao, Y., Roos, J., and Bellen, H.J. (2003). Synaptojanin is recruited by endophilin to promote synaptic vesicle uncoating. Neuron *40*, 733–748. https://doi.org/10.1016/S0896-6273(03)00644-5.

53. Huff, J. (2015). The Airyscan detector from ZEISS: confocal imaging with improved signal-to-noise ratio and super-resolution. Nat. Methods *12*. i–ii. https://doi.org/10.1038/nmeth.f.388.

54. Bademosi, A.T., Lauwers, E., Amor, R., Verstreken, P., Van Swinderen, B., and Meunier, F.A. (2018). In vivo single-molecule tracking at the drosophila presynaptic motor nerve terminal. J. Vis. Exp. *131*. https://doi.org/10.3791/56952.

55. Bademosi, A.T., Lauwers, E., Padmanabhan, P., Odierna, L., Chai, Y.J., Papadopulos, A., Goodhill, G.J., Verstreken, P., Van Swinderen, B., and Meunier, F.A. (2017). In vivo single-molecule imaging of syntaxin1A reveals polyphosphoinositide- and activity-dependent trapping in presynaptic nanoclusters. Nat. Commun. *8*, 13660. https://doi.org/10.1038/ncomms13660.

56. Tokunaga, M., Imamoto, N., and Sakata-Sogawa, K. (2008). Highly inclined thin illumination enables clear single-molecule imaging in cells. Nat. Methods *5*, 159–161. https://doi.org/10.1038/nmeth1171.

57. Zhang, M., Chang, H., Zhang, Y., Yu, J., Wu, L., Ji, W., Chen, J., Liu, B., Lu, J., Liu, Y., et al. (2012). Rational design of true monomeric and bright photoactivatable fluorescent proteins. Nat. Methods *9*, 727–729. https://doi.org/10.1038/nmeth.2021.

58. Manley, S., Gillette, J.M., Patterson, G.H., Shroff, H., Hess, H.F., Betzig, E., and Lippincott-Schwartz, J. (2008). High-density mapping of single-molecule trajectories with photoactivated localization microscopy. Nat. Methods *5*, 155–157. https://doi.org/10.1038/nmeth.1176.

59. Fleming, A., Bourdenx, M., Fujimaki, M., Karabiyik, C., Krause, G.J., Lopez, A., Martín-Segura, A., Puri, C., Scrivo, A., Skidmore, J., et al. (2022). The different autophagy degradation pathways and neurodegeneration. Neuron *110*, 935–966. https://doi.org/10.1016/j.neuron.2022.01.017.

60. Komatsu, M., Waguri, S., Chiba, T., Murata, S., Iwata, J., Tanida, I., Ueno, T., Koike, M., Uchiyama, Y., Kominami, E., and Tanaka, K. (2006). Loss of autophagy in the central nervous system causes neurodegeneration in mice. Nature *441*, 880–884. https://doi.org/10.1038/nature04723.

61. Chouhan, A.K., Guo, C., Hsieh, Y.C., Ye, H., Senturk, M., Zuo, Z., Li, Y., Chatterjee, S., Botas, J., Jackson, G.R., et al. (2016). Uncoupling neuronal death and dysfunction in Drosophila models of neurodegenerative disease. Acta Neuropathol. Commun. *4*, 62. https://doi.org/10.1186/s40478-016-0333-4.

62. Wang, T., and Montell, C. (2007). Phototransduction and retinal degeneration in Drosophila. Pflugers Arch. *454*, 821–847. https://doi.org/10.1007/s00424-007-0251-1.

63. Chang, D., Nalls, M.A., Hallgrímsdóttir, I.B., Hunkapiller, J., van der Brug, M., Cai, F., International Parkinson's Disease Genomics Consortium, 23andMe Research Team, Kerchner, G.A., Ayalon, G., et al. (2017). A meta-analysis of genome-wide association studies identifies 17 new Parkinson's disease risk loci. Nat. Genet. *49*, 1511–1516. https://doi.org/10.1038/ng.3955.

64. Alfradique-Dunham, I., Al-Ouran, R., von Coelln, R., Blauwendraat, C., Hill, E., Luo, L., Stillwell, A., Young, E., Kaw, A., Tan, M., et al. (2021). Genome-wide association study meta-analysis for Parkinson disease motor subtypes. Neurol. Genet. *7*, e557. https://doi.org/10.1212/NXG.0000000000000557.

65. Nalls, M.A., Blauwendraat, C., Vallerga, C.L., Heilbron, K., Bandres-Ciga, S., Chang, D., Tan, M., Kia, D.A., Noyce, A.J., Xue, A., et al. (2019). Identification of novel risk loci, causal insights, and heritable risk for Parkinson's disease: a meta-analysis of genome-wide association studies. Lancet Neurol. *18*, 1091–1102. https://doi.org/10.1016/S1474-4422(19)30320-5.

66. Baumann, H., Ott, F., Weber, J., Trilck-Winkler, M., Münchau, A., Zittel, S., Kostić, V.S., Kaiser, F.J., Klein, C., Busch, H., et al. (2021). Linking penetrance and transcription in DYT-THAP1: insights from a human iPSC-derived cortical model. Mov. Disord. *36*, 1381–1391. https://doi.org/10.1002/mds.28506.

67. Martinet, W., Schrijvers, D.M., Timmermans, J.P., Bult, H., and De Meyer, G.R.Y. (2013). Immunohistochemical analysis of macroautophagy: recommendations and limitations. Autophagy *9*, 386–402. https://doi.org/10.4161/auto.22968.

68. Verstreken, P., Ly, C.V., Venken, K.J.T., Koh, T.W., Zhou, Y., and Bellen, H.J. (2005). Synaptic mitochondria are critical for mobilization of reserve pool vesicles at Drosophila neuromuscular junctions. Neuron *47*, 365–378. https://doi.org/10.1016/j.neuron.2005.06.018.

69. Wang, T., Li, W., Martin, S., Papadopulos, A., Joensuu, M., Liu, C., Jiang, A., Shamsollahi, G., Amor, R., Lanoue, V., et al. (2020). Radial contractility of actomyosin rings facilitates axonal trafficking and structural stability. J. Cell Biol. *219*. https://doi.org/10.1083/jcb.201902001.

70. Kuijpers, M., Kochlamazashvili, G., Stumpf, A., Puchkov, D., Swaminathan, A., Lucht, M.T., Krause, E., Maritzen, T., Schmitz, D., and Haucke, V. (2021). Neuronal autophagy regulates presynaptic neurotransmission by controlling the axonal endoplasmic reticulum. Neuron *109*, 299–313.e9. https://doi.org/10.1016/j.neuron.2020.10.005.

71. Ribrault, C., Reingruber, J., Petković, M., Galli, T., Ziv, N.E., Holcman, D., and Triller, A. (2011). Syntaxin1A lateral diffusion reveals transient and local SNARE interactions. J. Neurosci. *31*, 17590–17602. https://doi.org/10.1523/JNEUROSCI.4065-11.2011.

72. Imoto, Y., Raychaudhuri, S., Ma, Y., Fenske, P., Sandoval, E., Itoh, K., Blumrich, E.M., Matsubayashi, H.T., Mamer, L., Zarebidaki, F., et al. (2022). Dynamin is primed at endocytic sites for ultrafast endocytosis. Neuron *110*, 2815–2835.e13. https://doi.org/10.1016/j.neuron.2022.06.010.

73. Gowrisankaran, S., Houy, S., del Castillo, J.G.P., Steubler, V., Gelker, M., Kroll, J., Pinheiro, P.S., Schwitters, D., Halbsgut, N., Pechstein, A., et al. (2020). Endophilin-A coordinates priming and fusion of neurosecretory vesicles via intersectin. Nat. Commun. *11*, 1266. https://doi.org/10.1038/s41467-020-14993-8.

74. Caminiti, S.P., Presotto, L., Baroncini, D., Garibotto, V., Moresco, R.M., Gianolli, L., Volonté, M.A., Antonini, A., and Perani, D. (2017). Axonal damage and loss of connectivity in nigrostriatal and mesolimbic dopamine pathways in early Parkinson's disease. Neuroimage Clin. *14*, 734–740. https://doi.org/10.1016/j.nicl.2017.03.011.

75. Burke, R.E., and O'Malley, K. (2013). Axon degeneration in Parkinson's disease. Exp. Neurol. *246*, 72–83. https://doi.org/10.1016/j.expneurol.2012.01.011.

76. Delva, A., Van Weehaeghe, D., Koole, M., Van Laere, K., and Vandenberghe, W. (2020). Loss of presynaptic terminal integrity in the substantia nigra in early Parkinson's disease. Mov. Disord. *35*, 1977–1986. https://doi.org/10.1002/mds.28216.

77. Proukakis, C., Dudzik, C.G., Brier, T., MacKay, D.S., Cooper, J.M., Millhauser, G.L., Houlden, H., and Schapira, A.H. (2013). A novel α-synuclein missense mutation in Parkinson disease. Neurology *80*, 1062–1064. https://doi.org/10.1212/WNL.0b013e31828727ba.

78. Krüger, R., Kuhn, W., Müller, T., Woitalla, D., Graeber, M., Kösel, S., Przuntek, H., Epplen, J.T., Schöls, L., and Riess, O. (1998). Ala30Pro mutation in the gene encoding α-synuclein in Parkinson's disease. Nat. Genet. *18*, 106–108. https://doi.org/10.1038/ng0298-106.

79. Polymeropoulos, M.H., Lavedan, C., Leroy, E., Ide, S.E., Dehejia, A., Dutra, A., Pike, B., Root, H., Rubenstein, J., Boyer, R., et al. (1997). Mutation in the alpha-synuclein gene identified in families with Parkinson's disease. Science *276*, 2045–2047. https://doi.org/10.1126/science.276.5321.2045.

80. Zarranz, J.J., Alegre, J., Gómez-Esteban, J.C., Lezcano, E., Ros, R., Ampuero, I., Vidal, L., Hoenicka, J., Rodriguez, O., Atarés, B., et al. (2004). The new mutation, E46K, of alpha-synuclein causes Parkinson and Lewy body dementia. Ann. Neurol. *55*, 164–173. https://doi.org/10.1002/ana.10795.

81. Olgiati, S., Quadri, M., Fang, M., Rood, J.P.M.A., Saute, J.A., Chien, H.F., Bouwkamp, C.G., Graafland, J., Minneboo, M., Breedveld, G.J., et al. (2016). DNAJC6 mutations associated with early-onset Parkinson's disease. Ann. Neurol. *79*, 244–256. https://doi.org/10.1002/ana.24553.

82. Krebs, C.E., Karkheiran, S., Powell, J.C., Cao, M., Makarov, V., Darvish, H., Di Paolo, G., Walker, R.H., Shahidi, G.A., Buxbaum, J.D., et al. (2013). The sac1 domain of SYNJ1 identified mutated in a family with early-onset progressive parkinsonism with generalized seizures. Hum. Mutat. *34*, 1200–1207. https://doi.org/10.1002/humu.22372.

83. Quadri, M., Fang, M., Picillo, M., Olgiati, S., Breedveld, G.J., Graafland, J., Wu, B., Xu, F., Erro, R., Amboni, M., et al. (2013). Mutation in the SYNJ1 gene associated with autosomal recessive, early-onset parkinsonism. Hum. Mutat. *34*, 1208–1215. https://doi.org/10.1002/humu.22373.

84. Paisán-Ruiz, C. (2009). LRRK2 gene variation and its contribution to Parkinson disease. Hum. Mutat. *30*, 1153–1160. https://doi.org/10.1002/humu.21038.

85. Olgiati, S., De Rosa, A., Quadri, M., Criscuolo, C., Breedveld, G.J., Picillo, M., Pappatà, S., Quarantelli, M., Barone, P., De Michele, G., and Bonifati, V. (2014). PARK20 caused by SYNJ1 homozygous Arg258Gln mutation in a new Italian family. Neurogenetics *15*, 183–188. https://doi.org/10.1007/s10048-014-0406-0.

86. Kitada, T., Asakawa, S., Hattori, N., Matsumine, H., Yamamura, Y., Minoshima, S., Yokochi, M., Mizuno, Y., and Shimizu, N. (1998). Mutations in the parkin gene cause autosomal recessive juvenile parkinsonism. Nature *392*, 605–608. https://doi.org/10.1038/33416.

87. Oliveira, L.M.A., Falomir-Lockhart, L.J., Botelho, M.G., Lin, K.H., Wales, P., Koch, J.C., Gerhardt, E., Taschenberger, H., Outeiro, T.F., Lingor, P., et al. (2015). Elevated α-synuclein caused by SNCA gene triplication impairs neuronal differentiation and maturation in Parkinson's patient-derived induced pluripotent stem cells. Cell Death Dis. *6*, e1994. https://doi.org/10.1038/cddis.2015.318.

88. Yue, M., Hinkle, K.M., Davies, P., Trushina, E., Fiesel, F.C., Christenson, T.A., Schroeder, A.S., Zhang, L., Bowles, E., Behrouz, B., et al. (2015). Progressive dopaminergic alterations and mitochondrial abnormalities in LRRK2 G2019S knock-in mice. Neurobiol. Dis. *78*, 172–195. https://doi.org/10.1016/j.nbd.2015.02.031.

89. Schöndorf, D.C., Aureli, M., McAllister, F.E., Hindley, C.J., Mayer, F., Schmid, B., Sardi, S.P., Valsecchi, M., Hoffmann, S., Schwarz, L.K., et al. (2014). IPSC-derived neurons from GBA1-associated Parkinson's disease patients show autophagic defects and impaired calcium homeostasis. Nat. Commun. *5*, 4028. https://doi.org/10.1038/ncomms5028.

Please cite this article in press as: Bademosi et al., EndophilinA-dependent coupling between activity-induced calcium influx and synaptic autophagy is disrupted by a Parkinson-risk mutation, Neuron (2023), https://doi.org/10.1016/j.neuron.2023.02.001



90. Murphy, K.E., Gysbers, A.M., Abbott, S.K., Spiro, A.S., Furuta, A., Cooper, A., Garner, B., Kabuta, T., and Halliday, G.M. (2015). Lysosomal-associated membrane protein 2 isoforms are differentially affected in early Parkinson's disease. Mov. Disord. *30*, 1639–1647. https://doi.org/10.1002/mds.26141.

91. Tanji, K., Mori, F., Kakita, A., Takahashi, H., and Wakabayashi, K. (2011). Alteration of autophagosomal proteins (LC3, GABARAP and GATE-16) in Lewy body disease. Neurobiol. Dis. *43*, 690–697. https://doi.org/10.1016/j.nbd.2011.05.022.

92. Alvarez-Erviti, L., Rodriguez-Oroz, M.C., Cooper, J.M., Caballero, C., Ferrer, I., Obeso, J.A., and Schapira, A.H.V. (2010). Chaperone-mediated autophagy markers in Parkinson disease brains. Arch. Neurol. *67*, 1464–1472. https://doi.org/10.1001/archneurol.2010.198.

93. Hegedűs, K., Takáts, S., Boda, A., Jipa, A., Nagy, P., Varga, K., Kovács, A.L., and Juhász, G. (2016). The Ccz1-Mon1-Rab7 module and Rab5 control distinct steps of autophagy. Mol. Biol. Cell *27*, 3132–3142. https://doi.org/10.1091/mbc.E16-03-0205.

94. Flemr, M., and Bühler, M. (2015). Single-step generation of conditional knockout mouse embryonic stem cells. Cell Rep. *12*, 709–716. https://doi.org/10.1016/j.celrep.2015.06.051.

95. Ran, F.A., Hsu, P.D., Wright, J., Agarwala, V., Scott, D.A., and Zhang, F. (2013). Genome engineering using the CRISPR-Cas9 system. Nat. Protoc. *8*, 2281–2308. https://doi.org/10.1038/nprot.2013.143.

96. Levitan, E.S., Lanni, F., and Shakiryanova, D. (2007). In vivo imaging of vesicle motion and release at the Drosophila neuromuscular junction. Nat. Protoc. *2*, 1117–1125. https://doi.org/10.1038/nprot.2007.142.

97. Kasprowicz, J., Kuenen, S., Swerts, J., Miskiewicz, K., and Verstreken, P. (2014). Dynamin photoinactivation blocks clathrin and α-adaptin recruitment and induces bulk membrane retrieval. J. Cell Biol. *204*, 1141–1156. https://doi.org/10.1083/jcb.201310090.

98. Kechkar, A., Nair, D., Heilemann, M., Choquet, D., and Sibarita, J.B. (2013). Real-time analysis and visualization for single-molecule based super-resolution microscopy. PLOS One *8*, e62918. https://doi.org/10.1371/journal.pone.0062918.

99. Nair, D., Hosy, E., Petersen, J.D., Constals, A., Giannone, G., Choquet, D., and Sibarita, J.B. (2013). Super-resolution imaging reveals that AMPA receptors inside synapses are dynamically organized in nanodomains regulated by PSD95. J. Neurosci. *33*, 13204–13224. https://doi.org/10.1523/JNEUROSCI.2381-12.2013.

100. Constals, A., Penn, A.C., Compans, B., Toulmé, E., Phillipat, A., Marais, S., Retailleau, N., Hafner, A.S., Coussen, F., Hosy, E., and Choquet, D. (2015). Glutamate-induced AMPA receptor desensitization increases their mobility and modulates short-term plasticity through unbinding from stargazin. Neuron *85*, 787–803. https://doi.org/10.1016/j.neuron.2015.01.012.

101. Ester, M., Kriegel, H.-P., Sander, J., and Xu, X. (1996). A density-based algorithm for discovering clusters in large spatial databases with noise. Data Min. Knowl. Discov. *96*, 226–231.

102. Lauwers, E., Wang, Y.-C., Gallardo, R., Van der Kant, R., Michiels, E., Swerts, J., Baatsen, P., Zaiter, S.S., McAlpine, S.R., Gounko, N.V., et al. (2018). Hsp90 Mediates Membrane Deformation and Exosome Release. Mol. Cell *71*, 689–702.e9. https://doi.org/10.1016/j.molcel.2018.07.016.

103. Verstreken, P., Ohyama, T., and Bellen, H.J. (2008). FM 1-43 labeling of synaptic vesicle pools at the drosophila neuromuscular junction. Methods Mol. Biol. *440*, 349–369. https://doi.org/10.1007/978-1-59745-178-9_26.

104. Slabbaert, J.R., Kuenen, S., Swerts, J., Maes, I., Uytterhoeven, V., Kasprowicz, J., Fernandes, A.C., Blust, R., and Verstreken, P. (2016). Shawn, the Drosophila homolog of SLC25A39/40, is a mitochondrial carrier that promotes neuronal survival. J. Neurosci. *36*, 1914–1929. https://doi.org/10.1523/JNEUROSCI.3432-15.2016.

105. Hu, Y., Sopko, R., Foos, M., Kelley, C., Flockhart, I., Ammeux, N., Wang, X., Perkins, L., Perrimon, N., and Mohr, S.E. (2013). FlyPrimerBank: an online database for Drosophila melanogaster gene expression analysis and knockdown evaluation of RNAi reagents. G3 (Bethesda) *3*, 1607–1616. https://doi.org/10.1534/g3.113.007021.

106. Capdeville, C., Russo, L., Penton, D., Migliavacca, J., Zecevic, M., Gries, A., Neuhauss, S.C., Grotzer, M.A., and Baumgartner, M. (2022). Spatial proteomics finds CD155 and endophilin-A1 as mediators of growth and invasion in medulloblastoma. Life Sci. Alliance *5*, 5. https://doi.org/10.26508/lsa.202201380.

107. Pernot, P., Round, A., Barrett, R., De Maria Antolinos, A., Gobbo, A., Gordon, E., Huet, J., Kieffer, J., Lentini, M., Mattenet, M., et al. (2013). Upgraded ESRF BM29 beamline for SAXS on macromolecules in solution. J. Synchrotron Radiat. *20*, 660–664. https://doi.org/10.1107/S0909049513010431.

108. Thureau, A., Roblin, P., and Pérez, J. (2021). BioSAXS on the SWING beamline at Synchrotron SOLEIL. J. Appl. Crystallogr. *54*, 1698–1710. https://doi.org/10.1107/S1600576721008736.

109. Perez, J., Bizien, T., T.A., and G.A.F. (2022). https://www.synchrotron-soleil.fr/en/beamlines/swing.

110. Panjkovich, A., and Svergun, D.I. (2018). CHROMIXS: automatic and interactive analysis of chromatography-coupled small-angle X-ray scattering data. Bioinformatics *34*, 1944–1946. https://doi.org/10.1093/bioinformatics/btx846.

111. Petoukhov, M.V., Franke, D., Shkumatov, A.V., Tria, G., Kikhney, A.G., Gajda, M., Gorba, C., Mertens, H.D.T., Konarev, P.V., and Svergun, D.I. (2012). New developments in the ATSAS program package for small-angle scattering data analysis. J. Appl. Crystallogr. *45*, 342–350. https://doi.org/10.1107/S0021889812007662.

112. Hajizadeh, N.R., Franke, D., Jeffries, C.M., and Svergun, D.I. (2018). Consensus Bayesian assessment of protein molecular mass from solution X-ray scattering data. Sci. Rep. *8*, 7204. https://doi.org/10.1038/s41598-018-25355-2.

113. Konarev, P.V., Volkov, V.V., Sokolova, A.V., Koch, M.H.J., and Svergun, D.I. (2003). Primus: A Windows PC-based system for small-angle scattering data analysis. J. Appl. Crystallogr. *36*, 1277–1282. https://doi.org/10.1107/S0021889803012779.

114. Krishnamurthy, S., Eleftheriadis, N., Karathanou, K., Smit, J.H., Portaliou, A.G., Chatzi, K.E., Karamanou, S., Bondar, A.N., Gouridis, G., and Economou, A. (2021). A nexus of intrinsic dynamics underlies translocase priming. Structure *29*, 846–858.e7. https://doi.org/10.1016/j.str.2021.03.015.

115. Krishnamurthy, S., Sardis, M.F., Eleftheriadis, N., Chatzi, K.E., Smit, J.H., Karathanou, K., Gouridis, G., Portaliou, A.G., Bondar, A.N., Karamanou, S., and Economou, A. (2022). Preproteins couple the intrinsic dynamics of SecA to its ATPase cycle to translocate via a catch and release mechanism. Cell Rep. *38*, 110346. https://doi.org/10.1016/j.celrep.2022.110346.

116. Smets, D., Tsirigotaki, A., Smit, J.H., Krishnamurthy, S., Portaliou, A.G., Vorobieva, A., Vranken, W., Karamanou, S., and Economou, A. (2022). Evolutionary adaptation of the protein folding pathway for secretability. EMBO J. *41*, e111344. https://doi.org/10.15252/embj.2022111344.

117. Soukup, S.F., Pocha, S.M., Yuan, M., and Knust, E. (2013). DLin-7 is required in postsynaptic lamina neurons to prevent light-induced photoreceptor degeneration in drosophila. Curr. Biol. *23*, 1349–1354. https://doi.org/10.1016/j.cub.2013.05.060.

Please cite this article in press as: Bademosi et al., EndophilinA-dependent coupling between activity-induced calcium influx and synaptic autophagy is disrupted by a Parkinson-risk mutation, Neuron (2023), https://doi.org/10.1016/j.neuron.2023.02.001



## STAR★METHODS

### KEY RESOURCES TABLE

| REAGENT or RESOURCE | SOURCE | IDENTIFIER |
|---|---|---|
| Antibodies | | |
| anti-endophilinA | Verstreken et al. | N/A |
| anti-Horseradish Peroxidase (HRP) | BioConnect | Cat#: 323-005-021; RRID: AB_2314648 |
| anti-GAPDH | Thermo Fisher | Cat#: PAI-16777 |
| anti-EndophilinA1 | Santa Cruz | Cat#: sc-48378; RRID: AB_628098 |
| anti-EndophilinA1 | GeneTex | Cat#: GTX32872 |
| anti-DLG | Developmental Studies Hybridoma Bank | Cat: 4F3; RRID: AB_528203 |
| anti-SOX2 | Santa Cruz | Cat#: sc-365823; RRID: AB_10842165 |
| anti-OCT4 | Abcam | Cat#: ab19857; RRID: AB_445175 |
| anti-NANOG | Santa Cruz | Cat#: sc-293121; RRID: AB_2665475 |
| anti-LMX1A/B | Millipore | Cat#: AB10533; RRID: AB_10805970 |
| anti-FOXA2 | Santa Cruz | Cat#: 101060; RRID: AB_1124660 |
| anti-Engrailed-1 (4G11) | Developmental Studies Hybridoma Bank | Cat#: AB_2314371; RRID: AB_528219 |
| anti-OTX2 | Santa Cruz | Cat#: sc-514195; RRID:AB_2921699 |
| anti-LC3B | Cell Signaling | Cat#: 2775S; RRID: AB_915950 |
| anti-Tyrosine Hydroxylase (TH) | Millipore | Cat#: AB152; RRID: AB_390204 |
| anti-Tyrosine Hydroxylase (TH) | Santa Cruz | Cat#: sc-25269; RRID: AB_628422 |
| anti-MAP2 | Abcam | Cat#: ab5392; RRID: AB_2138153 |
| anti-Dynamin | BD Biosciences | Cat#: 610246; RRID: AB_397641 |
| anti-Dynamin1 | Invitrogen | Cat#: MA515285; RRID: AB_10981827 |
| anti-Dynamin1 | Santa Cruz | Cat#: sc-12724; RRID: AB_2230650 |
| anti-Glutathione S-transferase (GST) | Invitrogen | Cat#: A5800; RRID: AB_1500200 |
| Alexa Fluor 488 goat anti-mouse IgG1 | Invitrogen | Cat#: A21121; RRID: AB_2535764 |
| Alexa Fluor 488 goat anti-rabbit | Invitrogen | Cat#: A11034; RRID: AB_2576217 |
| Alexa Fluor 555 goat anti-mouse IgG2a | Invitrogen | Cat#: A21137; RRID: AB_2535776 |
| Alexa Fluor 555 goat anti-rabbit | Invitrogen | Cat#: A27039; RRID: AB_2536100 |
| Alexa Fluor 647 goat anti-mouse | Invitrogen | Cat#: A21236; RRID: AB_2535805 |
| Alexa Fluor 647 goat anti-guinea pig | Invitrogen | Cat#: A21450; RRID: AB_2735091 |
| Alexa Fluor 647 goat anti-rabbit | Invitrogen | Cat#: A21245; RRID: AB_2535813 |
| Alexa Fluor 647 goat anti-chicken | Invitrogen | Cat#: A21449; RRID: AB_2535866 |
| Bacterial and virus strains | | |
| *E.coli* BL21(DE3) | F. Rousseau & J. Schymkowitz | N/A |
| Chemicals, peptides, and recombinant proteins | | |
| Nefiracetam | Santa Cruz | Cat#: SC-205766 |
| PreScission Protease | GE Healthcare | Cat#: 27084301 |
| Chloroquine | Sigma | Cat#: C6628 |
| EndophilinA WT | This study | N/A |
| EndophilinA D265A | This study | N/A |
| EndophilinA D265R | This study | N/A |
| EndophilinA1 WT | This study | N/A |
| EndophilinA1 G276V | This study | N/A |

(*Continued on next page*)

Please cite this article in press as: Bademosi et al., EndophilinA-dependent coupling between activity-induced calcium influx and synaptic autophagy is disrupted by a Parkinson-risk mutation, Neuron (2023), https://doi.org/10.1016/j.neuron.2023.02.001





*Continued*

| REAGENT or RESOURCE | SOURCE | IDENTIFIER |
|---|---|---|
| **Critical commercial assays** | | |
| Dynabeads Protein G | Thermo Fisher | Cat#: 10003D |
| **Experimental models: Cell lines** | | |
| Human iPSC: ctrl65 (SFC065) | Baumann et al. | N/A |
| Human iPSC: SH3GL2 mutant G276V | This study | N/A |
| SH-SY5Y | ATCC | CRL-2266 |
| **Experimental models: Organisms/strains** | | |
| *D. melanogaster*: $w^{1118}$ | BDSC | RRID: BDSC_3605; Fly base: FBal0018186 |
| *D. melanogaster*: $endoA^{26}$ | Guichet et al. | N/A |
| *D. melanogaster*: $endoA^{\Delta 4}$ | Verstreken et al. | Fly base: FBal0135727 |
| *D. melanogaster*: GMR57C10-Gal4 | BDSC | RRID: BDSC_39171; Fly base: FBti0137043 |
| *D. melanogaster*: longGMR-Gal4 | BDSC | RRID: BDSC_8605; Fly base: FBti0058798 |
| *D. melanogaster*: Atg8mCherry | Hegedus et al. | N/A |
| *D. melanogaster*: UAS Atg3 RNAi | BDSC | RRID: BDSC_34359; Fly base: FBal0257941 |
| *D. melanogaster*: UAS EndoA WT | This study | N/A |
| *D. melanogaster*: UAS EndoA D265A | This study | N/A |
| *D. melanogaster*: UAS EndoA D265R | This study | N/A |
| *D. melanogaster*: UAS EndoA S75D+D265A | This study | N/A |
| *D. melanogaster*: UAS EndoA S75A+D265R | This study | N/A |
| *D. melanogaster*: UAS EndoA S75A | This study | N/A |
| *D. melanogaster*: UAS EndoA S75D | This study | N/A |
| *D. melanogaster*: UAS SH3GL2 WT | This study | N/A |
| *D. melanogaster*: UAS SH3GL2 G276V | This study | N/A |
| *D. melanogaster*: UAS mEOS3.1::EndoA WT | This study | N/A |
| *D. melanogaster*: UAS mEOS3.1::EndoA D265A | This study | N/A |
| *D. melanogaster*: UAS mEOS3.1::EndoA D265R | This study | N/A |
| *D. melanogaster*: UAS mEOS3.1::SH3GL2 WT | This study | N/A |
| *D. melanogaster*: UAS mEOS3.1::EndoA D265R | This study | N/A |
| *D. melanogaster*: UAS GCaMP6m | BDSC | RRID: BDSC_42748; Fly base: FBtp0083046 |
| *D. melanogaster: cn bw* | BDSC | RRID: BDSC_264; Fly base: FBst0000264 |
| **Oligonucleotides** | | |
| Primers for cloning, see Table S5 | This paper | N/A |
| gBlocks for cloning, see Table S5 | This paper | N/A |
| Primers for gene-editing validation, see Table S5 | This paper | N/A |
| Primers for RT-PCR in fruit flies, see Table S5 | This paper | N/A |
| Oligo for iPSC gene editing: ssODN_G276V_AvaII: cgaatgagcctgGAGtttccaactggagacagtactcagcc caatggCgtCctctcccacacaggcactcccaaaccttcag gtaagagctgaaactgca | This paper | N/A |
| **Recombinant DNA** | | |
| pMB1610_pRR-Puro | Flemr M. and Buhler M. | Marc Bühler RRID: Addgene_65853 |
| pSpCas9(BB)-2A-GFP (PX458) | Ran et al. | Feng Zhang RRID: Addgene_48138 |
| pASUT-attB-w* | K. Basler | GenBank: EF362409.1 |
| pGEX-6P-1 | F. Rousseau & J. Schymkowitz | GenBank: U78872.1 |
| pUAST_EndoA-WT | This study | N/A |
| pUAST_EndoA-D265A | This study | N/A |
| pUAST_EndoA-D265R | This study | N/A |
| pUAST_EndoA-S75A | This study | N/A |

(*Continued on next page*)

Please cite this article in press as: Bademosi et al., EndophilinA-dependent coupling between activity-induced calcium influx and synaptic autophagy is disrupted by a Parkinson-risk mutation, Neuron (2023), https://doi.org/10.1016/j.neuron.2023.02.001



*Continued*

| REAGENT or RESOURCE | SOURCE | IDENTIFIER |
|---|---|---|
| pUAST_EndoA-S75D | This study | N/A |
| pUAST_EndoA-S75D+D265A | This study | N/A |
| pUAST_EndoA-S75A+D265R | This study | N/A |
| pUAST_EndoA-WT_mEOS3.1 | This study | N/A |
| pUAST_EndoA-D265A_mEOS3.1 | This study | N/A |
| pUAST_EndoA-D265R_mEOS3.1 | This study | N/A |
| pUAST_SH3GL2-WT | This study | N/A |
| pUAST_SH3GL2-G276V | This study | N/A |
| pUAST_SH3GL2-WT_mEOS3.1 | This study | N/A |
| pUAST_SH3GL2-G276V_mEOS3.1 | This study | N/A |
| pGEX-6P-1_EndoA-WT | This study | N/A |
| pGEX-6P-1_EndoA-D265A | This study | N/A |
| pGEX-6P-1_EndoA-D265R | This study | N/A |
| pGEX-6P-1_SH3GL2-WT | This study | N/A |
| pGEX-6P-1_SH3GL2-G276V | This study | N/A |
| pX_SH3GL2_G276V_gRNA1 | This study | N/A |
| pRR_SH3GL2(G276V) | This study | N/A |
| Software and algorithms | | |
| GraphPad Prism 9 | GraphPad Software | https://www.graphpad.com/scientific-software/prism/ |
| ImageJ-win64 | National Institute of Health | https://imagej.nih.gov/ij/ |
| Inkscape 1.1.2 | Inkscape's Contributors | https://inkscape.org/de/release/inkscape-1.1.2/ |
| NIS-Elements | Nikon | https://www.microscope.healthcare.nikon.com/ |
| Axoscope 10.7 | Molecular Devices | https://support.moleculardevices.com/s/article/Molecular-Devices-Software |
| Igor Pro 6.37 | Wave Metrics | https://www.wavemetrics.com/ |
| Axoclamp900A | Molecular Devices | https://support.moleculardevices.com/s/article/Molecular-Devices-Software |
| Clampex 10.7 | Molecular Devices | https://support.moleculardevices.com/s/article/Molecular-Devices-Software |
| Clampfit 10.7 | Molecular Devices | https://support.moleculardevices.com/s/article/Molecular-Devices-Software |
| Canvas 15 | ACD Systems | https://help.acdsystems.com/en/canvas-15/canvas_15.htm |
| Zen black | Zeiss | https://www.zeiss.com/ |
| MetaMorph | Molecular Devices | https://support.moleculardevices.com/s/article/Molecular-Devices-Software |
| GIMP 2.10.30 | GIMP | https://www.gimp.org/ |
| CLC workbench 22 | Qiagen | https://digitalinsights.qiagen.com/products/clc-main-workbench-direct-download/ |
| LAS v4.0 | Leica | https://www.leica-microsystems.com/ |
| LightCycler 480 Software | Roche | https://diagnostics.roche.com/ |
| Wyatt Dynamics Software v7 | Wyatt | N/A |
| Uncle Software 4.0 | Unchained Labs | N/A |
| Invenio Software | Bruker | N/A |
| ATSAS PRIMUS | EMBL | https://www.embl-hamburg.de/biosaxs/software.html |
| CHROMIXS | EMBL | https://www.embl-hamburg.de/biosaxs/software.html |
| FOXTROT | ESRF | https://www.esrf.fr/ |
| BsxCuBE | ESRF | https://www.esrf.fr/ |
| DynamX 3.0 | Waters | https://www.waters.com/waters/library.htm?locale=en_US&lid=134832928 |
| PyHDX v0.4.1 | Smit et al. | N/A |

Please cite this article in press as: Bademosi et al., EndophilinA-dependent coupling between activity-induced calcium influx and synaptic autophagy is disrupted by a Parkinson-risk mutation, Neuron (2023), https://doi.org/10.1016/j.neuron.2023.02.001



CellPress
OPEN ACCESS

## RESOURCE AVAILABILITY

### Lead Contact

Further information and requests for resources and reagents should be directed to the Lead Contact Patrik Verstreken (patrik.verstreken@kuleuven.be).

### Materials Availability

Data and reagents are available upon request.

### Data and Code Availability

- All data reported in this paper will be shared by the lead contact upon request.
- This paper does not report original code.
- Any additional information required to reanalyze the data reported in this paper is available from the lead contact upon request.

## EXPERIMENTAL MODEL AND SUBJECT DETAILS

### Fly stocks and maintenance

Flies were grown on standard cornmeal and sugar beet syrup medium at 25 °C. The *Drosophila* wildtype and mutant (D265A, D265R) cDNA of EndophilinA, as well as human wildtype and mutant (G276V) SH3GL2 were cloned into the pUAST-attB vector and flies generated by in-house embryo injection or at Bestgene Inc into the VK37 locus to establish *UAS-EndoA$^{WT}$*, *UAS-EndoA$^{D264A}$*, *UAS-EndoA$^{D264R}$*, *UAS-SH3GL2$^{WT}$*, *UAS-SH3GL2$^{G276V}$* lines and the mEOS3.1 tagged lines. Genomic *w$^{+}$; Atg8$^{3\times mCherry}$* (hereafter Atg8$^{mCherry}$) flies were a gift from Gabor Juhasz.[93] y[1] sc[*] v[1] sev[21]; P{y[+t7.7] v[+t1.8]=TRiP.HMS01348}attP2 (hereafter UAS-RNAi-Atg3) flies were purchased from Bloomington Drosophila Stock Center (#34359). *w*; endoA$^{26}$* from[49] and *w*; endoA$^{\Delta 4}$* from.[38] Both male and female flies were included in the study. Based on the experiment, either larvae or adult animals were used, as specified in the 'method details' section.

The following genotypes were used:

*w*;UAS-endoA$^{WT}$/+;endoA$^{26}$/endoA$^{\Delta 4}$,GMR57C10-GAL4* (where *GMR57C10-Gal4* is referred to as *nSyb-Gal4*)
*w*;UAS-endoAD$^{265A}$/+;endoA$^{26}$/endoA$^{\Delta 4}$,GMR57C10-GAL4*
*w*;UAS-endoAD$^{265R}$/+;endoA$^{26}$/endoA$^{\Delta 4}$,GMR57C10-GAL4*
*w*;GMR57C10-GAL4/+*
*w*; endoA$^{26}$/endoA$^{\Delta 4}$*
*w1118CS*
*w1118; genomic Atg8$^{3\times mCherry}$/+*
*w*;GMR57C10-GAL4/ genomic Atg8$^{3\times mCherry}$*
*w*;genomic endo$^{AS75A}$/+; endoA$^{26}$/EndoA$^{\Delta 4}$, genomic Atg8$^{3\times}$*
*w*; UAS-RNAi-Atg3/GMR57C10-GAL4;genomic Atg8$^{3\times mCherry}$/+*
*w*; GMR57C10-GAL4/+;genomic Atg8$^{3\times mCherry}$/+*
*w*;UAS-endoA$^{WT}$/GMR57C10-GAL4;endoA$^{26}$/EndoA$^{\Delta 4}$, genomic Atg8$^{3\times mCherry}$*
*w*;UAS-endoAD$^{265A}$/GMR57C10-GAL4;endoA$^{26}$/endoA$^{\Delta 4}$, genomic Atg8$^{3\times mCherry}$*
*w*;UAS-endoAD$^{265R}$/GMR57C10-GAL4;endoA$^{26}$/endoA$^{\Delta 4}$, genomic Atg8$^{3\times mCherry}$*
*w*;UAS-SH3GL2$^{WT}$/GMR57C10-GAL4;endoA$^{26}$/endoA$^{\Delta 4}$, genomic Atg8$^{3\times mCherry}$*
*w*;UAS-SH3GL2$^{G276V}$/GMR57C10-GAL4;endoA$^{26}$/endoA$^{\Delta 4}$, genomic Atg8$^{3\times mCherry}$*
*w*;UAS-SH3GL2$^{WT}$/+;endoA$^{26}$/endoA$^{\Delta 4}$, GMR57C10-GAL4*
*w*;UAS-SH3GL2$^{G276V}$/+;endoA$^{26}$/endoA$^{\Delta 4}$, GMR57C10-GAL4w;GMR57C10-Gal4/+; genomic Atg8$^{3\times mCherry}$ /+*
*w*;UAS-GCaMP6m/+;GMR57C10-GAL4/+*
*w*;UAS-endoA$^{WT}$,cn bw/cn bw;endoA$^{26}$/longGMR-GAL4*
*w*;UAS-endoA$^{D254A}$,cn bw/cn bw;endoA$^{26}$/longGMR-GAL4*
*w*;UAS-endoA$^{D254R}$,cn bw/cn bw;endoA$^{26}$/longGMR-GAL4*
*w*;cn bw/cn bw;longGMR-GAL4/+*
*w*;UAS-mEOS3.1::endoA$^{WT}$/+;endoA$^{26}$/endoA$^{\Delta 4}$,GMR57C10-GAL4*
*w*;UAS-mEOS3.1::endoA$^{D265A}$/+;endoA$^{26}$/endoA$^{\Delta 4}$,GMR57C10-GAL4*
*w*;UAS-mEOS3.1::endoA$^{D265R}$/+;endoA$^{26}$/endoA$^{\Delta 4}$,GMR57C10-GAL4*
*w*;UAS-endoA$^{S75D+D265A}$/GMR57C10-GAL4;endoA$^{26}$/endoA$^{\Delta 4}$, genomic Atg8$^{3\times mCherry}$*
*w*;UAS-endoA$^{S75A+D265R}$/GMR57C10-GAL4;endoA$^{26}$/endoA$^{\Delta 4}$, genomic Atg8$^{3\times mCherry}$*
*w*;UAS-endoA$^{S75D}$/GMR57C10-GAL4;endoA$^{26}$/endoA$^{\Delta 4}$, genomic Atg8$^{3\times mCherry}$*
*w*;UAS-endoA$^{S75A}$/GMR57C10-GAL4;endoA$^{26}$/endoA$^{\Delta 4}$, genomic Atg8$^{3\times mCherry}$*
*w*;UAS-endoA$^{WT}$/GMR57C10-GAL4;genomic Atg8$^{3\times mCherry}$*

Please cite this article in press as: Bademosi et al., EndophilinA-dependent coupling between activity-induced calcium influx and synaptic autophagy is disrupted by a Parkinson-risk mutation, Neuron (2023), https://doi.org/10.1016/j.neuron.2023.02.001



*w*;UAS-endoA$^{D265R}$/GMR57C10-GAL4;genomic Atg8$^{3\times mCherry}$*
*w*;UAS-endoA$^{S75D+D265A}$/+; endoA$^{26}$/endoA$^{\Delta 4}$, GMR57C10-GAL4*
*w*;UAS-endoA$^{S75A+D265R}$/+; endoA$^{26}$/endoA$^{\Delta 4}$, GMR57C10-GAL4*
*w*;UAS-endoA$^{S75D}$/+; endoA$^{26}$/endoA$^{\Delta 4}$, GMR57C10-GAL4*
*w*;UAS-endoA$^{S75A}$/+; endoA$^{26}$/endoA$^{\Delta 4}$, GMR57C10-GAL4*
*w*;UAS-mEOS3.1::SH3GL2$^{WT}$/+;endoA$^{26}$/endoA$^{\Delta 4}$,GMR57C10-GAL4*
*w*;UAS-mEOS3.1::SH3GL2$^{G276V}$/+;endoA$^{26}$/endoA$^{\Delta 4}$,GMR57C10-GAL4*

### iPSC maintenance and differentiation

iPSC from a control line (SFC065) and *SH3GL2* p.G276V knock-in line were differentiated into ventral midbrain dopaminergic neurons as described in the methods section. Briefly, hiPSC were maintained on matrigel-coated plates with mTeSR-Plus medium (Stem Cell Technologies) and medium changes were performed every two days. At day 18 of differentiation, neural progenitors were plated on coverslips coated with poly-D-lysine and mouse laminin in terminal differentiation medium. Human control iPSC line (SFC065) was used in accordance with an MTA with the University of Lübeck (Germany) and registered in the KU Leuven/UZ Leuven Biobank.

## METHOD DETAILS

### Plasmids generation

- pUAST_EndoA-WT

Gibson Assembly with EndoA PCR fragment and pUAST attB w+ linearized with EcoRI and XhoI. The PCR to obtain EndoA-WT sequence performed with primers FW EndoA WT and Rc EndoA WT (see primer sequences in Table S5).

- pUAST_EndoA-D265R

Gibson Assembly with EndoA D265R gBlock and pUAST attB w+ linearized with EcoRI and XhoI.

- pUAST_EndoA-D265A

Gibson Assembly with EndoA D265A gBlock and pUAST attB w+ linearized with EcoRI and XhoI.

- pUAST_EndoA-S75A

Gibson Assembly with EndoA S75A gBlock and pUAST_attB w+ linearized with EcoRI and XhoI.

- pUAST_EndoA-S75A+D265R

Gibson Assembly with EndoA S75A+D265R gBlock and pUAST_attB w+ linearized with EcoRI and XhoI.

- pUAST_EndoA-S75D

Gibson Assembly with EndoA S75D gBlock and pUAST_attB w+ linearized with EcoRI and XhoI.

- pUAST_EndoA-S75D+D265A

Gibson Assembly with EndoA S75D+D265A gBlock and pUAST_attB w+ linearized with EcoRI and XhoI.

- pUAST_EndoA-WT-mEOS3.1-v5, pUAST_EndoA-D265R-mEOS3.1-v5 and pUAST_EndoA-D265A-mEOS3.1-v5

These plasmids were made by respectively performing a restriction digest on pUAST_EndoA-WT, pUAST_EndoA-D264R, pUAST_EndoA-D265A with AgeI and XbaI and doing a Gibson assembly with gBlock mEOS3.1.

All plasmids contain the EndoA CDS (WT or mutation), a short flexible linker (GGTGGS), mEOS3.1, again a short flexible linker (GGTGGS) and a V5 epitope tag.

- pUAST_SH3GL2-WT

Gibson Assembly with SH3GL2 WT gBlock and pUAST attB w+ linearized with EcoRI and XhoI.

- pUAST_SH3GL2-G276V

Gibson Assembly with SH3GL2 G276V gBlock and pUAST attB w+ linearized with EcoRI and XhoI.

- pUAST-SH3GL2$^{WT}$-mEOS3.1 and pUAST-SH3GL2$^{G276V}$-mEOS3.1

Please cite this article in press as: Bademosi et al., EndophilinA-dependent coupling between activity-induced calcium influx and synaptic autophagy is disrupted by a Parkinson-risk mutation, Neuron (2023), https://doi.org/10.1016/j.neuron.2023.02.001



CellPress
OPEN ACCESS

These plasmids were generated by Gibson assembly with two fragments inserted in a pUAST_attB w+ vector linearized with XhoI and EcoRI. One fragment amplified from pUAST_SH3GL2-WT and pUAST_SH3GL2-G276V with primers Fw SH3GL2 EOS and Rc SH3GL2 EOS.

The other fragment was amplified from the pUAST_EndoA-WT-mEos3.1-V5 vector with primers: Fw SH3GL2 EOS_2 and Rc SH3GL2 EOS_2. For primer sequences see Table S5.

- pGEX-6P-1_EndoA-WT, pGEX-6P-1_EndoA-D265A and pGEX-6P-1_EndoA-D265R

These plasmids were generated by performing a PCR respectively from pUAST_EndoA-WT, pUAST_EndoA-D265A and pUAST_EndoA-D265R with primers Fw EndoA pGEX and Rc EndoA pGEX (see Table S5).

Gibson assembly was performed with the PCR fragments and pGEX-6P-1 linearized with BamHI and EcoRI

- pGEX-6P-1_SH3GL2-WT

Gibson assembly performed with codon optimized SH3GL2 WT gBlock_CodOpt and pGEX-6P-1 linearized with BamHI and EcoRI.

- pGEX-6P-1_SH3GL2-G267V

Gibson assembly performed with codon optimized SH3GL2 G276V gBlock_CodOpt and pGEX-6P-1 linearized with BamHI and EcoRI.

-pRR_SH3GL2(G276V)

This plasmid was cloned from pMB1610_pRR-Puro plasmid (gift from Marc Bühler; Addgene plasmid #65853; http://n2t.net/addgene:65853; RRID: Addgene 65853)[94] with primers SH3GL2(G276V)_pRR_Fwd and SH3GL2(G276V)_pRR_Rv.

-pX_SH3GL2_G276V_gRNA1

This plasmid was cloned from pSpCas9(BB)-2A-GFP (PX458) (gift from Feng Zhang; Addgene plasmid # 48138; http://n2t.net/addgene:48138; RRID: Addgene_48138)[95] with primers px_SH3GL2_G276V_gRNA1_Fwd and px_SH3GL2_G276V_gRNA1_Rv.

### Autophagy induction assays

Third instar larvae (still crawling in the food) expressing $Atg8^{mCherry}$ were dissected in fresh $Ca^{2+}$-free HL3 (100 mM NaCl, 5 mM KCl, 10 mM $NaHCO_3$, 5 mM Hepes, 30 mM sucrose, 5 mM trehalose and 10 mM $MgCl_2$, pH 7.2).

For electrical stimulation the nerves of dissected larvae were cut just below the ventral nerve cord, and axons innervating segments A3 and A4 were stimulated at 20 Hz for 30 min at 50 % above the threshold using a suction electrode.[15] During electrical stimulation, larvae were incubated in HL3 supplemented with or without 1 mM $CaCl_2$, as indicated. EGTA-AM (Thermo Fisher) was used at 25 μM (in anhydrous 0.1 % DMSO).

For calcium channel agonist treatment larvae were prepared as for electrical stimulation and then incubated for 30 min in HL3 with 10 μM of Nefiracetam (Santa Cruz), dissolved in 0,0025 % anhydrous DMSO,[35,36] and with or without 1 mM $CaCl_2$. 100 μM of NAS was similarly used to prevent muscle contractions.

For testing autophagy flux, third instar larvae were placed for 4 h in food supplemented with 10 mg/ml Chloroquine (Sigma). Control animals were kept in normal food without supplements. Larvae were then dissected in fresh HL3 and incubated for 30 min in HL3 supplemented with 10 μM of Nefiracetam (Santa Cruz), 1 mM $CaCl_2$ and 100 μM of NAS (Sigma) and Chloroquine in case of treated animals.

For starvation induced autophagy, experiments were carried out as described in[15]. Briefly, prior to imaging, third instar larvae were placed for 4 hours on starvation plates (20 % sucrose, 1 % agarose), while control animals were fed normally. In all experiments 100 μM 1-Naphthylacetyl spermine trihydrochloride – NAS (Sigma) was added[15,96] to prevent muscle contractions.

### Confocal Live Imaging and quantification

Live imaging of dissected larvae was carried out on a Nikon A1R confocal microscope with a 60X (NA 1.0) water-dipping lens. Dissected larvae were washed multiple times in HL3 prior to imaging. NIS Elements (Nikon) was used for data acquisition using the Resonant Scanning option, with a zoom factor of 3 and line averaging of 16. All images were acquired with a pinhole of one Airy unit and a resolution of 1024 × 1024. Z-stacks were used in data acquisition to capture fluorescence (puncta presence) across the whole NMJ. Low basal autophagy levels were always confirmed in control experiments.

Quantification of the number of puncta within synaptic boutons was performed in ImageJ.[15] $Atg8^{3\times mCherry}$ puncta were manually counted and this was combined with the application of a threshold mask as to determine the area of the bouton. Trafficking autophagosomes (punctae in motor neuron axons outside the NMJ) were excluded from data analysis. The conditions were blinded for quantification.

Please cite this article in press as: Bademosi et al., EndophilinA-dependent coupling between activity-induced calcium influx and synaptic autophagy is disrupted by a Parkinson-risk mutation, Neuron (2023), https://doi.org/10.1016/j.neuron.2023.02.001



### Calcium imaging

Third instar larvae expressing GCaMP6m in neurons (GMR57C10-GAL4) were dissected in fresh HL3 and nerves cut below the ventral nerve cord. After dissection, HL3 was replaced with freshly prepared 100 μM Nas (Sigma) and 2 mM $CaCl_2$ in HL3. Larval filets were imaged on a widefield Nikon Eclipse FN1 upright microscope equipped with a water dipping 20X lens (NA 0.95) and a GFP filter. Time-lapse images were acquired at a frequency of 5 Hz. Nefiracetam or DMSO (control) was added during imaging. Image analysis was performed using ImageJ. GCaMP6m intensity was plotted as $\Delta F/F_0$ and measured, after background subtraction, by normalizing the signal, within the synaptic boutons, in each frame to the averaged GCaMP6m intensity, for the same region of interest, of the first 10 frames.

Terminally differentiated neurons were transfected with GCaMP6f. Five days after transfection, cultures were imaged on a widefield Nikon Eclipse FN1 upright microscope equipped with a 10X lens (NA 0.3) and a GFP filter. Time-lapse images were acquired at a frequency of 6 Hz. Image analysis was performed using ImageJ. In summary, first the ROIs of the cells in each field of view were determined. After producing a maximum projection of the GCaMP signal, the background intensity was subtracted, and the images were thresholded. Using the analyze particles plugin the ROI of each cell was saved. Next, the ROIs were selected in the unprocessed image and the plugin TimeSeries V3_0 was used to get the average fluorescence intensity of each cell (ROI) over time. Next, the average change in fluorescence intensity relative to the resting fluorescence intensity ($\Delta F/F_0$) was calculated. $F_0$ was calculated as the average of local minima of the fluorescence intensities recorded over time. Local maxima of fluorescence peaks in each cell were considered when the maxima was above a pre-established threshold (background noise). Data are presented as 'peak activity' (average counts of activity peaks (local maxima of fluorescence peaks above the threshold) for all selected cells per field of view over time normalized to the number of frames of the time-lapse) and 'average peak amplitude' (average of the amplitude of the local maxima above the threshold per time-lapse).

### Immunohistochemistry and confocal imaging

Third instar larvae were dissected in cold $Ca^{2+}$ free HL3 and fixed for 20 minutes at room temperature with 4 % para-formaldehyde. Fixed larvae were permeabilized with 0.4 % PBX (TritonX-100 in 1X PBS), blocked for 1 hour with 10 % normal goat serum in PBX and incubated overnight at 4°C with primary antibodies. After several washes, larval filets were incubated with secondary antibodies for 90 min at room temperature. Samples were mounted in Vectashield (Vector Laboratories).

Brains of aged flies were dissected in cold PBS and fixed in 4 % PFA for 20 min at RT and blocked for 1 h with 5 % NGS in 0.4 % Triton X-100 in PBS. Primary antibodies were incubated at 4°C for 1.5 days and secondary antibodies at 4°C for 1 day. Stained brains were mounted in RapiClear 1.47 (SUNJin Lab).

The following antibodies were used: guinea pig anti-EndoA (GP69) [1:2000[38]], rabbit anti-HRP [1:1000 (Jackson ImmunoReasearch)], anti-SH3GL2 [1:1000 (GeneTex)], anti-TH [1:200 (Millipore)], anti-DLG [1:50 (DSHB)]. Alexa Fluor-488/Alexa Fluor-555 conjugated secondary antibodies [1:1000 (Invitrogen)].

Larval samples were imaged on a Nikon A1R confocal microscope with a 60X (NA 1.4) oil lens. Acquisition performed using a resonant scanner, a zoom factor of 3 and line averaging of 16. All images were acquired with a pinhole of 1 Airy unit and a resolution of 1024 × 1024. Z-stacks (step intervals of 0.45 μm) were used in data acquisition and the same image settings were maintained across the genotypes. Quantification of fluorescent intensity and NMJ area was performed with ImageJ. Imaging of adult brains was performed on a Nikon A1R confocal microscope with a 20X (NA 0.95) water immersion lens. Acquisition performed using a galvano scanner with line averaging of 2. All images were acquired with a pinhole of 1 Airy unit and a resolution of 1024 × 1024. Z-stacks acquired with a step interval of 2 μm.

For the characterization of iPSCs and midbrain floor plate progenitors, cells were fixed at day 16 of differentiation for 15 min in 4 % para-formaldehyde. Cells were blocked for 1 h at room temperature with 3 % normal goat serum + 0.3 % Triton X-100 (Sigma) in DPBS supplemented with $Ca^{2+}$ and $Mg^{2+}$ (Life Technologies). Primary antibodies were incubated overnight at 4°C in blocking solution. Secondary antibodies were incubated for 1 h at room temperature in blocking solution. Coverslips were mounted in Mowiol (Sigma) and imaged on an upright Nikon A1R confocal microscope equipped with a DIC N2 20X lens (NA 0.75). Z-stacks were acquired with pinhole of 1 Airy unit, a Galvano scanner with line averaging of 2, image size of 1024 x 1024 pixels and step intervals of 2 μm (for imaging of iPSCs) and 0.5 μm (for imaging of midbrain floor plate progenitors).

For the quantification of autophagy induction, terminally differentiated vmDAn (55-60 days) were fixed for 15 min in 4 % para-formaldehyde and blocked for 1 h at room temperature in 3 % normal goat serum + 0.01 % Saponin (Sigma) in DPBS supplemented with with $Ca^{2+}$ and $Mg^{2+}$ (Life Technologies). Primary antibodies were diluted in blocking solution and incubated overnight at 4°C, while secondary antibodies were incubated for 1 h at room temperature. Coverslips were mounted with Mowiol (Sigma) and imaged on an upright Nikon A1R confocal microscope equipped with an oil immersion Apo 60X lens with (NA 1.4). Z-stacks were acquired with a pinhole of 1 Airy unit, a Galvano scanner with line averaging of 2, image size of 1024 x 1024 pixels and step intervals of 0.3 μm.

The following antibodies were used: mouse IgG1 anti-SOX2 [1:200 (Santa Cruz)], rabbit anti-OCT4 [1:50 (Abcam)], mouse IgG1 anti-NANOG [1:50 (Santa Cruz)], rabbit anti-LMX1A/B [1:1000 (Millipore)], mouse IgG2a anti-FOXA2 [1:250 (Santa Cruz)], mouse IgG1 anti-Engrailed-1 [1:100 (DSHB, 4G11)], mouse IgG2a anti-OTX2 [1:100 (Santa Cruz)], Rabbit anti-LC3B [1:250 (Cell Signaling)], rabbit anti-TH [1:500 (Sigma)], mouse IgG2a anti-TH [1:500 (Santa Cruz)], Chicken anti-MAP2 [1:500 (Abcam)], mouse IgG1 anti-alpha-Tubulin [1:500 (DSHB 12G10)], Alexa Fluor-488/ Alexa Fluor-555/ Alexa Fluor-647 conjugated secondary antibodies [1:500 (Invitrogen)].

Please cite this article in press as: Bademosi et al., EndophilinA-dependent coupling between activity-induced calcium influx and synaptic autophagy is disrupted by a Parkinson-risk mutation, Neuron (2023), https://doi.org/10.1016/j.neuron.2023.02.001



CellPress
OPEN ACCESS

### Zeiss Airyscan Confocal Imaging and quantification

A Zeiss LSM 880 (AiryScan detector enabled) with a 63X (NA 1.4) was used to image the distribution of EndoA (WT, D265A, D265R, S75A+D265R, S75R+D265A and endogenous EndoA) across the NMJ. Zen Black software (2012, Carl Zeiss) was used for image acquisition and processing.

To quantify the distribution of EndoA within boutons, we selected boutons of similar size as previously described.[97] These were then rescaled to a standard diameter and average the labelling intensities per position along the bouton diameter were defined. Boutons were resized to a width of 500 pixels, and integrated intensity was calculated for whole boutons fit into a 400 pixel diameter, while cytosol integrated intensity was calculated by 250 pixel diameter circle (in ImageJ). The average integrated intensity was calculated across all boutons of the same genotype.

### Single-particle tracking photoactivated localization microscopy (sptPALM)

SptPALM was carried out on transgenic EndophilinA-mEOS3.1 (wildtype, D264A and D264R) expressing *Drosophila* third-instar larvae which were dissected on a PDMS (Sylgard) base as previously described.[14,54,55] Briefly, EndoA$^{WT::mEos3.1}$, EndoA$^{DA:mEos3.1}$ and EndoA$^{DR:mEos3.1}$ were imaged at the larvae synaptic boutons on muscle 13 of segments A3 and A4 using total internal reflection (TIRF) microscopy under slightly oblique illumination. The dissected larvae were inverted onto glass-bottomed imaging dishes (MatTek Corporation). The larvae were perfused with HL3, or a solution mixture of HL3, 10 μM Nefiracetam, 100 μM NAS and 1 mM $CaCl_2$. Acquisition of single EndoA-mEOS3.1 molecules was carried out using a C-Apochromat 63X (NA 1.2) water objective on the ELYRA PS.1 microscope (Zeiss). Synaptic boutons were located using 488 nm laser illumination. A 405 nm laser was used for photoconversion, and the 561 nm laser was used during acquisition. To spatially visualize and temporally characterize individual photoconverted fluorophores, the 405 nm laser was used at 0.00003-0.03 % power, while the 561 nm laser was used at 20 % power. A sensitive electron-multiplying charge-coupled device (EMCCD) camera (Evolve, Photomertic) was used to collect single molecule fluorescence. Zen Black acquisition software (2012 version, Carl Zeiss) was utilized for movie acquisition. 15,000 frames images were captured per synaptic bouton at a frame capture rate of 20 Hz. Analysis of sptPALM movies is described in the Supplemental Experimental Procedure.

### sptPALM Analysis

NIH ImageJ was used to convert movies from Zen's CZI format to the format recognizable for the image analysis software – Tiff format. PALM-Tracer, a customized-written software plugin in Metamorph (Molecular Devices)[98,99] was used to localize single molecules and quantify their mobility. Mobility data was plotted as mean square displacement ($\mu m^2$) values (equation 1) as well as diffusion coefficient ($\mu m^2\ s^{-1}$) values (equation 2). The parameters were set to isolate and recognize trajectories of molecules undergoing free cytosolic diffusion, associated with organelles or bound to presynaptic plasma membrane. Only fluorescent molecules with sufficient threshold and with consecutive appearance across eight movie frames were tracked and used for data analysis. The PALM-Tracer software generated trajectory maps, super-resolved average intensity as well as diffusion coefficient maps. The colour gradient in the trajectory maps indicate the time of detection of the tracks; the blue trajectories indicate molecules detected early during movie acquisition, while the white trajectories indicate later appearance and detection.

$$MSD(n \times \Delta t) = \sum_{i=1}^{N-n} \frac{[x((i+n) \times \Delta t) - x(i \times \Delta t)]^2 + [y((i+n) \times \Delta t) - y(i \times \Delta t)]^2}{N - n}(1) \quad (1)$$

$$MSD(\tau) = a + 4D\tau \quad (2)$$

N is the number of data points in a trajectory, $\Delta t$ is the time interval of each frame, $x$ and $y$ are the coordinates of a particle, $a$ is the offset constant which incorporates the effects of localization error and finite camera exposure, and $D$ is the diffusion coefficient. The mean square displacement (MSD) was calculated for the time interval $\tau = n\Delta t$ for the entire duration of each trajectory. The first eight points of the MSD were averaged over all trajectories and plotted against time.

The diffusion coefficient, $D$, ($\mu m^2$/second) was calculated for each trajectory, from linear fits of the first four points of the MSD versus time function using equation. The diffusion coefficient (D) distribution was sorted into two populations, immobile and mobile. The immobile population of molecules explore an area inferior to that defined by the spatial resolution within one frame. The $D_{threshold}$ = 0.0316 $\mu m^2$/s was calculated as previously described.[100] The immobile population was composed of molecules with a D value lower than 0.0316 $\mu m^2$/s, while the mobile population was composed of molecules with D values above 0.0316 $\mu m^2$/s.

The Robust regression and Outlier (ROUT) outlier test on Graph Pad Prism was used to identify and remove outliers. Relative frequency distribution graphs and average MSD curves were obtained using Graph Prism (version 6.0).

### Single-Molecule Localization Microscopy and Cluster Analysis

EndoA$^{::mEos3.1}$ expressing larvae were dissected in either HL3 with Nefiracetam and NAS with or without 1 mM $CaCl_2$ and then fixed with 4 % para-formaldehyde. Single-molecule localization was carried out on an ELYRA PS.1 microscope (Zeiss). Each dataset was

Please cite this article in press as: Bademosi et al., EndophilinA-dependent coupling between activity-induced calcium influx and synaptic autophagy is disrupted by a Parkinson-risk mutation, Neuron (2023), https://doi.org/10.1016/j.neuron.2023.02.001



acquired at a rate of 20 Hz for a duration of 20,000 frames by which point the mEOS3.1-tagged molecule were fully photoconverted. Coordinates of individual localizations were retrieved from each time-lapse video using Zen software (Zeiss). The datasets were corrected for *x,y* drift using Zen's automated fiducial markers and affline transform algorithms. Localizations that appeared within 1 frame and 1 pixel of each other were consolidated to account for individual fluorophore blinking. Density-based spatial clustering of applications with noise (DBSCAN) analyses, a spatial clustering algorithm based on density, was used to quantify the clustering of proteins.[101] DBSCAN identifies clusters in large datasets of localization coordinates by a continuous and propagative method that links components of a common cluster based on two parameters, r, and $\varepsilon$. Were r is the search radius and $\varepsilon$ is the minimum number of neighbouring localizations within the search radius. Localizations outside the search radius and neighbouring points were classified as noise. The DBSCAN was implemented in Python.

### Transmission Electron Microscopy (TEM)

Third instar larvae were dissected in cold HL3 and processed for transmission electron microscopy as previously described.[102] Briefly, larval fillets were fixed in fresh 4 % para-formaldehyde (Electron Microscopy Sciences) and 1 % glutaraldehyde (Sigma) in 1 mM $MgCl_2$ (Sigma) and 0.1 M Na-cacodylate (Sigma) buffer, pH 7.2, overnight at 4°C. Samples were washed with 0.1 M Na-cacodylate, pH 7.4 and osmicated with 2 % osmium ($OsO_4$/Na-Cacodylate buffer). Next, tissue was stained with 2 % uranyl acetate (Electron Microscopy Sciences) for 1.5 h and embedded in Agar 100 resin (Agar Scientific). Horizontal ultrathin sections (70 nm) were collected. Synaptic boutons were examined and imaged using a JEM-1400 transmission electron microscope (Jeol) at 80 keV.

### Correlative Light Electron Microscopy (CLEM)

Correlative light and electron microscopy (CLEM) was performed as previously described[15]. Third instar larvae were dissected in cold HL3 and fixed for 2 h at 4°C (0.5 % glutaraldehyde, 2 % para-formaldehyde in 0.1 M PBS, pH 7.4). After washing in 0.1 M PBS, samples were stained with DAPI (Sigma). Pre-fixed larval fillets were then branded using a Zeiss LSM 780 equipped with a Mai Tai HP DeepSee laser (Spectra-Physics) at 880 nm with 40 % maximal power output. Z-stacks of the ROI where acquired before and after branding with a 25X water immersion lens (NA 0.8). Samples were then post-fixed (4 % para-formaldehyde, 2.5 % glutaraldehyde in 0.1 M phosphate buffer) overnight at 4°C. The lavae were washed with 0,1 M PBS and afterwards with ddH2O. During the rest of the preparation the larvae were washed after every step with ddH2O until the dehydration steps. Branded larvae were then osmicated for 1 h (1 % $OsO_4$ and 1.5 % potassium ferrocyanide). Then, the larvae were incubated in a 0.2 % tannic acid for 30 min followed by a second osmication step (1 % $OsO_4$ for 30 min) and subsequently put for 20 min in 1 % thiocarbohydrazide. The larvae were osmicated for a third time (1 % $OsO_4$ for 30 min) and incubated overnight in 0.5 % uranyl acetate. Samples were then stained with lead aspartate (Walton's lead aspartate: 20 mM lead nitrate in 30 mM sodium aspartate, pH 5.5) for 30 min at 60°C. After a final washing step the larvae were dehydrated with solutions of increasing ethanol concentration (30 %, 50 %, 70 %, 90 % and twice with 100 %) followed by two 10 min incubation steps with propylene oxide (PO). Larval fillets were then infiltrated with resin agar 100 (Laborimpex), flat embedded in resin agar 100 and placed at 60°C for 48 h.

For 3D-SEM, the flat resin-embedded larval fillets were cropped into 1 $mm^2$ pieces with region of interest in the middle and mounted on an aluminium specimen pin (Gatan) using conductive epoxy (Circuit Works). For approaching the region of interest, aluminium pins were places in a Zeiss Sigma VP SEM equipped with Gatan 3View technology. Once the first branding marks were reached and muscle morphology was recognized by correlating with the light microscopy data,70 nm sections were cut on an ultramicrotome (EM UC7, Leica) and collected on slot grids (Van Loenen Instruments). The sections were imaged using a JEM-1400 transmission electron microscope (Jeol) at 80 kV. Branding marks around the NMJ and DAPI signal were used to correlate the confocal images with the TEM micrographs of the NMJ boutons. Overlay images were generated using ImageJ and Gimp.

### FM 1-43

The labeling and quantification of FM1-43 intensities was performed as previously described.[103] Third instar larvae were dissected in fresh $Ca^{2+}$ free HL3, nerves were cut and larvae subsequently incubated for 1 min in HL3 with 4 $\mu$M FM 1-43 (Invitrogen), 1.5 mM $CaCl_2$ and 90 mM KCl. Multiple steps of washing with HL3 before imaging removed the non-internalized dye. Images of FM 1-43 were captured with an upright widefield microscope (Nikon Eclipse FN1), fitted with 60X (NA 1.0) water dipping lens and stored using NIS elements. Mean boutonic intensities were determined, after background substraction, using ImageJ.

### Electrophysiology

Current clamp experiments to record EJPs were performed as previously described.[97,104] Third instar larvae were dissected in $Ca^{2+}$ free HL3 which was subsequently replaced with HL3 with 2 mM $CaCl_2$ and nerves were cut below the ventral nerve cord. Motor nerves from muscle 6-7, segment A2 or A3 were stimulated at 10 Hz for 400s at least 50 % above the threshold, using a suction electrode. EJP sets were omitted when the recording did not hold its basal membrane potential throughout the 400 s stimulation paradigm. Signals were amplified using the Axoclamp900A amplifier (Molecular Devices), filtered using a 1 kHz Bessel filter and digitized at 10 kHz using a Digidata 1440A (Molecular Devices). Data storage, processing and analysis was done using Clampfit 10.7 (Molecular Devices). EJP amplitudes were quantified for each of the stimuli over the 400 s stimulation duration. The EJP amplitudes were then binned per 300 stimuli with the exception of the first 150 stimuli. The consecutive EJP amplitudes for each binned data point were normalized to the first binned data point of the first 150 stimuli.

Please cite this article in press as: Bademosi et al., EndophilinA-dependent coupling between activity-induced calcium influx and synaptic autophagy is disrupted by a Parkinson-risk mutation, Neuron (2023), https://doi.org/10.1016/j.neuron.2023.02.001



CellPress
OPEN ACCESS

### Western blot

Flies collected separately from three independent crosses were decapitated and heads homogenized with a motorized pestle in lysis buffer (25 mM HEPES, 100 mM NaCl, 1 mM $CaCl_2$, 1 % Triton, 1X Complete Protease Inhibitor (Sigma)). After incubation on ice for 30 min, samples were spun down at 10000 g for 10 min and supernatant collected and quantified by Bradford assay (BioRad) in a GloMax Multi Detection Plate Reader (Promega). After boiling in 1X Laemmli buffer with 8 % 2-mercapto-ethanol (Sigma), samples were ran on a NuPage 4-12 % Bis-Tris gel (Thermo Fisher Scientific) and transferred on a nitrocellulose membrane (BioRad) subsequently blocked with 10 % BSA in TBS. Primary antibodies were incubated overnight at 4°C in antibody solution (5 % BSA in 0.05 % TBS-T). Fluorescent secondary antibodies were incubated for 1 h at room temperature in antibody solution. After detection with an iBright imaging system (Thermo Fisher Scientific), fluorescent bands were quantified in ImageJ. EndoA fluorescence was normalized to GAPDH fluorescence.

Terminally differentiated dopaminergic neurons were detached with Accutase (Merck) and lysed with 1% Triton X-100 in PBS for 30 min at 4°C. Protein quantification and western blot was carried out the same way as for Drosophila proteins.

The following antibodies were used: guinea pig anti-EndoA (GP69) [1:5000[38]], rabbit anti-GAPDH [1:2000 (Abcam)], mouse anti-ENDOA1 [1:500 (Santa Cruz)], mouse anti-Dynamin [1:1000 (BD Biosciences)], mouse anti-Dynamin [1:250 (Santa Cruz)], rabbit anti-GST [1:2000 (Life Technologies)], anti-β actin [1:500 (Abcam)], anti-SH3GL2 [1:500 (GeneTex)]. Alexa Fluor-488/Alexa Fluor-647 conjugated secondary antibodies [1:1000 (Invitrogen)].

### RNA extraction, retrotranscription and quantitative real time PCR (qRT-PCR)

RNA was extracted from three biological replicates per genotype using the Maxwell® RSC microRNA tissue kit (Promega) according to manufacturer's instructions. 1μg of RNA was retrotranscribed for each sample (mock samples were included in the retrotranscription). First, the RNA was incubated with OligoDT at 65°C for 5 min. After adding the reaction mix (RT buffer, $MgCl_2$, DTT, RNase out, dNTP's and SuperScript III reverse transcriptase (Thermo Fisher)) samples were incubated 50 min at 50°C and then 5 min at 85°C. Samples were chilled on ice and RNaseH was added prior to a final incubated at 37°C for 20 min.

Primers for *Drosophila ENDOA* (PP20645) were retrieved from the FlyPrimerBank.[105] Primers for human *SH3GL2* were selected from.[106] Before use, the efficiency of the primer sets was tested by running a qRT-PCR with Light Cycler 480 SYBR Green (Roche) on a serial dilution of the cDNAs. ΔCt were calculated based on Ct values of the synaptic proteins Syt1.

### Recombinant protein production and purification

GST-tagged recombinant proteins were produced in competent BL21(DE3) *E.coli* by induction with 1 mM IPTG (Thermo Fisher Scientific) at 37°C for 4 h followed by additional overnight incubation at 25°C. Bacteria were collected by centrifugation at 8000 g, resuspended in lysis buffer (4 mM DTT, 1 mM EDTA, 1X Protease Inhibitor EDTA-free in 1X PBS. pH 6.5-8) and lysed using a high-pressure homogenizer operating at a pressure between 15000-20000 bar (Emulsiflex C5, Avestin). Homogenized samples were incubated with 1X DNaseI and spun down at 25000 g for 40 min at 4°C.

Purification was performed using affininty chromatography by loading the supernatant on two 5 ml GSTrap HP column (GE Healthcare) mounted in series and operated at 5 ml/min with an ÄKTA Pure 25 system (GE Healthcare). After binding, the column was washed with 10 column volumes of PBS followed by 5 column volumes of PreScission buffer (20 mM Tris, 100 mM NaCl, 1 mM EDTA, 1 mM DTT, pH 8). Cleavage of the GST tag was perfomed on column at room temperature for 4 h with 500 U of PreScission Protease (GE Healthcare) diluted in PreScission buffer. Cleaved protein was collected in PBS by peak fractionation, while the remaining uncleaved protein was eluted with 5 column volumes of 100 % elution buffer (20 mM Tris, 10 mM Gluthatione reduced, pH 8).

Input material and collected fractions were analyzed by SDS-PAGE on NuPage 4-12 % Bis-Tris gel (Thermo Fisher Scientific) and stained with Coomassie.

EndoA protein concentrations were estimated by absorbance using the calculated molar extinction coefficient of 17670 $M^{-1}cm^{-1}$ for the *Drosophila* proteins, and 17545 $M^{-1}cm^{-1}$ for the human proteins.

### Biophysical/structural characterization of recombinant proteins

Prior to biophysical/structural characterization experiments, purified proteins were subjected to gel filtration to isolate the peak corresponding to dimeric EndoA. A Superdex 200 increase 30/100 column (GE Healthcare) was operated at a flow rate of 0.5 ml/min and buffered with 20 mM MOPS, 150 mM NaCl pH 7. The elution volume of the dimer peak was previously determined by Size exclusion chromatography-Multi angle light scattering (SEC-MALS).

Thermal stability was determined through thermal denaturation (from 20°C to 95°C at an increment rate of 0.3°C/min) monitored by fluorescent emission intensity upon excitation at 266 nm. Measurements were obtained in an Uncle instrument (Unchained Labs). $EndoA^{WT}$ was concentrated to ~3 mg/ml (Amicon Ultra centrifugal filters) and filtered through a 0.22 μm filter (Millex). Thermal stability was tested in the presence of 1 mM EDTA or 1 mM $CaCl_2$. Measurements were done in triplicate and average thermograms were displayed by plotting the barycentric mean (BCM) and Static light scattering (SLS) at 266 nm.

Fourier Transform InfraRed (FTIR) spectroscopy was performed on an Invenio spectrometer (Bruker) equipped with a BioATR-II measuring cell (Bruker). Proteins were concentrated to ~2 mg/ml and filtered through a 0.22 μm filter (Millex). Recordings were

Please cite this article in press as: Bademosi et al., EndophilinA-dependent coupling between activity-induced calcium influx and synaptic autophagy is disrupted by a Parkinson-risk mutation, Neuron (2023), https://doi.org/10.1016/j.neuron.2023.02.001



performed at 25°C. The temperature was controlled by a thermostatic water bath. Spectra were acquired with a resolution of 4 $cm^{-1}$ and with a total of 120 scans per spectra averaged to improve the signal-to-noise ratio.

Dynamic light scattering (DLS) measurements were performed in a DynaPro DLS plate reader (Wyatt). Proteins were concentrated to ~2 mg/ml, filtered through a 0.22 μm filter (Millex) and loaded on a low binding 394-well black plate with transparent bottom (Costar). The autocorrelation of scattered light intensity was averaged over 5 recordings to obtain single data points. Wyatt Dynamics software (v7) was used to calculate the hydrodynamic radius.

For Small angle X-ray Scattering (SAXS) purified *Drosophila* EndoA and human ENDOA1 proteins were run though a Superdex200 10/300 increase chromatographgy column (GE Healthcare) to isolate the peak corresponding to the dimeric protein. The column was buffered in 20 mM MOPS, 150 mM NaCl, 1 mM DTT, pH 7 or 20 mM MOPS, 150 mM NaCl, 1 mM DTT, 1 mM $CaCl_2$, pH 7. Dimeric proteins were concentrated with an Amicon Ultra centrifugal filter to a concentration of at least 6 mg/ml. Concentrations were determined by absorbance. SAXS data were collected according to Table S1. The sample of *Drosophila* $EndoA^{D265A}$ mutant was measured at the BM29 beamline of the ESRF synchrotron (Grenoble, France),[107] while all other samples were measured at the SWING beamline of the SOLEIL synchrotron (Paris, France).[108] Measurements were performed using the HPLC-SEC setup available at the beamlines by injecting 30-50 μl of 6-11 mg/ml of protein onto an Advanced BioSEC 300Å 2.7/300 column. The column was pre-equilibrated with a buffer containing 20 mM MOPS (pH 7), 150 mM NaCl, 1 mM DTT, 5 % glycerol and either no calcium or 1 mM $CaCl_2$. The flow rate was set at 0.3 ml/min for the measurement performed at the BM29 beamline and at 0.35 ml/min for the ones measured at the SWING beamline. The radial averaging was performed using BsxCuBE[107] for the data collected at the ESRF synchrotron and using FOXTROT[109] for those collected at the SOLEIL synchrotron. Buffer subtractions were performed using CHROMIXS[110] and the averaged data, corresponding to the peak of interest, were further processed using the ATSAS software package.[111] The molecular weight estimations were taken from the Bayesian assessment method,[112] while the Kratky plots were generated using the ATSAS program PRIMUS[113]).

### Amide hydrogen/deuterium exchange mass spectrometry (HDX-MS)

Local HDX-MS conditions and analysis routines have been described in detail in.[114,115] Specific conditions used in this study are detailed below.

#### *Sample preparation*

Purified EndophilinA and derivatives (~150 μM) were dialyzed in 25 mM Tris (pH 8), 25 mM KCl.

#### *D-exchange reaction*

Lyophilized buffer (25 mM Tris-HCl pH 8.0, 25 mM KCl), reconstituted in 99.9% $D_2O$ (Euriso-top) and 2mM fresh TCEP [tris(2-carboxyethyl)phosphine], was adjusted to $pH_{read}$=8.0 and pre-incubated on ice. The exchange reaction initiated by diluting the protein into $D_2O$ buffer (final concentration: 90% $D_2O$; 10 μM protein). Labelling for various time points (5 s, 10 s, 30 s, 1 min, 5 min, 15 min, 30 min and 60 min) occurred on ice.

#### *Quenching*

Pre-chilled quench buffer (1.3 % formic acid, 4 mM TCEP, 0.1 % DDM, 4 M Urea) was added at 1:1 ratio (final pH=2.4), and incubated (4°C; 2 min). During this incubation the reaction was centrifuged (20000 x g; 90 s; 4°C; Eppendorf) to remove aggregated material.

#### *Full deuteration controls*

Under the same D-exchange/quench conditions, a protein sample that has been dialyzed (o/n, RT), in 8 M Urea, 25 mM Tris-HCl (pH 8), 25 mM KCl buffer, was labelled for 10 s, on ice.

#### *LC-MS conditions*

450 pmol protein were injected into a nanoACQUITY UPLC with HDX technology (Waters, UK) coupled to a SYNAPT G2 ESI-Q-TOF MS system and digested online using a nepenthesin-2 cartridge (2 mm x 2 cm, Affipro), at 16°C. Peptides were first trapped onto a VanGuard C18 Pre-column, (130 Å, 1.7 mm, 2.1 x 5 mm, Waters) at 100 mL/min for 3 min using 0.23% (v/v) formic acid and then separated on a C18 analytical column (130 A°, 1.7 mm, 1 x 100 mm, Waters) at 40 mL/min, at 2°C. For UPLC separation (solvent A: 0.23 % v/v formic acid, solvent B: 0.23 % v/v formic acid in acetonitrile) a 12 min linear gradient was used (5-50 % solvent B). Then, solvent B was raised to 90 % (1 min) for column cleaning. MS parameters: capillary voltage 3.0 kV, sampling cone voltage 20 V, extraction cone voltage 3.6 V, source temperature 80°C, desolvation gas flow 500 L/h at 150°C. The % of D-uptake was calculated using the full deuteration control values. Deuterium/Protium back exchange values for our instrumental set up have been previously calculated.[114]

#### *Peptide identification*

200 pmol of protein in 25 mM Tris-HCl (pH 8), 25 mM KCl buffer, quenched as described above, were analyzed in the $MS^E$ acquisition mode of the previously described LC-MS system, over the 100–2,000 Da m/z range. Collision energy ramped from 15 to 35 V; other instrument parameters as described above. We used the primary sequence of EndophilinA or derivatives as search template and the ProteinLynx Global Server (PLGS v3.0.1, Waters, UK). Only peptides that had a signal to noise ratio >10, PLGS score >7 and appeared in 3 out of 6 replicate runs for each derivative were considered. These peptides were individually assessed for accurate identification.

#### *Replicates*

Data were obtained from minimum 2 separate protein purifications (biological repeats), in technical triplicates and over multiple days to control for instrument variation. Biological and technical repeats were all combined showing repeatability (average std deviation) in the 0.054–0.075 range. All spectra were individually inspected and manually curated to ensure accurate centroid calculations.

Please cite this article in press as: Bademosi et al., EndophilinA-dependent coupling between activity-induced calcium influx and synaptic autophagy is disrupted by a Parkinson-risk mutation, Neuron (2023), https://doi.org/10.1016/j.neuron.2023.02.001



CellPress
OPEN ACCESS

### Data analysis

The DynamX 3.0 (Waters, Milford MA) software was used. Peptides with average D-uptake and standard deviations, are presented in Table S2 (as suggested in[46]). HDX data were further analyzed using PyHDX (v0.4.1(68624c40)[47] to derive ΔGs. Output ΔGs values/residue are presented in Table S3. PyHDX was also used to determine the relative fractional uptake (RFU values)/residue, relative to a fully deuterated control sample (as described in [116]). Output values are presented in Table S4.

### SH-SY5Y cell maintenance and lysis

Human SH-SY5Y neuroblastoma cells were cultured in DMEM/F-12 (Gibco) supplemented with 10% (v/v) fetal bovine serum (Gibco), 100 units/mL of penicillin, and 100 μg/mL of streptomycin. Cells maintained under standard conditions (37°C, 5% CO2) and split every 4–5 days. For the lysis, cells were pelleted and incubated with 1% Triton X-100 in PBS for 30 min at 4°C. After a centrifugation step (5 min at 13000 g), protein concentration on the supernatant was quantified by Bradford assay (BioRad) in a GloMax Multi Detection Plate Reader (Promega).

### Co-immunoprecipitation

50 μl of slurry Dynabeads Protein G (Thermo Fisher) were coupled with 5 μg of mouse monoclonal anti-Dynamin antibody (BD Biosciences or Invitrogen for the pull down of fly and human Dynamin respectively) rotating for 1 h at room temperature. Beads were washed twice with wash buffer (50 mM Tris, 150 mM NaCl, pH 7.5) and incubated overnight at 4°C with 1 mg of total *Drosophila* ($w^{1118}$) head lysate or 1 mg of SH-SY5Y cells lysate diluted in wash buffer to a final volume of 400 μl. After washing the beads twice with wash buffer, they were incubated for 4 h at room temperature with 30 μg of purified GST-EndoA$^{WT}$, GST-EndoA$^{D265A}$, GST-EndoA$^{D265R}$, GST-SH3GL3$^{WT}$ or GST-SH3GL2$^{G276V}$. Following washes, the beads were resuspended in wash buffer and loading dye (4X Laemlli buffer (Bio-Rad) + 2-mercapto ethanol (Sigma)), boiled for 10 min at 95°C and loaded on NuPage 4-12 % Bis-Tris gel (Thermo Fisher Scientific). After transferring the proteins on a nitrocellulose membrane (BioRad), the membrane was processed for Western blotting as described in the 'Western blot' section.

Control Co-IP were performed by incubating 50 μl of slurry Dynabeads Protein G, not coupled with anti-Dynamin antibody, with 1 mg of total head lysate followed by incubation with 30 μg of purified GST-EndoA$^{WT}$ or GST-SH3GL2$^{WT}$. Incubation times were the same as for the other conditions.

GST-EndoA proteins used for this assay were purified as described in the 'recombinant proteins production and purification' paragraph, with the exception that the GST tag was not cleaved. Proteins were eluted from the 5 ml GSTrap HP column with elution buffer (20 mM Tris, 10 mM Gluthatione reduced, pH 8) and dialyzed overnight at 4°C in 50 mM Tris, 150 mM NaCl, pH 7.5. GST-EndoA proteins concentrations were estimated by absorbance using the calculated molar extinction coefficient of 60780 $M^{-1}cm^{-1}$ and GST-SH3GL2 proteins with molar excitation coefficient of 60655 $M^{-1}cm^{-1}$. Protein concentration was measured prior to each experiment.

### Electroretinograms (ERGs)

ERGs were recorded from 1 to 3-day-old flies as previously described.[15] Flies were immobilized on glass microscope slides, by use of double-sided tape. For recordings, glass electrodes (borosilicate, 1.5 mm outer diameter) filled with 3 M NaCl were placed in the thorax as a reference and on the fly eye for recordings. Responses to repetitive light stimuli were recorded using Axosope 10.7 and analyzed using Clampfit 10.7 software (Molecular Devices) and Igor Pro 6.37.

### Light induced neurodegeneration and histology

Light induced retinal degeneration induced by placing 1 to 3-day-old flies under continuous illumination (1300 lux).[117] Batches of flies were also kept in darkness for 7 days at 25°C. Flies were used for ERG data acquisition, or processed for histological staining of the retina.

Histological sections of the retina were prepared by decapitating heads and fixing them in 4 % para-formaldehyde and 2.5 % glutaraldehyde in 0.1 M PBS overnight at 4°C or until further processing. Heads were then osmicated in 2 % $OsO_4$ for 2 h and subsequently incubated in 4 % uranyl acetate for 1 h. After dehydration using an ethanol series, heads were embedded in hard resin (Agar 100, Laborimpex) and semi-thin (1.5 μm) sections were cut on a microtome (EM UC7, Leica) and stained on a heating block with a 1 % toluidine blue (Merck) solution including 2 % Borax for 90 s at 60°C. The stained sections were mounted with Eukit Quick-hardening mounting medium (Sigma). Histological sections were imaged using the Leica DM2500 M microscope equipped with a 40X lens and the LAS v4.0 software.

### Gene editing of iPSC

*SH3GL2* p.G276V was engineered in the "Ctrl65" iPSC line (SFC065, [66]), by means of CRISPR/Cas9 gene editing using a split puromycin recombination reporter.[94] One million cells were seeded per well of a 6-well plate in the presence of Rho kinase inhibitor the day before transfection (Miltenyi Biotech; 130-106-538). The next day, the cells were transfected using Lipofectamine Stem (Life Technologies; STEM00015) with a mix of 1 μg donor single stranded oligodeoxynucleotide, 0.5 μg pRR_SH3GL2(G276V) plasmid specific for the guide RNA (gRNA) spacer sequence and 1 μg pX_SH3GL2_G276V_gRNA1 encoding for a guide RNA targeting the mutation site. Two days post-transfection, cells were treated with 0.5 μg/ml puromycin for 48 h in the presence of Rho kinase inhibitor. Ten to fourteen days after transfection, resistant colonies were manually picked, expanded, and molecularly characterized

Please cite this article in press as: Bademosi et al., EndophilinA-dependent coupling between activity-induced calcium influx and synaptic autophagy is disrupted by a Parkinson-risk mutation, Neuron (2023), https://doi.org/10.1016/j.neuron.2023.02.001



by means of PCR, Sanger sequencing and digital droplet PCR to discard large deletions. Clones showing the desired genotype were karyotyped by means of comparative genomic hybridization (CGH) and stained for pluripotency markers.

### iPSC differentiation

On day -1, 300.000 hiPSC/cm$^2$ were seeded on Matrigel coated 6-well plate wells in mTeSR-Plus medium supplemented with 10 μM Rho kinase inhibitor (RI). On day 0, medium was switched to knockout serum replacement medium (KSR) containing DMEM/F-12, 15 % knockout serum replacement, GlutaMAX, Penstrep, non-essential amino acids and 10 μM β-mercaptoethanol (all from Life Technologies) supplemented with LDN193189 (500 nM, Sigma), SB431542 (10 μM, Tocris), SHH-C24II (100 ng/ml, Miltenyi Biotec), Purmorphamine (2 μM, Sigma). CHIR99021 was added to the medium from day 3 to day 13 (CHIR; 3 μM, Stemcell Technologies). From day 4, KSR was gradually shifted to Neurobasal/0.5X B27 supplement without vitamin A, 0.5X N2, GlutaMAX, Penstrep, non-essential amino acids at the rate of 1/3 every 2 days for 4 days, and to ¼ for 3 days. SB431542, SHH-C24II, and Purmorphamine were withdrawn from the medium at day 7. FGF8b (100 ng/mL, R&D) was added to the medium from day 9 until day 16. At day 18, cells were switched to terminal differentiation medium consisting of Neurobasal-A/1xB27 supplement without vitamin A, GlutaMAX, Penstrep containing BDNF (brain-derived neurotrophic factor, 10 ng/ml; R&D), ascorbic acid (0.2 mM, Sigma), GDNF (glial cell line-derived neurotrophic factor, 10 ng/ml; R&D), dibutyryl cAMP (0.2 mM; Sigma), SR11237 (100 nM, Tocris), and DAPT (10 μM; Tocris). On day 20, ventral midbrain neural progenitors were cryopreserved and quality controlled. Neural progenitor cells were terminally differentiated on coverslips previously coated with poly-D-lysine (50 μg/mL)/mouse laminin (1 μg/mL) in terminal differentiation medium for additional 35 days.

### Analysis of LC3B puncta in TH$^+$ neurites

Terminally differentiated vmDAn (55-60 days) were incubated for 15 min in physiological solution (20 mM HEPES pH 7.4, 140 mM NaCl, 4.7 mM KCl, 2.5 mM $CaCl_2$, 1.2 mM $MgSO_4$, 1.2 mM $KH_2PO_4$, 11 mM glucose) and subsequently fixed with 4 % para-formaldehyde, processed for immunostaining and imaged as described in the 'Immunohistochemistry and confocal imaging' paragraph.

Z-stack confocal images were analyzed with ImageJ in a semi-automated way. The 'Skeletonize' plugin was ran on the TH channel and the total length of TH$^+$ neurites was measured. The skeleton was converted to a mask within which LC3B puncta were counted using the 'Analyze particle' plugin. The number of LC3B puncta within the mask were normalized by the total length of TH$^+$ neurites and plotted as LC3B puncta/TH$^+$ unit length.

## QUANTIFICATION AND STATISTICAL ANALYSIS

GraphPad Prism 9.3 (San Diego, USA) was used to determine statistical significance. Datasets were tested for normal distribution using the D'Agostino-Person Omnibus and Shapiro-Wilk normality tests. Normally distributed data were tested with parametric tests: when two datasets were compared, the Student's *t*-test was used, and when more than two datasets were compared, a one-way analysis of variance test (ANOVA) followed by a *post hoc* Tukey test was used. For non-normally distributed datasets, Mann-Whitney test was used when comparing two datasets, and an ANOVA Kruskal-Wallis test followed by a Dunn's *post hoc* test was used for multiple datasets. When multiple parameters were compared (genotypes and treatments) a two-way ANOVA was used, followed by a *post hoc* Tukey test or Šidàk test for multiple comparison correction. Significance levels are defined as $^{***}P < 0.0001$, $^{**}P < 0.01$, $^{*}P < 0.05$ and ns, not significant. 'n' in the legends indicates the number of animals used and analyzed. For the biochemical experiments, 'n' indicates the number of times the experiment was performed. For the analysis of microscopy images of iPSC-derived neurons, 'n' indicates the number of images analyzed, which were always acquired from three independent neuronal differentiations. For sptPALM images 2 separate NMJs were imaged per animal, while for the confocal imaging and single molecule localization studies, 4 different NMJs were imaged in each animal. Data are plotted as mean ± SEM and specifics on the statistical test used for analysis are reported in the figure legends.